Cave Front Tracking Experiment

by

Mark Green

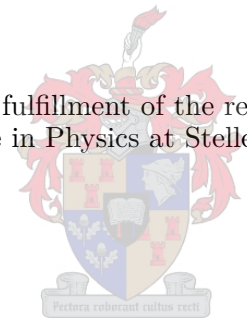

Thesis presented in partial fulfillment of the requirements for the degree of
Master of Science in Physics at Stellenbosch University

Supervisor: Prof. Kristian Muller-Nedebock

Co-supervisor: Dr. Richard Lynch & Dr. Leandro Boonzaaier

Department of Physics

December 2016

Declaration

By submitting this thesis electronically, I declare that the entirety of the work contained therein is my own, original work, that I am the sole author thereof (save to the extent explicitly otherwise stated), that reproduction and publication thereof by Stellenbosch University will not infringe any third party rights and that I have not previously in its entirety or in part submitted it for obtaining any qualification.

December 2016

Acknowledgments

I would like to offer special thanks to Dr. Geoff Capes for initiating the Cave Front Monitoring Project and the Geo-technical team of Ridgeway mine who helped with the setup and maintenance of the experiment over its two year operation. Thanks go out to the IMS research patrons, in particular Newcrest Mining Limited who sponsored the project between the years 2012 and 2014.

I would like to offer my thanks the following individuals who played a part in the experiment and bringing this thesis to its final completion:

Richard Lynch for organizing and coordinating the research project and laying the foundation for the thesis.

Rod Green for the support and advice on experimental procedure and thesis writing.

Gerrit Oilvier for advice and encouragement and drawing my attention to similar work in the field.

Leandro Boonzaaier for supervising the administration of the thesis over its extended writing period.

Abstract

Seismic tomography, a procedure to trace seismic wave velocity variation, has been used for more than 100 years to "see through rock". Initially the recording of seismic waves from natural sources (earthquakes) using seismographs, provided the first evidence of the crust - mantle boundary. Further development of recording techniques and use of explosive seismic sources were employed for the delineation of the geological structures of mineral deposits (primarily oil and gas) as well as detailing the earth - mantle location and geometry. Ultra sonic techniques have been applied in the laboratory experiments to characterise rock sample velocities and its relationship to changes in temperature and stress. Active seismic tomography for hydrocarbon resources determination as well as for the earth structure utilized both reflection and refraction techniques. During the early 60's seismic techniques were employed in active mines to investigate rock properties for geotechnical purposes.

The objective of the Cave Front Tracking Experiment was to investigate whether active seismic tomography could potentially be used to track the cave back progression of a block cave mine. A small scale experiment was conducted to study the variations in seismic travel times associated with ray path refraction caused by stress changes and changes in the rock fabric induced by sub-level mining. A piezoelectric transducer was employed as an active seismic source and a seismic recording system was installed to monitor a volume of rock through which sub-level mining was propergated. Implementation involved the deployment of 11 seismic detectors and the recording of pre-stacked data. The experimental details and hardware characteristics are discussed, which includes technical problems encountered, the process and techniques of significant data stacking in order to recover weak signals generated by a piezoelectric seismic source and travel time variation calculation using signal cross-correlation. Signal travel time variation measurements were made over the course of a year and a half (2013-14), however only five months are investigated in detail and related to mining activities.

Finite difference numerical modelling was also employed in order to create a better understanding of the sub-level mining process and its effect on seismic signal delay change. Technical problems associated with the signal processing and signal behavior interacting with an advancing mining front were identified and a number of techniques were employed to overcome problems faced by routine cave front estimation in a working mine environment.

The field testing of a prototype impact source that is pneumatically driven and an eccentric rotating mass device is discussed.

Opsomming

Seismiese tomografie, 'n prosedure om die variasies in seismiese golfsnelhede na te spoor, word reeds meer as 100 jaar gebruik om "deur rots te sien". Deur die meting van seismiese golwe van aardbewings het die eerste seismograwe inligting verskaf oor die bestaan – en posisie van die kors-mantel oorgang. Wanneer golwe van natuurlike seismiese bronne ge-analiseer word verwys ons na 'passiewe' tomografie terwyl 'aktiewe' tomografie verways na die gebruik van kunsmatige seismiese bronne, soos ontploffings of vibreerders. Verbeterde opnametegnieke en die gebruik van ontploffings as seismiese bronne het gehelp om aardstruktuur en ook die strukturele aard van ertsafsettings en die van olie en gasvelde te detaileer. Ultrasoniese tegnieke word in laboratoriumeksperimente aangewend om die seismiese golfsnelhede van rotsmonsters te karakteriseer, asook om die verband tussen die veranderinge in golfsnelhede en veranderinge in temperatuur en ook veranderinge in spanning te bepaal. Beide reflektiewe en refraktiewe tegnieke word gebruik in aktiewe seismiese tomografie vir die studie van koolwaterstof-bronne en die aardstruktuur. Gedurende die vroeë 60's is seismiese tegnieke in myne gebruik om die geotegniese aard van die rots te bestudeer vir 'n beter begrip van die onstaan van rotsbarste en die algemene meganiese gedrag van rots.

Die doel van die mynboufront-volgingseksperiment is om aktiewe seismiese tomografie te gebruik om variasies in seismiese reistye (Engels: travel times) te bestudeer. Hierdie variasies hou verband met golfroete-refraksie wat veroorsaak word deur verandering in spanning en in die geotegniese aard van die rotsmedium onder die invloed van mynbou. 'n Piësoëlektriese transduktor is as aktiewe seismiese bron gebruik en 'n seismiese waarnemingstelsel is geïnstalleer om die rotsvolume te moniteer waardeur 'n groot myn-opening sou vorder. In hierdie verhandeling word verslag gegee oor die tegniese probleme en die vordering van die projek. Die projek behels die ontplooiing van 11 seismiese sensors en die opname van vooraf-gestapelde data – deur groot hoeveelhede digitale seismogramme van dieselfde bron op mekaar te stapel kan klein veranderinge in golfsnelhede bespeur word. Die eksperimentele detail en eienskappe van die hardeware word bespreek, wat die proses en tegnieke van beduidende data-stapeling vir die uitsifting van swak seine vanaf 'n piësoëlektriese seismiese bron insluit. Metings van die variasies in sein-reistyd wat met mynbouaktiwiteite verband hou, is oor die verloop van 'n jaar (2013-14) gedoen.

Die numeriese modeleringstegniek van eindige verskille is gebruik om 'n beter begrip te kry van die migreerende mynboufront en die effek daarvan op seismiese seine se fasevertraging. Die probleme wat geassosieer word met die ondersoek van die seismiese data van 'n migreerende mynboufront is geïdentifiseer en 'n aantal tegnieke is aangewend om probleme te oorkom wat verband hou met roetine skatting van die posisie and mynboufront'n myn.

Die veldtoetsing van 'n prototipe impakbron wat deur lugdruk aangedryf word, en 'n bron gebaseer op 'n eksentries-roterende massa, word beskryf.

Contents

List of Figures

List of Tables

Nomenclature

Roman Symbols

A	Amplitude of a waveform.
C	The normalised cross-correlation function.
f	Frequency.
H	Front estimation cost function.
K	The current modelled mining step.
m	Numer of samples in a waveform.
n	Number of seismograms used in a stack.
Q	Rock quality factor which plays a role in signal frequency attenuation.
S	The total number of sensors used in the array.
T	Travel time soluation calculated using the Fast Marching Method.
t	Time sequence of the reference waveform.
V_p	P-wave velocity.
V_s	S-wave velocity.
x, y, z	Spatial position along Cartesian co-ordinates.

Abbreviations

ATU	Analogue Time Update, a specific signal used to maintain time synchronization.
CFL	Courant-Friedrich-Lewy condition.
E3D	Dynamic seismic wave modelling program.
EMI	Electromagnetic Interference, originating from high voltage driving signals.
ERM	Eccentric Rotating Mass.
FMM	Fast Marching Method.
GPS	Global Positioning System, used to acquire accurate absolute time.

GS	Geotechnical Seismometer
PPS	Pulse-Per-Second, a specific signal, generated every second, to maintain time synchronization.
RMS	Root mean squared.
WGN	White Gaussian Noise, a sequence of random uncorrelated values with a constant power spectral density.

Greek Symbols

Δ	Parameter change.
λ	Signal wavelength.
ϕ	Signal phase-lag.
Φ^{E3D}	Signal delay calculated using phase-delays measured from E3D synthetic seismograms.
Φ^{FMM}	Signal delay calculated using FMM travel times solutions.
ρ	Rock density.
σ	Spatial position along Cartesian co-ordinates.
τ	Time sequence of the comparator waveform.

Seismic Terminology

Accelerometer	A type of acceleration transducer, used to measure ground motion.
Access drive	An underground tunnel linking levels or cross-cuts together.
Blast	The detonation of conventional explosives in one or more boreholes, to break up rock for extraction.
Body Wave	The seismic wave that travels through the interior of a seismic medium.
Bulk medium	The intact host rock which has not been altered by mining activities.
Caving	A mining method that exploits gravity to break up an ore body.
Crosscut	A horizontal tunnel extention created to access an ore body/seem, typically perpendicular to an access drive.
Digitizer	An electronic device that converts an electrical analogue reading to a digital form.
Drawbell	A funnel shaped excavation of rock, used to feed ore from above to an extraction tunnel below.
Geophone	A type of velocity transducer, used to measure ground motion.
Grout	A type of concrete used to secure seismic devices within a borehole.

Level	A set of underground inter-linked horizontial tunnels.
Microfracture	Rock fractures that are several millimeters or less in length and are typically much smaller than seismic signal wavelength.
Noise	Portions of a seismogram originating from amibient activity that is not part of the desired signal.
Offset	The phase seperation between two correlated signals.
P-wave	Seismic pressure wave that oscillates in the longitudinal axis of the wave.
Piezoelectric	A type of material that undergoes a change in volume when exposed to an electric field.
Post-stack	A seismogram stack created using pre-stacks to improve signal-to-noise ratios.
Pre-stack	A seismogram stack created early in the recording process to reduce data storage requirements.
Ray-path	The path of shortest travel time taken by seismic signal traveling between source and sensor.
Reference	Signal data to which other recorded data is compared.
Ring	A set of boreholes drilled into a tunnel ceiling, forming a semi-circular shape, intended for blasting.
S-wave	Seismic shear wave that oscillates in the transverse axis of the wave.
Seismicity	Occurrence of seismic events associated with a seismogenic region.
Seismogram	An record of seismic vibrations measured by a seismic sensor.
Seismometer	An instrument that records seismic vibrations from a seismic sensor.
Shot	A signal seismic signal generated by an active source device.
Signal	The waveform that drives or is generated by the piezoelectric source.
Source	A physical process or device generating seismic vibrations.
Stack	A seismogram that results from stacking two or more seismograms.
Stacking	The process of stacking two or more seismograms.

Chapter 1

Introduction

Block Cave Mining

Block cave mining (colloquially referred to as caving) is a method of underground mining which exploits the effect of gravity to aid in the break up and extraction of underground mineral resources. This approach involves tunneling to a position beneath a massive steeply dipping ore body, creating a network of tunnels that make up an extraction level and then stimulating the break up of the ore body from this extraction level through various methods such as blasting and hydraulic fracturing (Figure 1.1). Removing material from beneath the ore body leaves the bottom of the rock mass unsupported, causing further fracturing and break up of the ore body from below due to stresses acting on the mass. This process results in the formation of a cave, with the extraction level at the bottom, a muck pile of broken up rock which makes up the floor of the cave and the heavily fractured ceiling or cave back which forms the bottom of the ore body (Figure 1.2). The cavity between the top of the muck pile and the ceiling of the cave is known as the air gap. A subsidence zone will typically form at the surface, directly above the caving zone. Extraction of the broken up ore in a controlled manner allows this caving process to be self-sustaining, making block caving an efficient means of mining once the caving process has started.

There are several downsides to this method of mining, namely the extensive capital outlay and mine development required to setup block cave mining and the low degree of control over the growth and progression of the cave (once it has started propagating). This inherent inability to readily track the progression of the cave is of particular interest.

Knowledge of both the extent of a cavity and its directions of progression is not only important for ensuring a steady flow of gravity fed ore but also of particular importance for mine safety. The full extent of the problems that can result from inaccurate cave state knowledge was highlighted by the North Parkes incident in New South Wales, Australia [2]. A hang up in the breakup of the North Parkes cave resulted insufficient broken material falling into the extraction level compared to the volume being extracted. This resulted in the airgap growing well beyond the established safe limits and was estimated to be 180 m high at the time incident.

This proved disastrous when the cave eventually breached a weaker supporting rock layer, resulting in a large portion of the remaining cave to gave way. The massive volume of rock falling into the over extended air gap volume acted as a piston by compressing the air which generated an extremely powerful air blast. This blow out severally damaged an exploration drive and the extraction level and resulted in the deaths of four mine personal. Had the extent full extent of the cave and its condition been known at the time, this tragedy could have been avoided.

The difficulty in tracking the shape and height of the cave arises from the lack of access

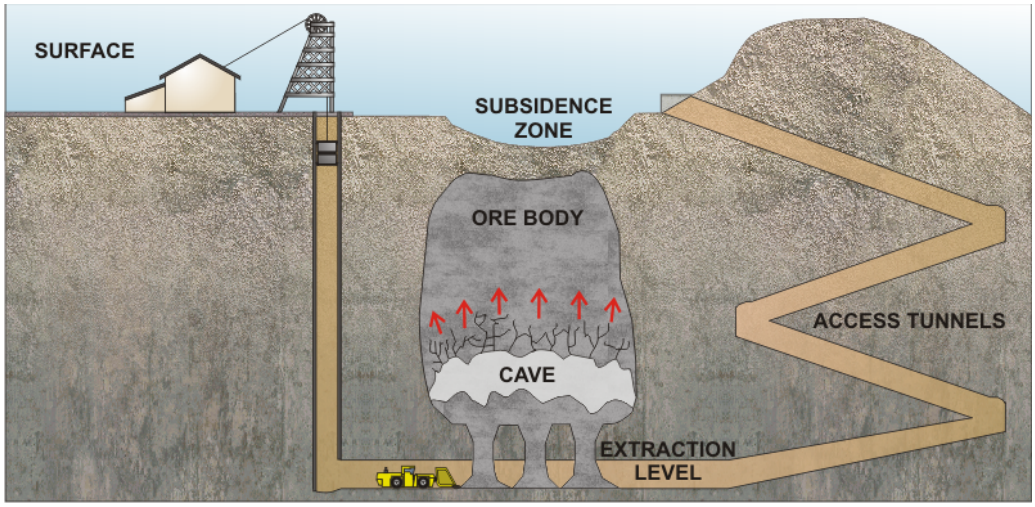

Figure 1.1: A cross-section illustration that depicts a typical block cave mine configuration. Access tunnels are created to a point beneath a steeply dipping ore body where the extraction level is then created. The ore body is broken up from below and ore falls to the extraction level where it is scooped up and transported to the surface for processing. Figure is not to scales.

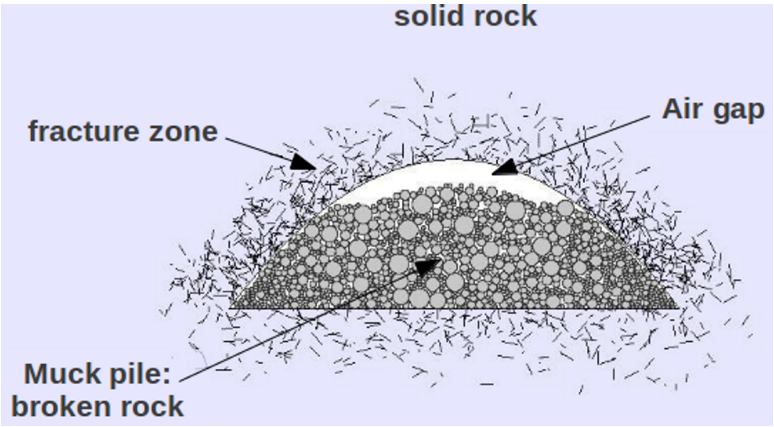

Figure 1.2: An cross-section illustration of a block-cave mine that details the different sections of the block cave. The ceiling of the cave or cave back is heavily fractured by gravity and heavy stresses acting from above. Broken rock falls to the floor forming a muck pile which feeds into shoots called draw bells. Image originally compiled by Dr. R. A. Lynch.

to the caving area with the result that the cave cannot be studied by direct physical means. There are a number of possible ways by which the cave back might be tracked, each with varying degrees of success. The use of borehole cameras is often limited by the difficulty of probing individual boreholes and the problems which arise from borehole closure over time.

Another passive method involves the use of progression makers which are interspersed throughout the ore body. Before the caving process is started, these serialized markers are inserted into the ore body using boreholes drilled at various heights and orientations (typically geological exploration boreholes). As the cave progresses upward, so the markers fall from the ceiling and are eventually extracted along with the rest of the broken rock. The markers are then recovered from the ore (using powerful electromagnetic separators) and by pinpointing their position of installation, the ceiling of the cave can be extrapolated. While this method provides a good picture about the shape of the cave, the time between when a marker is detached from the cave ceiling and to when it is identified can be several days if not weeks, which greatly delays the vital information it provides.

Passive seismic monitoring relies on the natural seismicity generated by the fracturing process of the cave back. The level of seismic activity that it generates is used as the the proxy for cave growth. However, an aseismic gap exists between the actual cave back and the location of the seismic activity which prevents the reliable estimation of the cave geometry [33].

While such methods do provide some information about the cave's progression upwards, the picture generated is not wholly accurate and does not provide information on a regular basis. This implies that a technique of scanning the shape of the cave both accurately and routinely would be advantageous.

Active seismic tomography techniques are routinely used by the oil and gas exploration industry to study and map voids and areas of seismic velocity contrast which could further have the potential to create accurate three dimensional scans of a block cave. Unfortunately the technology and methods employed are extremely costly, requiring extensive instrumentation operated by teams of trained professionals, which in most cases is not a practical solution in a mine scale operation. In order to develop a cost effective tool applicable to the mining, a different approach to the use of active seismic was taken which focused on studying the incremental changes on the medium caused by mining to build a picture of its state of excavation as opposed to the normal tomography approach which seeks to measure medium contrasts directly. The first IMS Cave Front Tracking Experiment was proposed in order to develop the methods and technology that could in turn be used to track cave back growth.

The aim of this project was to investigate whether a small scale active seismic monitoring array could be used towards the goal of routinely monitoring the progression of the cave back in a block cave mine. Two approaches were taken to achieve this. A numerical modelling investigation to gain an understanding of active seismic signal behavior when used to track an advancing mine front and a physical experiment that would monitor a controlled small scale mining operation in an underground mine. The chosen experiment site was a Halo sub-level caving region at Ridgeway Deeps Mine outside Orange, New South Wales, Australia.

The physical experiment made use of a piezoelectric seismic source and micro-seismic monitoring array that was installed to monitor a portion of the planned sub-level mining of the Halo 5205 Level. The weak signal characteristics of the piezoelectric source necessitated the use of extensive data stacking for signal recovery at a distance. The experiment was to provide routine measurements of changes in source signal travel time. Measured over time, this would provide an in-situ study of the increased delay in the signal travel time, caused by the ray bending induced by the growth of the voids and fracture zones created by the mining process (Figure 1.3). Signal delay information was

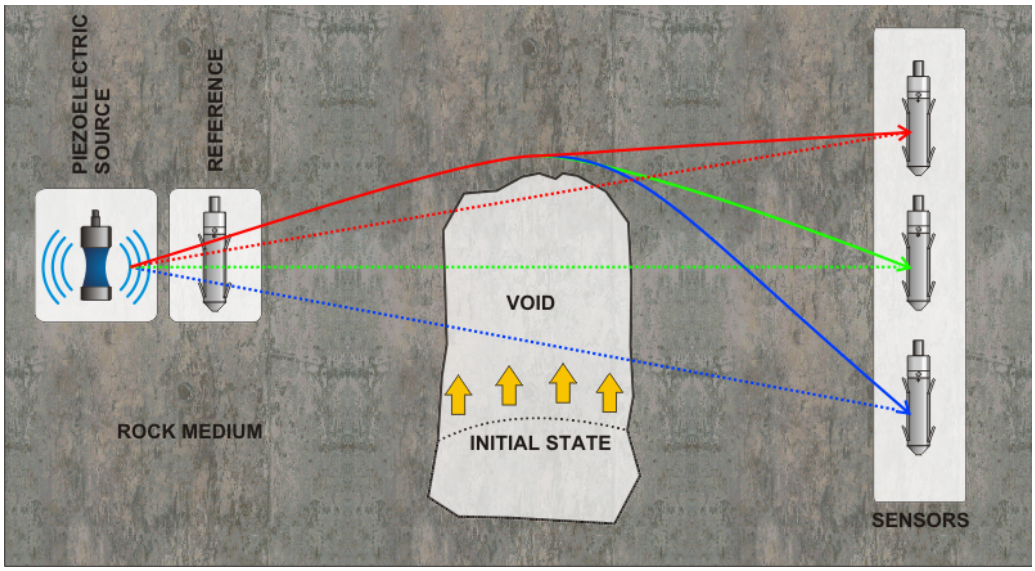

Figure 1.3: A cross-section that illustrates the basic concept behind the Cave Front Tracking Experiment. The initial state (represented by dotted curves) of the setup was characterised by straight ray-paths between the piezoelectric seismic source on the left and the seismic sensors on the right. A reference sensor was placed close to the source to measure the signal zero time. A seismic void was made to advance in between the source and sensors through mining processes, which forced the signal traveling between them to bend (solid curves). This resulted in an increased delay in signal travel time, the periodic measurement of which was used to determine the growth extent of the seismic void.

used to estimate the extent of mining advance which in turn was compared to the actual physical progression of the sub-level mining process.

Numerical modelling of the same sub-level mining process was conducted using third party software called E3D [25, 49] which modelled dynamic seismic wave propagation. Survey and mine production information provided by the mine was combined with planned experiment installation information and used to build numerical models of the Halo 5205 Level mining process. This modelling was used create an understanding of the effects of ray-path bending on the signal and the expected degree of signal travel time variation over the course of the mining process.

The 5205 level was chosen due to the opportunity to make use of instrumentation that had already been permanently installed to monitor the 5235 level using active seismics. Unfortunately a drop in the ore grade, towards the end of the mining cycle, prevented the sub-level mining from reaching and interacting with the source-to-senor ray paths in any significant way.

Seismic Velocity Experiments

A number of experiments have been performed in the past which made use of active seismic sources to measure travel time changes over extended periods. A number of these these were aimed at measuring the minute velocity variations caused by changes in the bulk medium originating from environmental factors such as changes in hydrostatic pressure, tidal strain, atmospheric pressure and temperature changes and stress and strain influences as a result of mining or regional tectonics. Past experimentation has indicated

a fairly large range of velocity-stress sensitivity as well as varying degrees of influence attributed to the different contributing factors.

Several experiments were conducted in the 1970s to continuously and precisely measure changes in stress by relating it to measured changes in velocity. Reasenberg and Aki [41] were among the first to measure extremely small changes in seismic signal travel times using an airgun seismic source in an experiment conducted in 1971 (however the work was only published in 1974). These variations were attributed to tidal strain induced velocity variations measured from Raleigh surface waves generated by the airgun, covering a distance of 200 m. The authors calculated a maximum velocity variation of up to half a percent which suggests a much higher sensitivity between stress change and medium velocity. At the time, the authors attributed this to thin cracks in the granite body in which the experiment was conducted.

A similar experiment was performed by Leary et al.[27] who used an marine airgun, fired in a reservoir once every 5 days to measure seismic velocity variations over distances of up to 8.5 km. Recording was performed over several periods, starting in 1974 and spanning two years. In their experiment, no net change in P-wave travel time was observed, despite a regional increase in shear strain of $\sim 2 \times 10^{-7}$ per year originating from the San Andreas-San Gabriel fault systems. However, they did observe a systematic fluctuation that varied in period from hours to days. Daily temperature and Earth tide effects were deemed only partially responsible for observed fluctuations, which were interpreted as the effect of water filling cracks which open due to incremental strain. However these fluctuations appear to occur faster than the diffusion time of water into newly opened cracks.

Other seismic velocity variation experiments were conducted over much shorter baselines, using high frequency active sources. Galdwin [16] performed continuous measurements of the seismic velocity of a ultrasonic pulse in a rock support pillar at a depth of 700 m in an active mine, which covered a distance of 10 m. The same pillar was instrumented with capacitance strain sensors and the pillar was subjected to large scale stress relief process. Velocity change, $\Delta v/v$, is measured with a precision of 2×10^{-6} which resolved stress changes in the order of 1 kPa. These findings showed that the degree of velocity variation with change in stress at depth to be much lower than that seen in previous experiments such as conducted by Reasenberg and Aki.

A more recent experiment was conducted by Niu et al. [37] in 2005 at the Parkfield San Andreas Fault Observatory at Depth drill site (SAFOD) which investigated the velocity-stress coupling at seismogenic depth. Stress changes were measured through continuous monitoring of seismic velocity of ultrasonic pulses, installed at a depth of ~ 1 km, between two boreholes separated by 10 m. The use of modern monitoring equipment and highly repeatable piezoelectric seismic sources improved the timing error to 1 part in 1×10^7. The S-wave coda was used to calculate the time delay, rather than first arrivals, as it is more sensitive to velocity changes [46]. Their work revealed an inverse relationship between the change in barometric pressure and travel time delay, a phenomenon which was also observed in near surface experiments. The effect of air pressure, pressing down on the rock mass caused an opening and closing of micro-cracks which varied as the air pressure changed. An apparent deviation from this relationship prior to two large earthquakes which occurred several kilometers away was unexpected. The authors put forward the hypothesis that there is a prior and sudden change in elastic moduli before a large rupture which supports the idea that continuous stress monitoring may prove useful in anticipating large events which is particularly important to the underground mining environment.

Much of the inspiration for the technology and methods used for the Cave Front Tracking Experiment was drawn from the work conducted by Niu et al. at SAFOD.

Chapter 2

Experiment Setup

2.1 Project History

2.1.1 Phase One

The Cave Front Tracking (CFT) experiment reviewed in this report follows as a revision from a previous attempt which embodied the same experimental goals. This initial experiment, referred to as Phase One, aimed to track the mining progression of the Halo 5235 Level.

The Phase One experiment was designed using information gained from earlier active seismic source tests conducted in deep level South African gold mines which explored the practical nature of using a piezoelectric seismic source in conjunction with extensive data stacking in order to perform active seismic studies in a hard rock mining environment . These prior tests proved successful, and demonstrated that the seismic signal from a piezoelectric source could be recovered at a range of just over 200 m and that from this data it was possible to measure very small velocity variations ($O\left(10^{-3}\ \%\right)$). Other seismic sources available on the market at the time were investigated and considered either too costly or ungainly for the intended experiment.

Phase One aimed to take the technology one step further by introducing internal vertical pre-stacking on seismic data loggers, as opposed to a complex system of post-stacking which required huge volumes of continuously recorded seismic data. This pre-stacking was coupled with pulse-per-second (1 s) time synchronization system for both the piezoelectric source signal generator and the seismic data loggers in order to eliminate problems of relative device clock drift which was necessary to ensure constructive vertical pre-stacking (See Section 2.5.1 for more details on data stacking).

As it was the first long term experiment of its kind conducted by IMS, Phase One suffered a series of set backs that severely hampered it from producing any meaningful results before the level had been mined through. One issue in particular arose from having both the communications and seismic monitoring equipment installed on the same level in which mining was conducted. Numerous hardware failures were traced back to mining activities. Blasts conducted in particular crosscuts occasionally caused damage to the communications link to surface, halting the entire experiment due to the dependence on pulse-per-second timing attained from GPS time broadcast. Another consistent problem arose from the high concentration of diesel exhaust fumes generated by heavy loaders and haul trucks operating in the level. This lead to a build up of diesel exhaust particulate on electronics that were not contained in a sealed environment, which ultimately resulted in their failure. The early generation source driver electronics were particularly vulnerable to this problem as the particulate build up eventually caused its high voltage (450 V) amplifiers to short-circuit.

The very high levels of seismic noise generated by the heavy machinery and problems with unaided internal pre-stacking greatly hampered the recovery of the piezoelectric source signal. A weak signal recovery was achieved using data recorded from the closest sensor (3GU1), but reliable recording was not possible from sensors installed at distances greater than 100 m.

2.1.2 Phase Two

Much was learned from the first Cave Tracking Experiment and it was decided that the experience gained could be applied in monitoring the sub-level caving of the 5205 level (the level below 5235). It was decided to maximize on existing hardware already installed from the previous experiment. The redesign process aimed to address set backs suffered previously but was restricted by the less than ideal source and sensor array arrangement (Figure 2.1). This new arrangement meant that the full sub-level caving area would not be covered but the goal of tracking an advancing mining front could still be achieved for a portion of the intended extraction volume.

During the lead up to the installation of the experiment, two additional prototype seismic sources were selected for field testing at the Halo experiment site in the form of a pneumatically driven impact source and an electric eccentric rotating mass source. These additional sources were installed in short boreholes, set within a 1 m spacing from the piezoelectric seismic source so that the device performances could be easily compared. Refer to Figure *2.1* for a plan view of the instrumentation positioning while Figure 2.2 provides details on the communications layout.

Installation of the Phase Two of the experiment began on the 15th of October 2012 and pre-stack data recording began on the 28th November of the same year. Recording was halted on the 4 April 2013 due to a damaged fibre optic cable which resulted in the loss of timing communications. Recording was resumed on the 6th June 2013 after repairs and a minor modifications to the experiment setup were completed. Data recording was again halted on 24th October 2013 following a piezoelectric source driver upgrade and was subsequently resumed on the 2nd November 2013 and remained ongoing until 2 June 2014 when all seismic data recording was terminated.

2.2 Sensor Array

Seismic sensors are devices that are used to measure seismic vibrations by converting ground motion into a measurable electronic signal. Ground motion can be measured using a number of different sensor types, the choice of which depends on the intended application. The most common type is the geophone which measures ground velocity using a coil and magnet system [36]. Accelerometers which measure ground acceleration are also routinely employed.

The sensor array consisted of ten seismic sensors (Table 2.1 as well as Appendix A and B) positioned in four different boreholes, the majority of which were originally installed for CFT Phase One. These original sensors comprised four tri-axial geophones (L2G - L5G) and an accelerometer (L1A) installed in a 48 m long horizontal borehole L, while an a single tri-axial geophone (U1G) was installed in an vertically orientated 10 m deep borehole U, placing it outside of the caving zone. These sensors which were positioned to monitor the caving progression of the 5235 level and thus the ray paths between source and sensor would only be intersected by the 5205 sub-level cave in the latter half of the mining cycle.

In order to reduce the planar distribution of sensors, an additional three tri-axial geophones (D1G - D3G) were installed in an inclined borehole D which dips towards the

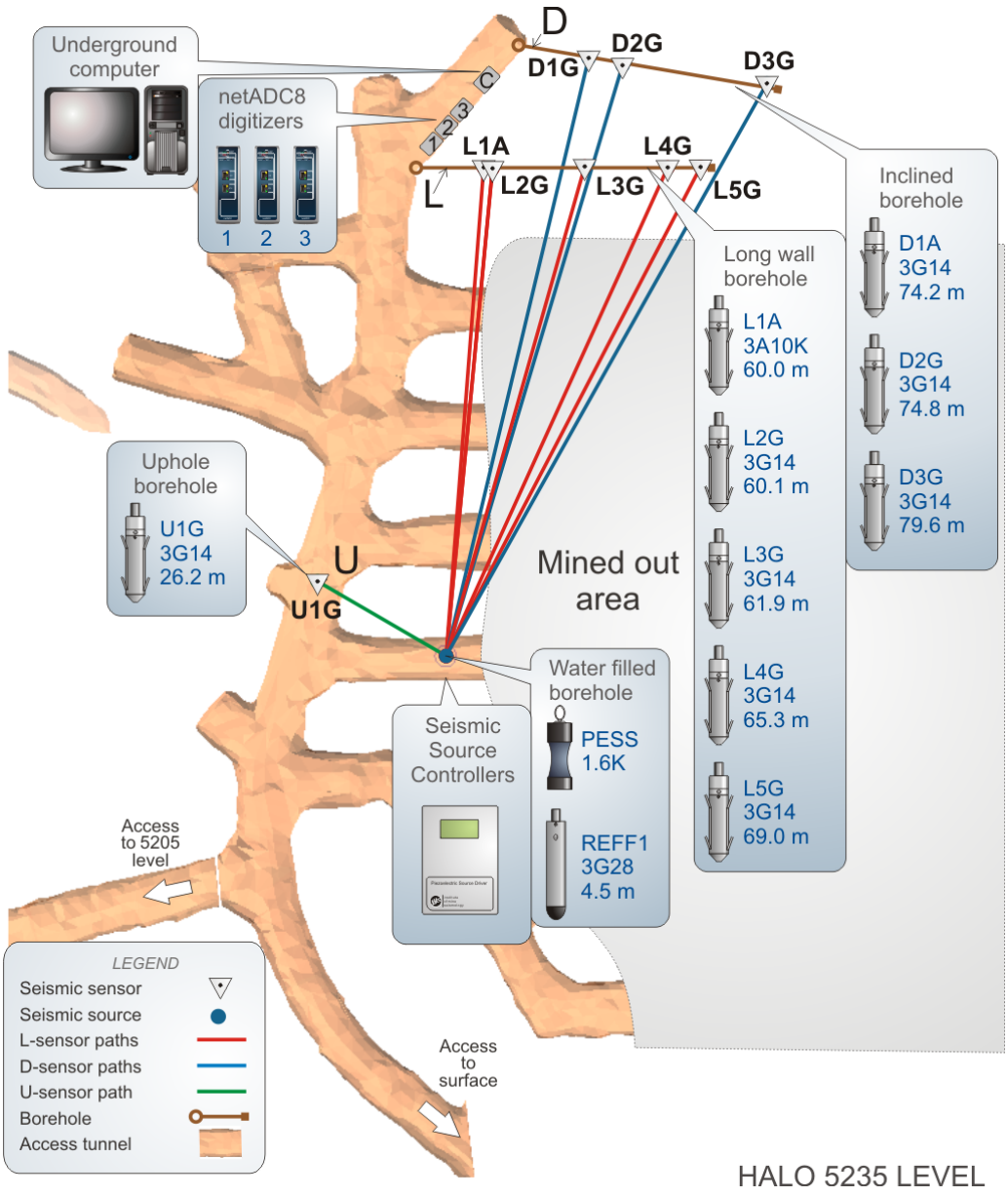

Figure 2.1: A illustration depicting the layout of the Cave Front Tracking experiment at Ridgeway Mine on the 5235 Level. The seismic monitoring array covered a portion of the sub-level caving progress of the 5205 Level (level below). Sensors were installed in two boreholes, holes L and D. An additional up-hole sensor was installed in hole U. Three IMS netADC8 digitizers and a central site computer were installed in Crosscut 9 at the end of the 5235 access drive. The piezoelectric source was installed to a depth of 8 m in a water filled borehole, drilled from Crosscut 4 on the 5235 level.

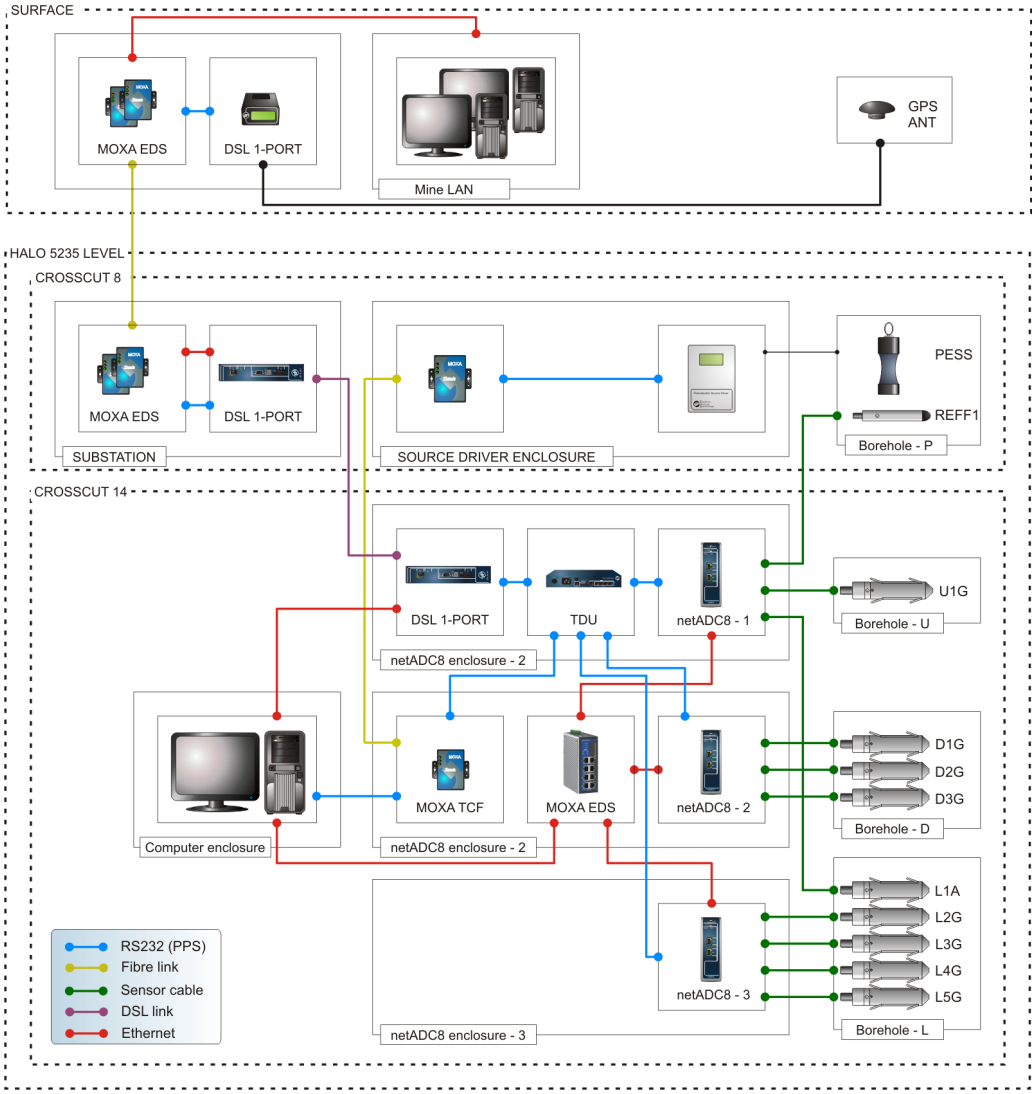

Figure 2.2: A systems layout diagram that details the communications between hardware used in the Cave Front Tracking Experiment. Ethernet and timing signals were transmitted from surface using a fibre optic link, carried to an underground substation. Communications were then relayed using an IMS DSL link to the experiment site on the Halo 5235 Level. IMS netADC8 units were linked to the central computer through a Moxa EDS308 switch, using standard CAT5 Ethernet links. The Pulse-Per-Second timing was distributed using an IMS TDU which further relayed to the source driver using a two-way fibre optic link.

Figure 2.3: A typical tri-axial borehole geophone manufactured by IMS for use in underground mines. Nine such geophones and an two accelerometer sensors where installed in boreholes at the Halo Cave Front Tracking experiment.

No.	Name	Type	X (m)	Y (m)	Z (m)	Distance (m)
1	PESS	Piezoelectric	10814.2	22772.8	5227.1	N/A
2	PNEU	Pneumatic	10814.2	22772.3	5231	N/A
3	ERM	Eccentric Rotating Mass	10813.8	22772.3	5232	N/A
1	R1G	28 Hz Geophone	10814.2	22772.8	5233.1	6
2	U1G	14 Hz Geophone	10798.9	22781.7	5248.4	26.2
3	L1A	10 kHz Accelerometer	10818.9	22831.7	5237.8	60.0
4	L2G	14 Hz Geophone	10819.9	22831.7	5237.8	60.1
5	L3G	14 Hz Geophone	10830.9	22831.7	5237.8	61.9
6	L4G	14 Hz Geophone	10840.9	22831.7	5237.8	65.3
7	L5G	14 Hz Geophone	10844.9	22831.7	5237.8	69.0
8	D1G	14 Hz Geophone	10831.5	22844.8	5529.3	74.2
9	D2G	14 Hz Geophone	10835.5	22844.0	5226.4	74.8
10	D3G	14 Hz Geophone	10852.9	22841.7	5217.2	79.6

Table 2.1: A list of the seismic sources and sensors installed at the Cave Front Tracking Experiment Site at Ridgeway Mine. XYZ values are provided in the co-ordinate system used by the mine. Straight ray distances between the piezoelectric source and sensors are listed in the last column.

5205 level below at an angle of 30° from horizontal, providing the array with a vertical distribution.

Finally, a geophone was installed close (4 m) to the seismic sources to serve as the timing reference of the active sources (Figures 2.1 and 3.8). An additional reference sensor was later installed to compliment the existing one after changes in the reference signal were detected following extended periods of monitoring.

2.3 Seismic Data Acquisition

2.3.1 IMS GS and Internal Pre-stacking

Digitization and capture of seismic data was achieved using IMS digital seismometers. The first phase of the experiment saw the use of four GS units, sampling a total of 24 channels at a rate of 48 kHz. The high sampling rate was necessary for the precision required to study possible stress induced velocity variations, and so the experiment would generate huge volumes of data over its intended one year operation. The first technique employed to contend with the extensive data volume was the use of internal vertical pre-stacking that reduced 5 minutes worth of seismic data down to a single second long seismogram (Section 2.5.1).

These GS units ran a special version of their data acquisition code that performed continuous vertical pre-stacking of consecutive second long data buffers, outputting a single stacked file every 5 minutes. In other words, the GS would digitize a second's worth of data and then add that data to a stacked buffer, also a second in length. This was performed for all 6 recording channels per unit. Once 5 minutes worth of stacked data was recorded, the stacked buffer was saved to an external storage device and the stacking process would start again. Data from all four units was transmitted to a central control computer, also stationed underground on the same level and data was archived and made available for transfer to servers in Stellenbosch, where the data could be further analyzed.

Full continuous data was specifically recorded and was used to ascertain why the piezoelectric signal recovery was not achieved using stacked data recorded by the GS, despite the successes of previous underground experiments which covered similar or larger distances [32, 34, 31]. The investigation revealed that unaided vertical pre-stacking was partially responsible, which prompted the redesign of the data acquisition system for the study of the 5205 level.

2.3.2 IMS netADC and Aligned Stacking

Experimental data attained during Phase One revealed small temporal variations in the piezoelectric signal generation which prevented successful internal pre-stacking at the seismometer. A new generation of seismometer became available at the time of the Second Phase, the IMS netADC8 (Appendix A). This device performed analogue to digital conversion of the recorded seismic signal but differed from its predecessor by transmitting the data over Ethernet to an appropriate processing device, instead of trying to process the data itself using seismic triggering and association algorithms. This feature provided flexibility in how and where the seismic data could be processed.

Seismic data stacking was transferred to a central computer which was better suited to the computationally intensive task of collating, scanning and stacking the data. Centralizing the pre-stacking task to a single computer provided ease of control and monitoring of the ongoing data collection and stacking process.

Three netADC8s sampling 8 input channels at a rate of 48 kHz were setup to feed raw seismic data directly to the central computer over Ethernet. Time synchronization was achieved using analogue time updates (ATU) generated by the computer once every minute while the piezoelectric source driver continued to rely on Pulse-Per-Second (PPS) timing. Figure 2.2 provides diagrammatic details on the communications layout.

The IMS software required for full continuous data recording was not ready at the time of installation of the experiment. Instead a special data handling program was written that would capture waveform Ethernet packets and then to reconstruct the recorded waveform by inserting the seismogram packets into their respective positions in time and

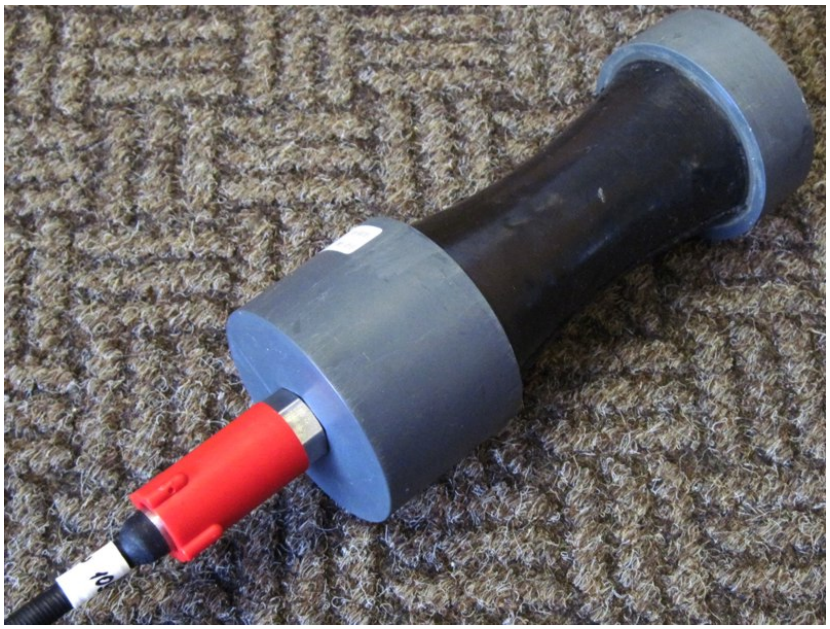

Figure 2.4: An SRX-1 piezoelectric active seismic source used in the Cave Front Tracking experiment. It was designed to operate underwater and so required a water filled borehole. Its low power output necessitated the use of data stacking techniques in order to boost the effective range of the device so that it could cover the baseline distances required by the Cave Front Tracking Experiment.

recording channel within a minute long buffer for all 24 channels. Once the all continuous waveforms were reconstructed, the full waveform was then processed and stacked using cross-correlation techniques, as discussed in Section 2.5.

2.4 Active Seismic Sources

2.4.1 Piezoelectric Seismic Source

A Sensortec SRX-1 piezoelectric transducer was used as the experiment's active seismic source. The particular source was designed to operate underwater and to generate signals within the human audible range. It was chosen over other commercially available transducers due comparatively low resonant frequency - a desirable characteristic for a seismic source due to the frequency dependent attenuation of seismic transmission. A piezoelectric source has a very low power output compared to other available seismic source types [14] giving it a low detectable range. However the device has the advantage of producing unique signals that can be repeated at a rapid rate while operating for extended periods (due to low mechanical stresses), which made it ideally suited for data stacking techniques (Section 2.5). Correctly executed data stacking was used to boost the effective range of the piezoelectric source many times over in a number of past active source experiments [37, 34, 31].

2.4.2 Piezoelectric Source Driver

Piezoelectric transducers require high voltages in order to produce the maximum change in volume and so require specialized high voltage signal generators. The IMS piezoelec-

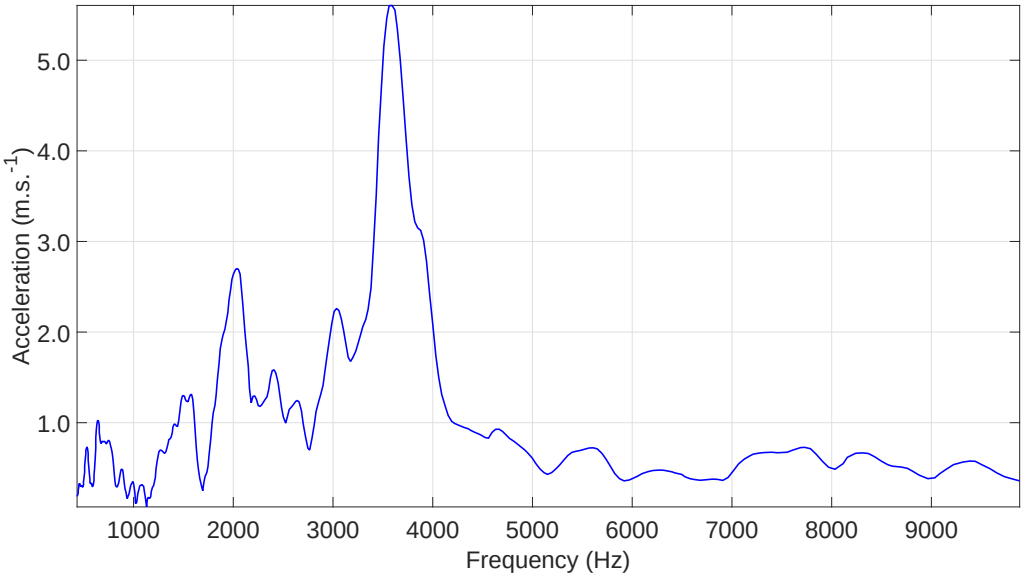

Figure 2.5: A frequency sweep response test conducted on the SRX-1 piezoelectric source between 100 Hz and 10 kHz. The source was driven using a continuous sine-wave with a steady frequency increment over a fixed duration. Source response was measured using a 25 kHz accelerometer sensor, posited 3.5 cm from the source and connected to an IMS netADC8 sampling at 192 kHz. The dominant resonant mode was found at 3590 Hz while the second highest resonant mode was found at 2050 Hz.

tric source driver was designed to generate Ricker-Wavelet pulses which are amplified in voltage, while also maintaining time synchronization with the rest of a seismic monitoring network (Appendix A). In order to derive the maximal power output from the Sensortec piezoelectric source, the source driver was configured to operate the unit at its second resonant mode of 2050 Hz, and near half its optimal duty cycle (~60%) by generating three Richer-wavelet pulses per second (3 Hz) with a peak-to-peak voltage of ±900 V.

PPS timing signals were used to maintain accurate clock synchronization of the source control electronics with that of the internal clocks of the netADC units. Accurate time synchronization was important, not only for knowing when a source pulse was generated in time but crucial for internal pre-stacking to succeed. (Section 2.5.1). As the experiment had initially been designed around the concept of internal pre-stacking for Phase One, the driver was programmed to only fire the source when it had reliable time synchronization and would cease operation when PPS was lost.

2.4.3 Pneumatic Seismic Source

Tests conducted into the feasibility of using hammer impacts as a means of locating trapped miners showed that well placed sledge hammer impacts could be detected over a distance of 250 m within a working mine environment while also producing fairly repeatable seismograms. This made the heavy mass impact seismic source an appealing concept to expand on and so the idea of pneumatically operated impact device was conceived. Many mining environments readily have access to high pressure air supplies which is routinely used for mining operations.

The prototype source, simply named the Pneumatic Seismic Source, used high pressure

Figure 2.6: Piezoelectric Source Driver Type 2 used at the Ridgeway Cave Front Tracking Experiment. The driver unit featured serial communications to facilitate GPS time synchronization and internal temperature and pressure reporting. The unit was configured to drive a SRX-1 piezoelectric source with a 2050 Hz Ricker-wavelet pulse, generated at a fixed rate of 3 pulses per second.

gas to propel a 3 kg mass or slug within a tube over a distance of 2 m to impact against a solid metal surface. This makes its seismic signature similar to that of a heavy hammer impact.

As the motion of the mass or slug is identical each time the device is fired, so the seismic signal generated was expected to be highly correlated between shots, making the device suitable for stacking techniques similar to that employed with the piezoelectric source. This aspect, coupled with a considerably stronger seismic signal output strength, would make it a longer range source when compared to the piezoelectric source.

In order to field test the device a working prototype was grouted in a 3 m long vertical borehole at the Halo Cave Front Tracking site and operated to test its reliability, seismic signal strength and signal reproducibility. As it was the first installation of the device in any mine environment, mechanical reliability was of particular concern and so an endurance testing scheme was devised whereby the device was be fired once every hour until it showed signs of failure which would be detected using the seismic monitoring array.

Control of the device's firing or discharge mechanism was achieved using a set of four electronically controlled actuator valves configuration that would fire the slug upward (bottom to top) and then six seconds later, fire it downward (top to bottom) returning the slug to it original starting position.

Figure 4.4 provides an example of shots recorded from the pneumatic source installed

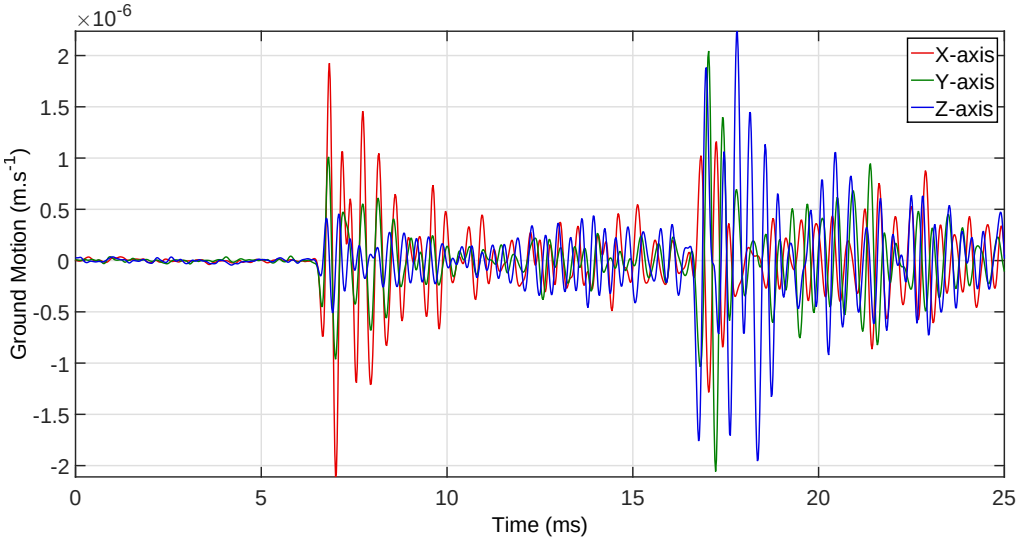

Figure 2.7: A seismogram of a single test shot signal generated by the prototype Pneumatic Seismic Source recorded by sensor D2G.

at Ridgeway. The overlaid shots show a strongly repeated seismic signal with a signal-to-noise ratio of approximately 9, recorded by sensor D3G positioned 79.8 m away from the source.

2.4.4 Eccentric Rotating Mass Seismic Source

An eccentric rotating mass (ERM) seismic source differs from the other two seismic sources by producing a continuous sinusoidal seismic signal as opposed to a single discrete pulse. The particular ERM source installed at the Halo Cave Front Tracking Experiment operated using a 1 kW brushless motor to spin a set of off-center masses at 200 revolutions per second, generating a 200 Hz sinusoidal vibration. Like the pneumatic source discussed in Section 2.4.4, the ERM source was grouted into a short vertical hole to ensure a solid coupling between the device and surrounding rock.

As the signal generated by the EMR source was a continuous monochromatic signal, recorded waveforms were not suitable for analysis using time domain based cross-correlation methods discussed in Section 2.5. Such monochromatic waveforms could be analyzed in the frequency domain by measuring the phase angle of the real and imaginary parts of the Fast Fourier Transform. However calculating the actual rock velocity between source and sensor was problematic due to the periodic nature of the sine function as well the problem of phase mixing caused by P- and S-wave separation [19].

Oscillatory type seismic sources are employed in the Oil and Gas Exploration industry but are operated in a manner that produces unique signals through techniques such as signal chirping and M-sequencing [12, 17, 43] instead of a signal which is purely monochromatic. Unfortunately the ERM source installed could only be operated at a single frequency and was installed simply to test the seismic signal strength output. Like the pneumatic source, it was under investigation for possible future use as a seismic source alternative. Seismic records and analysis results from the ERM installed at Ridgeway can be found in Appendix G.

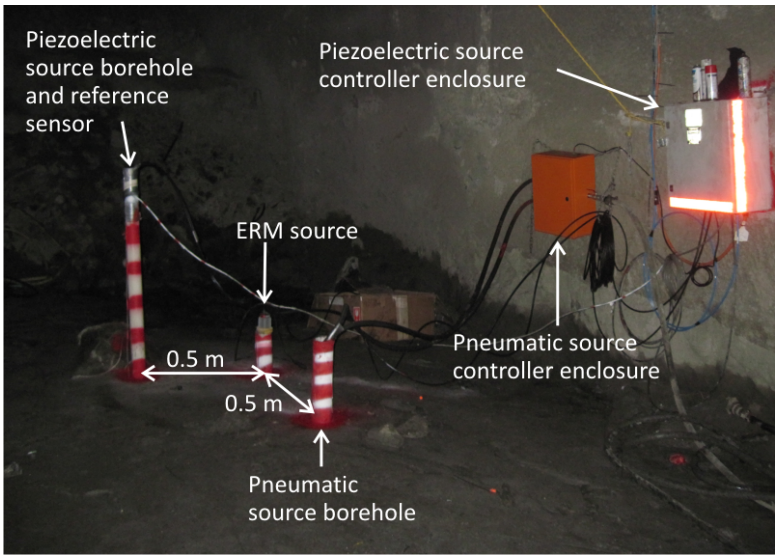

Figure 2.8: The three different seismic sources installed on at Cave Front Tracking Experiment site at Ridgeway Mine. The piezoelectric source was installed in a water filled borehole to a depth of 8 m while the ERM and Pneumatic sources were installed to depth of 3 m. A control unit was required for both the pneumatic and piezoelectric sources, housed in steel enclosures mounted nearby. A fiber optic communications link provided the PPS timing signal to the piezoelectric source controller to ensure accurate clock synchronization with the rest of the seismic monitoring array.

2.5 Data Processing

2.5.1 Seismic Data Stacking

Seismogram data stacking was an integral part of the technology and data analysis required for the Cave Front Tracking experiment because of the large source-to-sensor distances, ranging from 27 to 80 m (see Figure 2.1 and Table 2.1) compared to the basic 20 m range afforded by the piezoelectric source.

Data stacking is the technique of adding two or more measurements of the same subject signal together in order to compound the measurement and increase the amplitude of the recorded signal. Alternatively it can be thought of as an averaging of multiple measurements of the same type in order to reduce the contribution of random influences. In the case of a digitized waveform, the stacking of two or more similar waveforms, A, is the per-sample superposition or addition of all individual records expressed as:

$$U_n\left(t_i\right) = A_1(t_i) + A_2(t_i) + ... + A_n(t_i)$$

where:

- U_n is the stack comprised of the superposition of n number of individual discretized signals, A_i.
- t is the waveform times series, which is local to each waveform and does not refer to an absolute time.
- i is the array index of each waveform time series, with $i \in [0, m-1]$ and $i \in \mathbb{N}$.
- Waveforms U and A are comprised of the same number of samples, m.

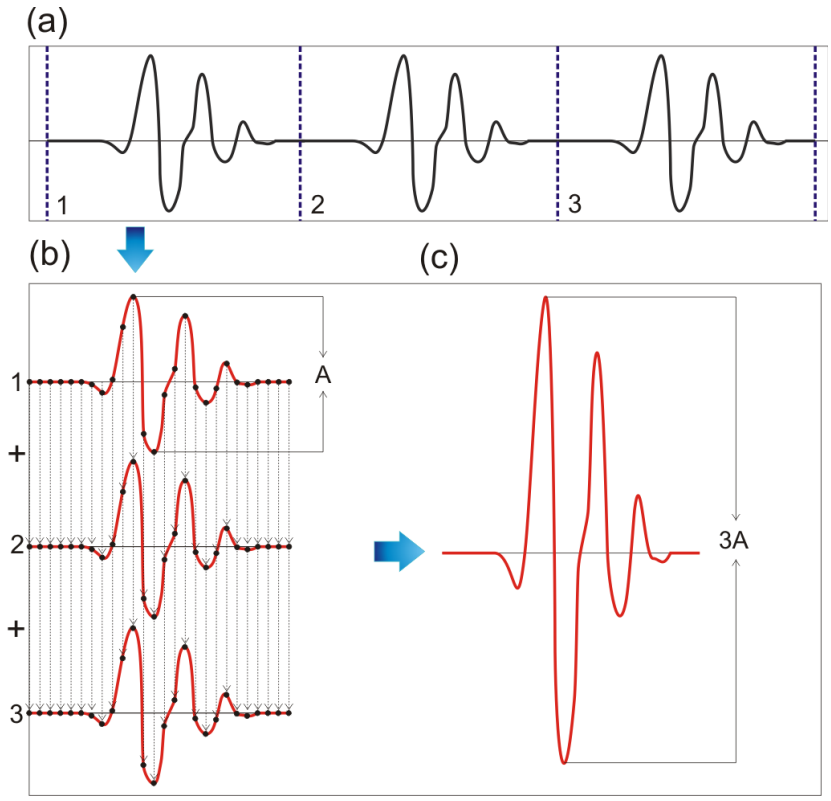

Figure 2.9: A simple description of waveform stacking. A set of repeated waveforms from a repetitive source are divided into equal length segments that contain an individual waveform (a). Each of the individual samples from the respective waveforms are added to the samples in the other waveforms with the corresponding array position (b). The resulting output is a waveform that is n times the amplitude of the individual waveforms, where n is the number of waveforms stacked (c).

This straight forward signal stacking is referred to as vertical stacking [23] and the process is only beneficial when the two or more waveforms that are stacked contain near identical signal patterns with the two signals aligned in phase. Stacking of two such waveforms will simply result in the same waveform with double the amplitude. Thus stacking any multiple of the same signal results in a factor n increase in the stack signal amplitude, where n is the number of signals stacked (Figure 2.9). Stacking can be performed on waveforms of different array lengths but would require specific array indexing in order to ensure constructive amplitude growth.

Digitized seismic signals will typically contain signal noise which originates from electronic noise and background ambient seismic vibrations which contaminant the recorded seismogram and can obscure the details of a signal of interest. Recorded ground motion G_i can be thought of as the superposition of both a specific deterministic seismic signal A (in this case the signal generated by the active seismic source) and stochastic noise, N, such that $G = A + N$. Recorded noise is predominately random in nature. Stacking such random influences will result in an reduced averaging of the two or more sections of noise as no two segments will be characterized with either the same waveform pattern or be aligned in phase. It can be empirically shown that stacking perfectly random white Gaussian noise (a fair approximation of electrical noise) will see a $\sqrt{n}$ mean increase in

signal amplitude (Figure 2.10).

Stacking of seismograms that contain both phase aligned signals and noise will result in a signal amplitude growth of a factor n while the noise only grows by a factor $\sqrt{n}$. The signal-to-noise ratio (SNR), defined as:

$$SNR = \left(\frac{A_{\text{rms}}}{N_{\text{rms}}}\right) \tag{2.1}$$

where rms is the root mean square definition $A_{\text{rms}} = \sqrt{\frac{1}{m}\sum_i^m A_i^2}$. SNR thus grows by a factor $n/\sqrt{n} = \sqrt{n}$ [23, 37, 32]. The portion of the seismogram that was typically used to calculate the noise level N_{rms} in this investigation, was the recording taken just prior to the arrival of the signal while only the portion of the signal used to calculate the phase delay was used to calculate signal level, A_{rms} (Figure 4.11).

The effective increase in signal over noise will not only increase the quality of the resulting signal but can also be used to recover a signal with an amplitude that was originally much smaller than the amplitude of the noise. This translates to a boost in the effective range of a source device whereby measurements can be made over distances much larger than the basic range provided by the source and receiver pair. This principle was employed to great effect with the piezoelectric source, which was well suited for data stacking techniques.

The goal of the experiment was the calculation of travel time variations attained through the measurement of phase delays in active source signals arriving at the various sensors. The lower bound accuracy of these measured phase delays were dependent on the quality of compared signals, a relation which was expressed using a simplified form of the Cramér–Rao lower bound, originally applied by Niu, et al. [37, 45]:

$$\sigma_{DTE} \geq \frac{1}{2\pi f_0 (SNR)} \tag{2.2}$$

The dominant signal frequency f_0, was determined by the driving input signal which was fixed by the programming of the source driver and matched to the resonant frequency of the source at 2.05 kHz. For a repeatable source like the piezoelectric or pneumatic source the SNR can be improved through data stacking, which in turn improved the minimum phase-delay resolution, further highlighting the importance of the technique.

Strong seismic noise generated by mining operations on the level below, primarily the drilling of blasting boreholes, created periods with significantly high noise levels. Simple vertical stacking of such periods contributed negatively to the noise mitigation when compared to quiet periods. To help contend with such noisy signals the seismogram was subjected to an amplitude scaling that was based on the seismogram's average noise value [23]. This seismogram weighting significantly reduces the contribution of noisy records to the stacking process. Since the duration of noisy periods may vary greatly, the time duration required to record enough data to achieve a desired SNR will vary as well. In addition to the weighting scheme, a cutoff was also be applied where records with noise values beyond a certain threshold were rejected altogether.

An optimal solution for stacking seismograms with varying degrees of noise can be established by characterizing the noise levels of each signal under consideration for stacking. These noise values are then sorted in ascending order and a function of noise growth calculated in relation to the n growth factor expected for the signal. Only the records that will produce the highest gain in SNR are then stacked.

While correct stacking will produce a positive growth factor it does however have diminishing returns as achieving higher SNR's require exponentially greater volumes of input data. For an experiment with a fixed signal generation rate, this means a non-linear relation between the recording interval required in order to achieve a desired SNR

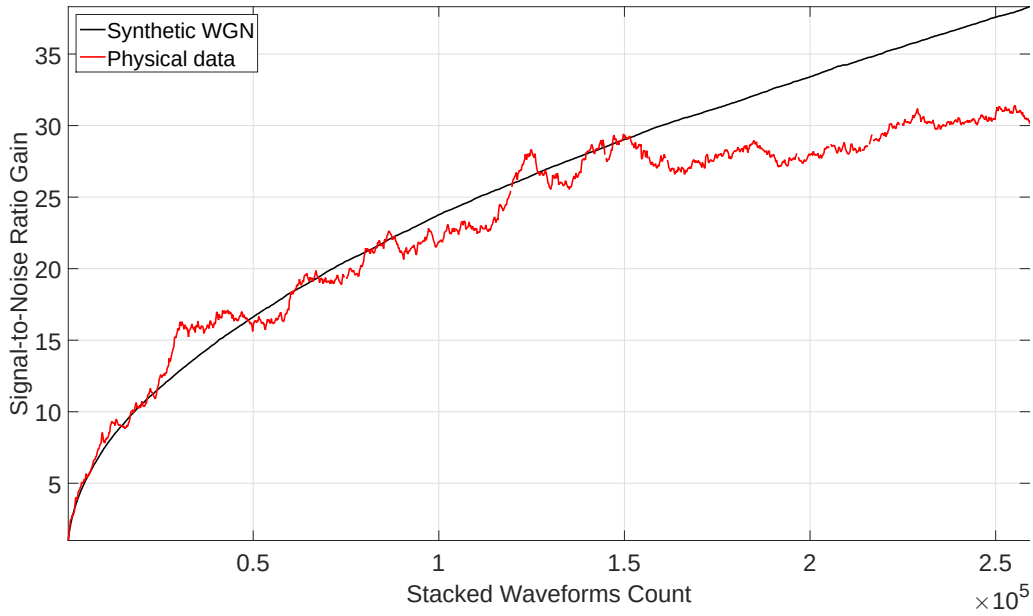

Figure 2.10: The SNR growth history that resulted from stacking data over the period of a typical working day (259200 shots) using data recorded by the Cave Front Tracking Experiment. This was compared to the stacking of synthetic data comprised of white Gaussian noise. Periods of slow growth in the experiment corresponds to periods of very high noise caused predominantly by drilling (see Figure 2.11).

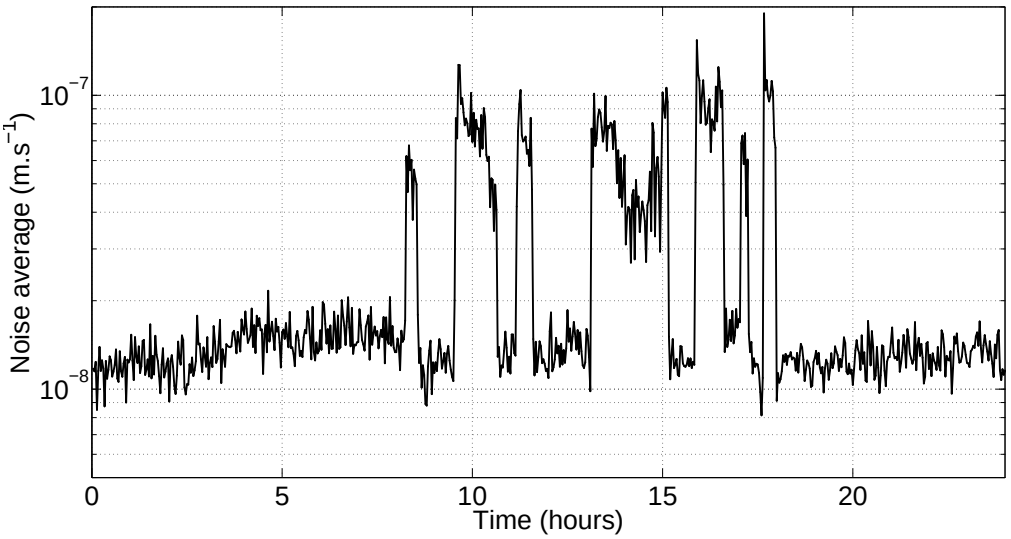

Figure 2.11: An example of the noise levels recorded by the Cave Front Tracking experiment over a period of 24 hours. Drilling blasting boreholes created periods with noise values that are typically an order of magnitude greater than quieter periods. Such periods contribute negatively to the stacking process, which necessitated the use of a weighted stacking scheme that was based on the seismogram's noise levels.

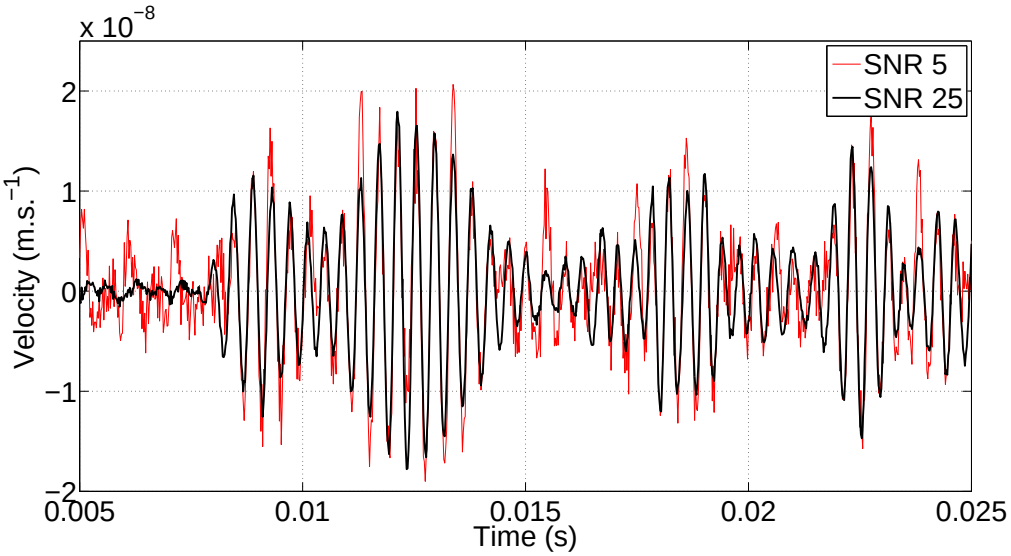

Figure 2.12: An example of the increase in signal-to-noise ratio as a result of signal stacking. The red curve denotes a stack that has a SNR of 5 while the black curve has an SNR of 46. A SNR of 5 was attained after stacking of 5760 shots whereas an SNR of 32 required 236160 shots. This considerable difference in the volume of data required is a result of the $\sqrt{n}$ growth rate of SNR through stacking and the minimal contribution from periods of high noise (See Figures 2.11 and 2.10). Scaling the amplitude of the stacks by applied weighting factors creates the effect of the noise shrinking with relation to the signal. Data was attained from the sensor D3G which was 79.6 meters from the source.

for each stack. This in turn affects the interval between when velocity variation measurements could be made (Section 2.5.6). In certain cases the elapsed time between such measurements may be of a longer period than that of the phenomenon under investigation, such as the stress relaxation after blasting. In order to reduce the time duration between measurements, an overlapping time window scheme was used. In such a scheme, stacks would share data with neighboring stacks, which had the effect of smoothing the calculated travel time variation history.

2.5.2 Waveform Cross-Correlation

Calculating the phase or time difference between individual stacks, in order to measure a signal delay change, was achieved using a time domain based sliding window cross-correlation by searching for the point of best fit alignment. The likeness of two seismograms of equal length are compared to each other using the standard normalized cross-correlation function between two waveforms:

$$C\left(F,G\right)=\frac{1}{m}\sum_{i}^{m}\frac{\left(F(t)-\overline{F}\right)\left(G(\tau)-\overline{G}\right)}{\sigma_F\sigma_G} \tag{2.3}$$

Where:

- F is the reference waveform, G the comparator waveform.

- t and τ are the time series which defines what section of the seismograms are compared. For a digitized waveform, $F(t_i)$ and $G(\tau_i)$ are the amplitudes of the seismogram at time t_i and τ_i respectively.
- $\overline{F}$ and $\overline{G}$ are the mean values of the waveforms of $F(t)$ and $G(\tau)$ respectively.
- σ_F and σ_G denote the standard deviations of the respective waveforms, were $\sigma_F = \sqrt{\frac{1}{m}\sum_i^m \left(F(t_i) - \bar{F}\right)^2}$.
- m is the total number of samples in time series t and τ, where $F(t)$ and $G(t)$ have equal lengths.

In order to find the point of optimal alignment between two phase shifted yet similar waveforms, a sliding time window form of τ is needed (Figure 2.13). In the sliding window scheme τ is defined by:

$$\tau(k) = t + t_{offset} = t + k \cdot \Delta t \tag{2.4}$$

The cross-correlation function is then expressed in the specific form:

$$C\left(F, G\right)\left(t_{offset}\right) = \frac{1}{m}\sum_i^m \frac{\left(F(t_i) - \overline{F}\right)\left(G(t_i + t_{offset}) - \overline{G}\right)}{\sigma_F \sigma_G} \tag{2.5}$$

Where:

- t_{offset} is the applied time shift to G with limits defined by a maximum positive and negative phase lag $\pm t_{offset-max}$.
- Δt is the inter-sample period of the discretized waveforms.

For a discretized waveform t_{offset} is a multiple of Δt, which gives $t_{offset} = k \cdot \Delta t$ with k an integer multiple and $\frac{-t_{offset-max}}{\Delta t} \leq k \leq \frac{t_{offset-max}}{\Delta t}$.

Reasonable limits must be defined for $t_{offset-max}$ to account for the largest possible signal delays while avoiding the search for unrealistically large phase shifts. Cross-correlation was performed for each time window $\tau(k)$ in order to build a cross-correlation cost function $C(k)$, starting from a negative phase lag and progressing through to a positive lag using regular steps in time, Δt. The phase lag of optimal alignment between the reference and comparator waveforms was attained by taking the phase lag that corresponded with the point of maximum in the sliding window cost function, defined by:

$$C\left(k\right) = \frac{1}{m}\sum_i^m \frac{\left(F(t_i) - \overline{F}\right)\left(G(t_i + k\Delta t) - \overline{G}\right)}{\sigma_F \sigma_G} \tag{2.6}$$

and measured signal phase lag φ, between F and G, is given in time by:

$$\varphi = k_{\max(C(k))}\Delta t$$

The normalized cross-correlation provides a measure of waveform similarity between -1 to 1, where -1 is anti-correlated, 1 would be perfectly identical waveforms while values closer to zero are uncorrelated or dissimilar. This normalization made it easy to define generalized correlation value thresholds for the purpose of deciding whether waveforms were similar or not.

All seismograms recorded by the various digitizer units during the physical experiment were inserted into a waveform collection that shared a common time. A phase offset that was calculated for the reference sensor could thus be applied to all recorded seismograms for all sensors in the array.

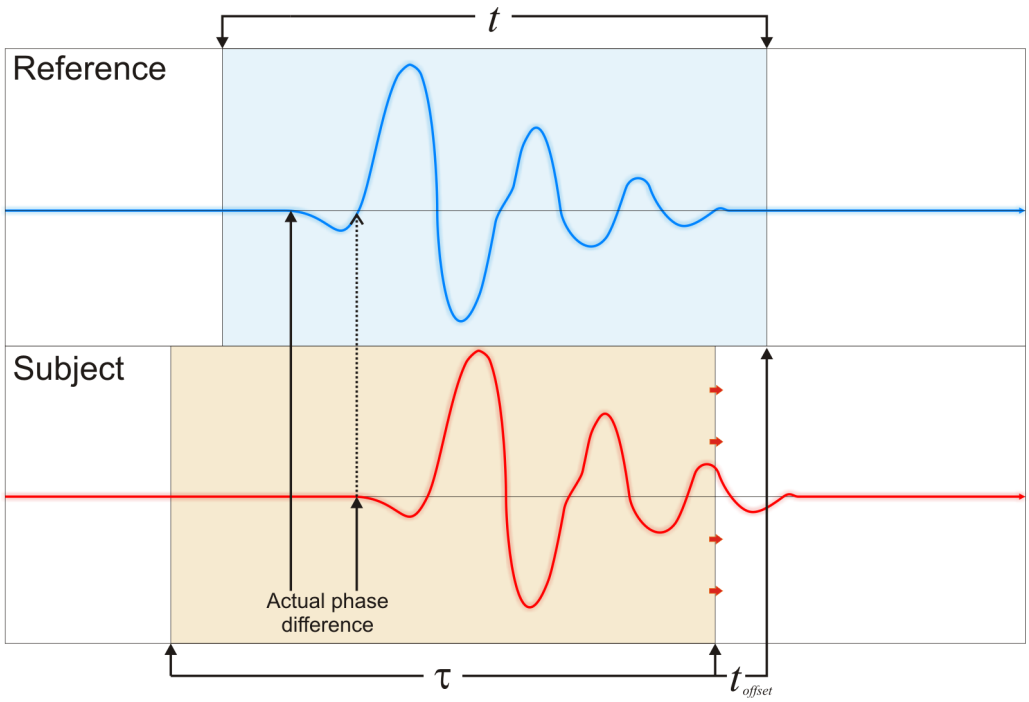

Figure 2.13: An illustration that defines the features of the sliding window phase lag calculation process. The reference waveform was a predetermined signal master copy with a fixed duration t. The subject waveform was compared to the reference using a section of the waveform defined by $\tau_i = t_i + t_{offset}$. A cost function of the two waveform's similarity as function of phase shift was created by performing the comparison over the series values of t_{offset} which cover both positive and negative phase lag values. The t_{offset} value which corresponded with the maximum point in the cross-correlation function was the chosen phase lag between the reference and subject waveform.

The sliding window cross-correlation was used to perform three important tasks during the data processing of the experiment. First, as means to correctly identify when a piezoelectric signal was recorded in the continuous data stream (Section 2.5.4). Second was the calculation of the point of optimal alignment of waveforms for constructive stacking (Section 2.5.1). Thirdly it measured the time lag between two or more stacks which was used create long term travel time variations 2.5.6.

2.5.3 Sub-sample Phase Determination

Blasting sub-level drawbells resulted in a signal path length increase which was larger than the time separation afforded by the sampling rate of the data acquisition system. For example a face advance that caused a 1 meter change in the P-wave signal path length resulted in a phase delay increase of 1.75×10^{-4} s, much larger than the inter-sample period of 2.08×10^{-5} s when recording at 48 kHz (Section 3.6.1).

In contrast, extremely small changes in the seismic velocity were expected from changes in the local stresses acting on mining region, which translates to extremely small changes in the signal phase lag [18, 32, 41, 4, 16, 27, 21, 31, 37, 45, 38]. The shortest straight line distance between source and sensor distance was 26.2 m which required a minimum time resolution of 4.6×10^{-8} s in order to resolve stress changes in the order

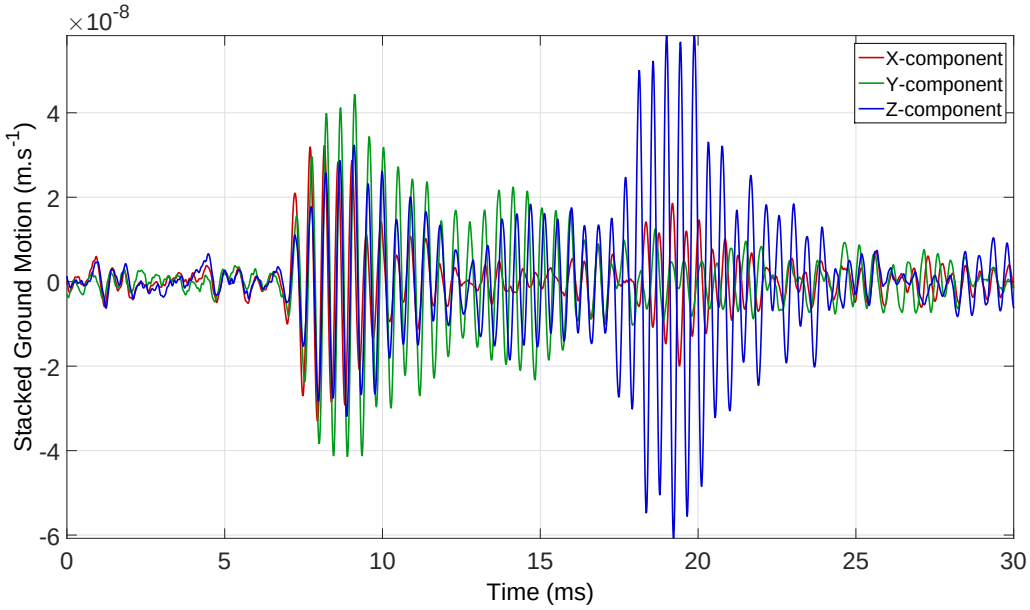

Figure 2.14: An example of the stacked piezoelectric signal measured at Sensor D3G. The stack was created using data recorded at midnight on the 1st of December 2013. The signal shows a monochromatic characteristic, which is particularly strong on the Z-component of the sensor.

of 1 kPa, measuring P-wave velocity changes and assuming a stress coupling at depth of 10^{-8}/Pa [32].

However the Cramér–Rao lower bound 2.2 restricts the smallest time difference that can be resolved when applied to example stacks shown in 2.14.

A dominant frequency of 2050 Hz and a SNR of 50 (Figure 2.15), resulted in a best case resolution of 1.6×10^{-6} s, which was only sufficient for measuring stress variations in the order of 100 kPa - a change that was quite possible from mining induced activities. This best case resolution however, was an order of magnitude smaller than the digitization sampling rate. To increase the inter-sample resolution needed in order to reach this lower bound resolution, signal oversampling was required which was achieved using a cubic spline interpolation function (Appendix C).

The measurement of stress variations was not the primary objective of the experiment, however its successful measurement would help to verify the working sensitivity of the experiment as well as served as a potential investigation into the application of the piezoelectric seismic source for measuring stress variations in the working mining environment [32]. Further studies of this phenomenon could have a significant bearing on mining safety where the detection of changing stress conditions may serve as a forewarning of an imminent seismic event or pillar failure [37].

2.5.4 Signal Identification

The first step of the stacking process was the identification of the desired signal within a continuous waveform recording. This was achieved using the signal recorded by the reference sensor, which was installed at a 4 m distance from the source. Unlike the other sensors in the array, the reference recorded a signal with extremely high SNR. The output

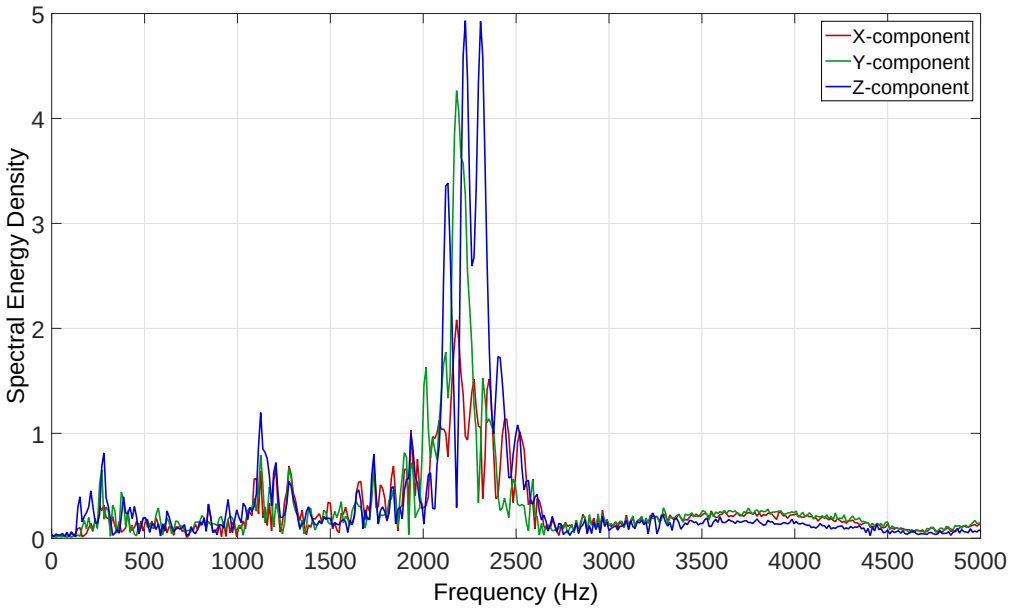

Figure 2.15: A plot of the spectral energy density calculated from a stacked seismogram of Sensor D3G. A peak in energy density was observed between 2000 and 2400 Hz for three axial components. A smaller energy distribution was also observed at 1250 Hz, which was the first resonance frequency of the SRX-1 piezoelectric source.

signal generated by the piezoelectric source (Figure 2.17) had distinctive peaks which were programmatically identified using a threshold and local maximum/minimum locater.

A specific threshold value was chosen and each portion of the waveform that exceeded the threshold was considered as a possible signal peak. Each threshold crossing is marked based on weather it was the start of a crossing or the end and the local maximum (or minimum, depending on the chosen threshold) between these two point is marked. From this marked point, a window was created and the contained section of waveform was extracted compared to a predefined master waveform using a short sliding-window cross-correlation. Waveforms that correlated highly with the reference waveform were considered a valid signal generated by the source (Figure 2.16) and tagged for stacking.

The correlation value attained provided a measure of the signal similarity while the phase lag that was measured was used to correct phase miss alignment before stacking the signal.

2.5.5 Pre-stacking Procedure

The large data volumes recorded by the experiment necessitated the process of pre-stacking data before committing it to long term storage. Phase One of the Cave Front Tracking Experiment had shown that unaided vertical pre-stacking did not result in sufficient SNR gain. The revised pre-stacking method instead employed a full waveform reconstruction, signal identification and alignment such that all waveforms were first time shifted by any phase-shift measured using the reference signal before any stacking was performed.

Stacks were created using one minute long sections of data (containing 180 source pulses), starting and ending on the edge of the clock minute. All signal identification and alignment was performed using the reference sensor data (Figure 2.17), which was high-

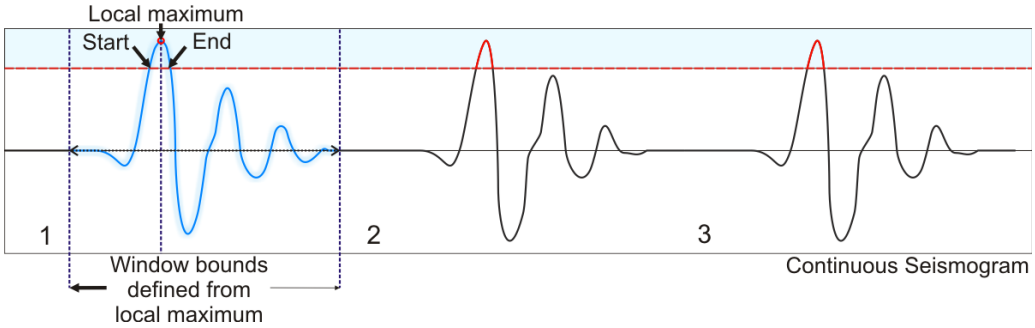

Figure 2.16: An illustration that details the signal identification process in a continuously recorded seismogram. A suitable threshold was defined which only intersected with the largest peak in the shot signal pattern. Seismogram regions between threshold crossings were considered and local maximums found for each region. From this local maximum point, a window was defined and the contained section of the seismogram was applied to a sliding window cross-correlation against a known signal reference to identify whether the section of seismogram was a valid signal or not.

pass filtered to remove unwanted low frequency influences such as 50 Hz electrical mains interference and heavy vehicle activity. Due to the noise generated by ongoing mining activity, signal pulses were occasionally dropped as a result of low correlation values or failed identification using the threshold method.

Data output consisted of a single set of 24 waveforms, 2350 samples in length at sample rate of 48 kHz, each comprised of stacked data recorded during periods when the piezoelectric source had fired the in respective minute. This reduced one minute worth of continuous data recording, totaling 6.912×10^7 samples, down to 5.64×10^4 samples which was a significant reduction in data storage usage. However, the continuous data was considered of interest for future investigation using ambient noise correlation techniques [21, 9, 38] and so provision was made to store the continuous data in a down-sampled 16-bit format.

2.5.6 Post-stacking and Travel Time Variation Calculation

Pre-stacked data was transferred from the Underground Computer to IMS servers where further data analysis and processing was performed. Full signal recovery was not achieved for all sensors after stacking one minutes worth of data, thus data was post-stacked using overlapping stacking time periods. Investigations into suitable stacking schemes showed that a common stacking period for all channels was suitable. Fixed periods in time were used to create stacks that spanned a total of 4 hours, with an shared data overlap of 1 hour. This resulted in post stacked waveforms with a 3 hour separation, or 8 waveforms per day. Similar to the pre-stacking procedure, a single master signal recorded by the reference sensor was used to determine if any time shift corrections should be applied all wave-forms before post-stacking.

After post stacks were created for a particular time period, signal time lags were calculated for all sensors (including the reference). A data flow and processing diagram for the physical experiment can be found in Figure 2.18. Phase lag calculations were performed independently for each recording channel, which allowed meaningful comparison of differences measured for different axial components of the same sensor. Because fixed stacking periods were used, certain post-stacks were unsuitable for comparison, either due to a lack of data or particularly noisy data within its defined stacking period. This

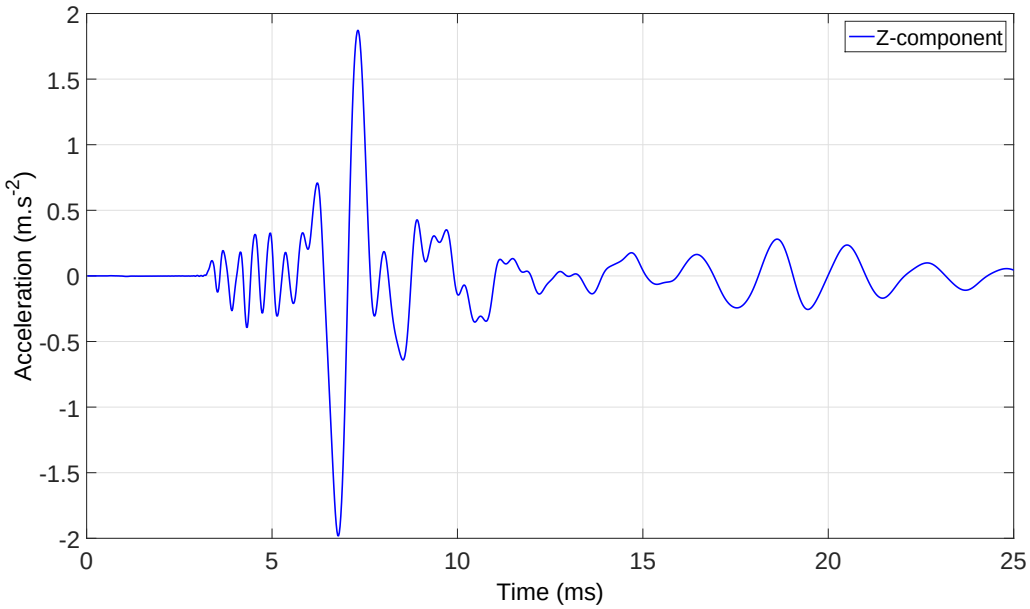

Figure 2.17: An example of reference signal recorded by an accelerometer sensor suspended in the piezoelectric source borehole. A short high frequency burst is followed by a lower frequency large amplitude double swing.

resulted in gaps in the calculated time variation history. Time variation histories were plotted and compared to the blasting schedule provided by the mine.

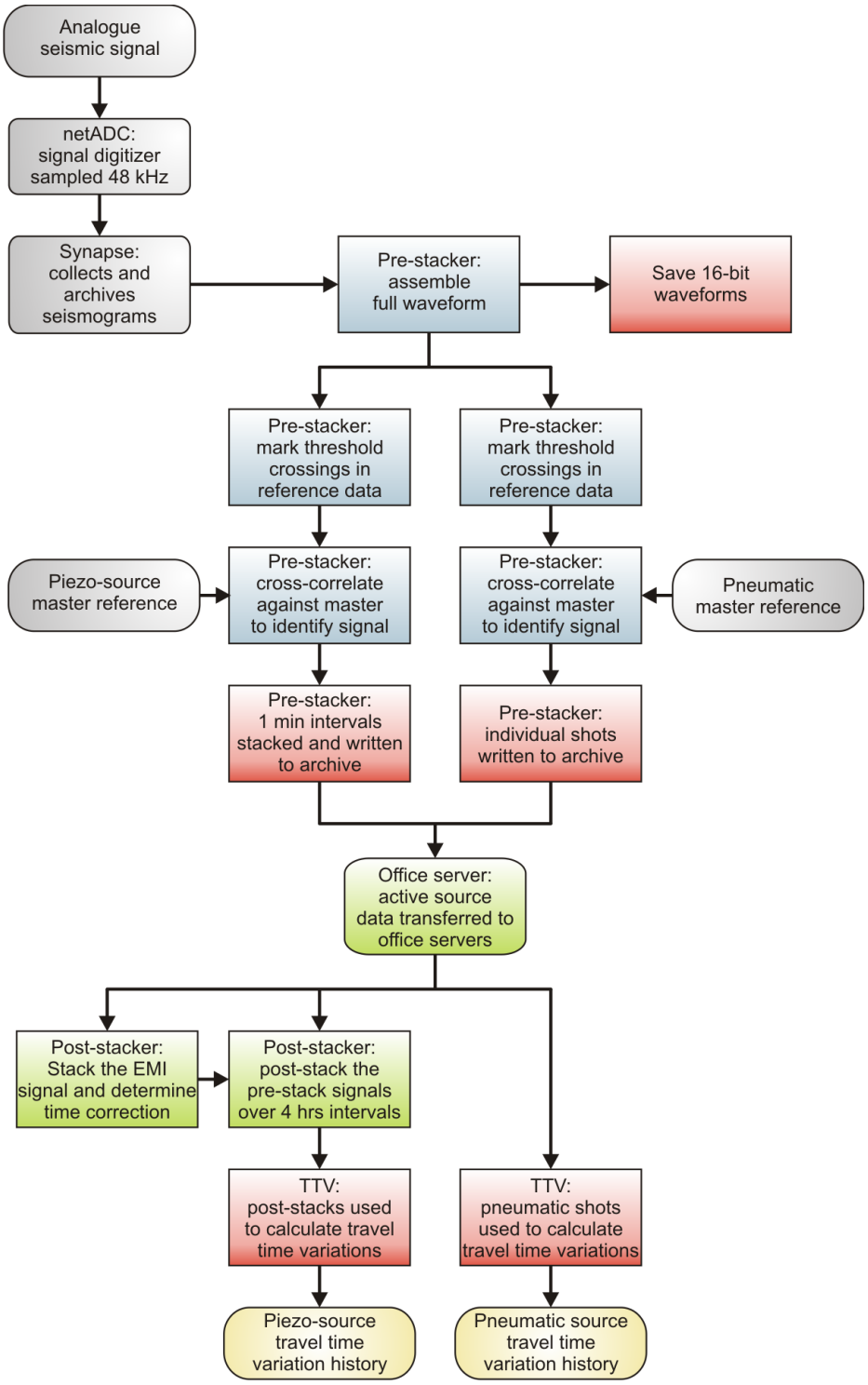

Figure 2.18: A data flow diagram that details the procedure taken for processing active source seismic data recorded by the Cave Front Tracking Experiment. The process starts with the continuous recording of the analogue signal for all seismic sensors which was digitized and logged to a central computer. Piezoelectric and pneumatic source signal identification was performed on reference sensor data and valid signals were vertically stacked using one minute intervals of source data. Stacks are then transfered to office side servers for timing correction and further stacking. the resulting stacks are used to calculate travel time variation histories for all sensors.

Chapter 3

Modelling

3.1 Introduction

A better understanding of the effect of sub-level cave mining on the local medium and the changes its causes to seismic wave propagation can be achieved by numerically modeling the mining process. Dynamic wave modeling is routinely used to study seismic wave propagation through complicated media, particularly in crustal seismology and seismic exploration utilized by the oil and gas industry. As a consequence there are many third party seismic wave numerical modeling programs available that would be suitable for this study.

This investigation employed the use of the E3D seismic wave modeling package which has been used extensively by IMS to study the interaction and behavior of body waves with underground and open cast excavations. E3D is an explicit 3D (or 2D) elastic finite-difference wave propagation code used for the modeling of seismic waves originally developed by Shawn Larsen from Lawrence Livermore National Laboratory. It is 2nd-order accurate in time (using the Taylor series expansion approximation of the first derivative) however its staggered grid implementation allows it to be up 4^{th}-order accurate in space. It is based on the elastodynamic formulation of the wave equation on a staggered grid [15, 35, 29, 47, 48].

Modelling using E3D provided additional insight into how the seismic signal arriving at the various sensors changed as the mining on the 5205 Level progressed, as well as the challenges that were faced when attempting to invert for the mining front advance. In addition to the E3D modelling, second order Fast Marching Method was also implemented and was used as a source of comparison for calculated signal delay changes caused by mining advance. Fast Marching Method times were subsequently used to create a look up table which was employed in the modelled mining front inversion process.

3.2 Modelling Difficulties

3.2.1 Seismogram Rotation

Initial modelling using E3D revealed that the significant ray-path bending caused by large changes in the medium geometry as a result of mining, created noticeable changes to waveform patterns. Phase-lag calculation accuracy was hampered by this progressive change in the seismogram signature as the process relied on cross-correlation techniques (see Section 2.5.2) and high waveform similarity. Reduced travel time delay accuracy in turn affected the accuracy by which the mining front could be estimated.

The changes in seismic void geometry resulted in a several factors that contributed to the observed signal changes, namely changes in reflection interfaces, apparent wave

rotation and the mixing of different ray-paths. Lower frequencies being less affected by small enough voids may also have played a part.

The majority of these effects contributed to changes in the latter part of the seismogram or coda, thus in order to reduce the complexity of the investigation only the initial portions of the P- and S-wave first arrivals were considered. In this regard, the apparent wave rotation (a direct result of ray-path bending) was the most prominent of these phenomena at work. As the seismic wave was forced to bend around an expanding void, it experienced an increase in travel time (due increase in path length) as well as a change in the direction from which wavefront arrived at a fixed position on the other side of the void due to path bending (Figure 3.1).

Physical seismic sensors elements only function along a single axis and thus a tri-axial sensor with three perpendicular components is required to measure the full seismic body waves which are three-dimensional in nature. Any changes in the direction of arrival results in a change in the ratio of the amplitudes recorded by the axial components of a seismic sensor which subsequently causes a change in the overall seismogram shape. For example, a source and receiver pair in a homogeneous medium, aligned along the X-axis will record all P-wave vibrations on the sensor's X-component and nothing on the Y- or Z-components. However, if a void were placed in between the source and sensor, the ray would be forced to bend around the void and arrive at the sensor at an angle to the X-axis, resulting in P-wave vibrations that maybe recorded by all three components, depending on the incident angle. This component mixing is enough to cause problems with the phase-determination process and so a seismogram rotation scheme must be included in the phase-lag calculation process.

In order to compensate, seismograms must be rotated to the local coordinate system of the wave arriving at the sensor which effectively rotates the sensor to face the wave front. This provides recorded waveforms with a common orientation with respect to the recorded wave. Seismogram rotation is commonly used in signal processing and seismology when studying earthquakes. The three components of the wave are rotated using a standard 3D rotation matrix.

The back-angle of the wave (direction from which the wave approached the sensor, relative to the sensor) could be determined through the use of principle component analysis.

P- and S-waveforms are part of E3D's output which provides the equivalent of a seismogram that had been rotated to account for the direction of the wave. Seismogram rotation was therefore not implemented for waveforms generated using E3D.

It should also be noted that the measured back-angle of the wave could be used when attempting to invert for more complicated void shapes, as the direction of arrival of a ray will shed some light on the geometry of the medium it was forced to bend around.

3.2.2 Waveform Stretching

Simplified model tests using a 2.05 kHz Ricker wavelet source (Section 3.5.2) and homogeneous velocity model showed that seismograms taken at large distances would produce stretched waveforms (in the time domain) when compared with waveforms taken closer to the source. The degree of waveform stretching or decrease in frequency was dependent on the travel time between source and sensor, meaning the greater the distance and the slower the medium velocity, the greater the degree of waveform stretching. This posed a problem as the modelled mining process was characterized with increased signal travel time which resulted in waveform stretching. This hampered the accuracy of phase-lag calculation process as the cross-correlation method (Section 2.5.2) is ill suited for the purpose when comparing waveforms which differ in pattern by a degree of stretching.

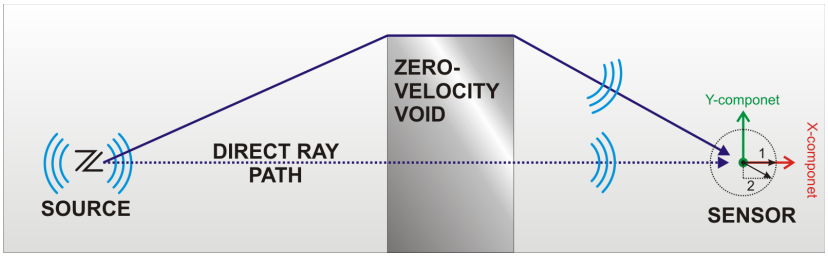

Figure 3.1: A diagram that illustrates the effect of apparent seismogram rotation that results from significant ray bending. Relative to the orientation of the sensor, all the P-wave energy, travelling along the direct ray-path (dashed line) will be measured by the X-component of the sensor, indicated by vector 1. The wave travelling along the bent ray-path ray-path (solid line) arrives at the sensor in a direction which is at an angle to both the X-component and Y-component of the sensor, resulting in the measurement of P-wave by both components, indicated by vector 2.

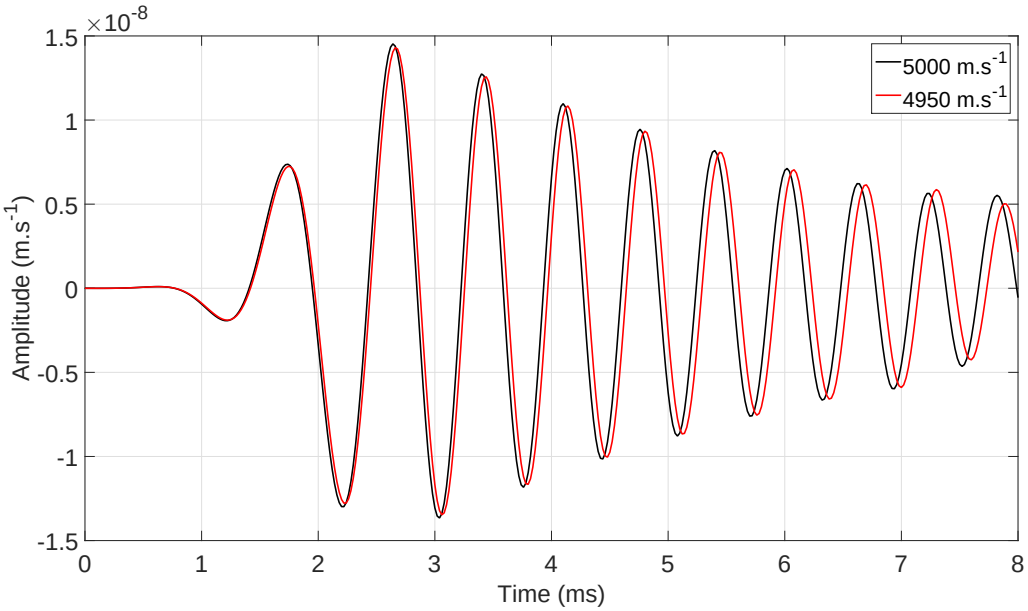

Figure 3.2: An example of waveform stretching for high frequency waveform modelled using E3D following 1 % change in velocity or increase in travel time. A homogeneous velocity medium was used and model attenuation disabled. Waveforms are phase shifted to align arrival times.

This effect was originally attributed to frequency dependent attenuation, a parameter normally included to model energy absorption of an imperfect material through friction and inelastic scattering losses. This anelastic damping is expressed by the following equation [36, 26, 1]:

$$A(t) = A_0 e^{-(\pi f/Q)t} \tag{3.1}$$

and similarly related to signal path length:

$$A(x) = A_0 e^{-(\pi f/Qv_p)r} \tag{3.2}$$

Where:

- Q is the dimensionless intrinsic attenuation characteristic known as the quality factor.
- A is the wave displacement or amplitude as a function of time or space.
- A_0 is the amplitude of the wave at some origin point.
- t is the travel time from its source of origin.
- f is a particular frequency that comprises the wave.
- v_p phase velocity of the particular frequency.
- r is the distance the wave has travelled from it source of origin.

Quality factor Q is analogous to the concept of energy loss in a oscillatory type electric circuit. The fractional energy loss per oscillation ΔE, is related to Q and the wave elastic energy E by [30]:

$$\frac{2\pi}{Q} = -\frac{\Delta E}{E} \tag{3.3}$$

The number of oscillations that wave undergoes is dependent on the distance that the wave has traveled, r and the wave length, which relates to the medium velocity and wave frequency, $v = \lambda f$. Higher frequency waves will contain a higher number of oscillations when covering the same distance as wave with a lower frequency, meaning it will undergo a higher degree of anelastic attenuation.

In order to attain equations 3.1 and 3.2 it is assumed that the attenuation is a linear phenomenon for all frequencies as well as having a linear stress-strain relation such that the amplitude is proportional to the square root of the strain energy. Thus equations 3.1 and 3.2 only describes the attenuation of a linear elastic medium and does not take into account the complex behavior of an anelastic heterogeneous medium or attenuation through geometric spreading.

Attempts to minimize the frequency attenuation in the E3D such as increasing the corner frequency of the model's imposed attenuation curve as well as the Q-value of the medium had little effect. Specifically setting the model to ignore all forms of attenuation also had no effect which meant either that E3D has an intrinsic high frequency attenuation (possibly to avoid high frequency related numerical instability) or that it was some other unknown property of the modelling code that was causing a non-physical numerical artifact. E3D was not originally written with modelling high frequency sources in mind and indeed the only means of minimizing waveform stretching was to use low frequency sources.

As the stretching effect could not be avoided in the modelling, the effect had to mitigated in the cross-correlation process by stretching the comparator waveforms to best

match that of the reference wave while performing the phase-lag search. This was achieved using the same cubic spline interpolation method used to over sample waveforms for sub-sample phase lag determination (Section 2.5.3,) to either shrink or stretch a waveform as required.

The phase-lag calculation process thus became a minimization for the combination of signal phase-lag and stretching factor that resulted in the highest cross-correlation co-efficient between the comparator and reference waveforms.

3.2.3 Reference Scheme

Phase delay algorithms, which focused on measuring subtle sub-sample changes caused by very small deviations in seismic velocity were not well-suited for signals subjected to large degrees of ray-bending due to the effect of the change in signal signature.

The use of seismogram rotation to account for ray bending was not sufficient to completely correct the deteriorating cross-correlation values attained when compared against direct ray-path seismograms.

Exploration into different reference schemes suggested that a dynamic reference approach was more appropriate. Instead of using a fixed set of seismograms from the first modelled mined stage, the reference was updated using the seismograms from the previous modelling step. This method therefore only measured the phase delay between the previous stage and the next. The total the signal delay for modelled step k, for each sensor s was calculated by summing the measured delays for all previous steps:

$$\Phi_k^s = \sum_{i=1}^{k} \phi_i \tag{3.4}$$

The dynamic reference helped to contend with the changing signal patterns and had the added benefit of reducing the phase lag search window size which in turn helps reduced the number of false correlations with later parts of the seismogram.

The downside of this approach was that all phase delay measurements were dependent on all previous measurements and their accumulative associated error. Thus any errors made early on in the phase measurement process was carried through to succeeding measurements when calculating total signal delay.

3.3 Fast Marching Method

A Fast Marching Method (FMM) engine was implemented for the purpose of calculating waveform first arrivals travel time for a signal interacting with a particular shaped void. The FMM detailed by Sethian and Bærentzen [44, 7, 5, 15] which uses a second order approximation of the first derivative of the wave equation. This particular approach was chosen due to the increase in travel time calculation accuracy compared to the simpler first order approximation as well as the relative ease of implementation.

The benefit of using FMM was the significant difference in solution calculation time over that of E3D's full waveform calculation which became a concern when attempting to model a large number of different mining advance states. It also had the added benefit that it used the same discretized velocity grid created for E3D input models, requiring no further conversion schemes. Every time a particular mine model was generated both the E3D and the FMM engine were deployed.

3.3.1 Method Theory

What distinguishes the Fast Marching Method (FMM) from E3D is that the FMM algorithm only evaluates the travel time evolution of a monotonically expanding wave front as

opposed to modelling a full and complete wavefield. This consideration makes the FMM calculation simpler and faster as calculations need only concern grid points that make up the leading edge of the evolving wavefield or wave front.

As FMM is singularly concerned with the travel time of the wave front, it makes sense to describe the wave expansion not in terms of displacement but as a travel time front using geometric ray theory and the idea of rays that travel perpendicular to the wavefront [26].

A basic analogy of this idea is that of a free electron contained within an field. The speed and direction in which the electron moves is determined by the direction of the highest change in electric field potential or field gradient.

In the case of a travel time wave front the time gradient at any given position along the front, is equal to the local slowness (inverse of medium velocity) and the direction of maximum travel time change defines the direction of ray propagation. The Eikonal approximation (Appendix D) of the wave equation can used to describe this ray approach which this given by the Eikonal equation [44, 7]:

$$|\nabla T(\bar{x})| = \frac{1}{V(\bar{x})} \tag{3.5}$$

where:

- $\bar{x}$ is the spatial position vector, $\bar{x} = [x, y, z]$;
- $T(\bar{x})$ is the time of the wave front at position $\bar{x}$.
- $V(\bar{x})$ is the medium velocity (non-negative) at position $\bar{x}$.

A number of methods exist to evaluate the time gradient $|\nabla T(\bar{x})|$ however as the method is concerned with solving for a monotonically expanding wavefront, an entropy enforcing solution is employed, as discussed by Sethian [44]. The entropy enforcing solution ensures that the wavefront does not travel back on itself making the method unsuitable for interactions involving reflections.

$$|\nabla T(\mathbf{x})| = \sqrt{\max\left(-D_{ijk}^{+x}, D_{ijk}^{-x}, 0\right)^2 + \max\left(-D_{ijk}^{+y}, D_{ijk}^{-y}, 0\right)^2 + \max\left(-D_{ijk}^{+z}, D_{ijk}^{-z}, 0\right)^2} \tag{3.6}$$

where D_{ijk}^{+x} is the second order Taylor series approximation of the first derivative along the x-axis:

$$\dot{F}(x) \approx \frac{3f(x + 2\Delta x) - 4f(x + \Delta x) + f(x)}{2(\Delta x)} \tag{3.7}$$

and the sub indexes i, j and k refer to indexing of points along the travel time grid in the x, y, and z planes respectively. The superscript $+x$, denotes the right-hand (positive in x) forward approximation along the x axis, while$-x$ refers to the left-hand approximation (see Figure 3.3) and similarly superscript y and z refer to the derivatives along the y and z plane respectively. Δx is the grid spacing size.

The forward positive time contribution along the x-axis, at point ijk orD_{ijk}^{+x} is thus calculated by evaluating:

$$D_{ijk}^{+x} = \frac{3T(i + 2, j, k) - 4T(i + 1, j, k) + T(i, j, k)}{2\Delta x} \tag{3.8}$$

Equation 3.8 requires that both the first and second adjacent points in the positive x-direction are known, but it is possible that certain configurations arise where only the first adjacent point is known. In this case the first order approximation is required instead.

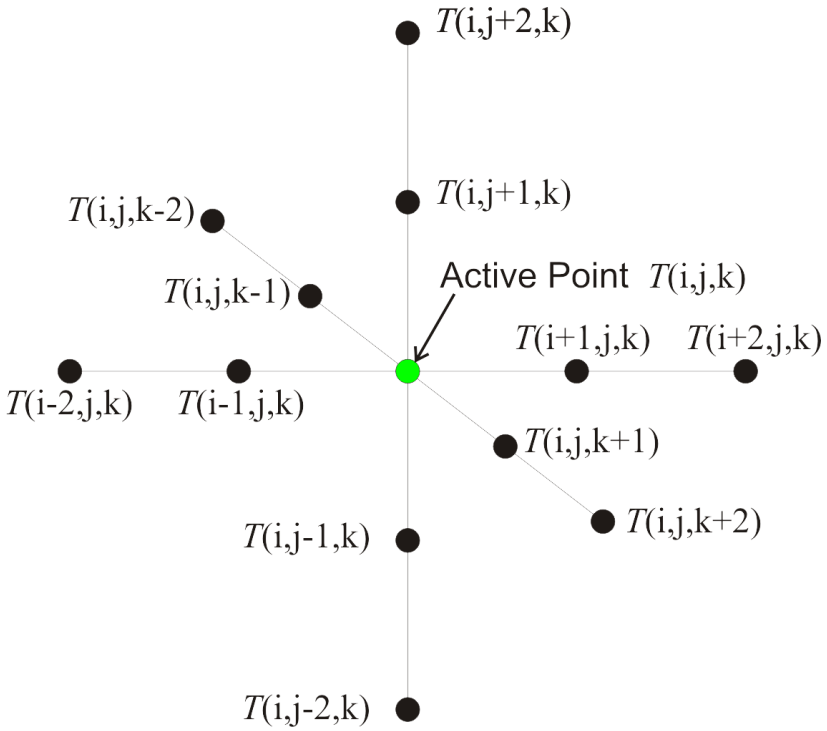

Figure 3.3: An illustration that defines the stencil pattern of grid points considered when calculating the wave front travel time at the active point $T(i,j,k)$ using the Fast Marching Method. The second order approximation uses the first and second adjacent points, while the first order approximation uses only the first adjacent point when calculating the forward partial derivative.

$$\dot{F}(x) \approx \frac{f(x+\Delta x) - f(x)}{\Delta x} \tag{3.9}$$

And so D_{ijk}^{+x} takes the following form:

$$D_{ijk}^{+x} = \frac{T(i+1,j,k) - T(i,j,k)}{2\Delta x}$$

It is necessary to compute and compare the left-hand approximation to the right-hand in Equation 3.6 and chose the maximum of the two in order to satisfy the entropy condition of an expanding wavefront.

$T(i,j,k)$ is the desired quantity and so by substituting 3.8 and 3.6 into the Eikonal Equation 3.5 and re-arranging, what remains is a quadratic equation. The coefficients of this quadratic will depend on the availability of grid points neighboring $T(i,j,k)$ and whether the first or second order approximations were used and which evaluation direction was chosen. Assuming that valid evaluations exist for the positive x, y and z directions then the equation can be expressed in the generalized form:

$$\begin{aligned}
\frac{1}{V^2(\bar{x})} &= \left[\left(\frac{\alpha + T(i,j,k)}{2\Delta x}\right)^2 + \left(\frac{\beta + T(i,j,k)}{2\Delta y}\right) + \left(\frac{\gamma + T(i,j,k)}{2\Delta z}\right)^2\right] \\
0 &= \frac{1}{2\Delta x}\left[3 \cdot T(i,j,k)^2 + 2(\alpha+\beta+\gamma) \cdot T(i,j,k) + (\alpha^2+\beta^2+\gamma^2) - \frac{1}{V^2(\bar{x})}\right]
\end{aligned}$$

where α, β and γ incorporate the contribution of neighboring points in the x, y and z directions respectively. The travel time value $T(i,j,k)$ is attained using the analytic solution to the quadratic, taking the standard definition $0 = a \cdot T^2(i,j,k) + b \cdot T(i,j,k) + c$:

$$\begin{aligned} T(i,j,k) &= \frac{-b \pm \sqrt{b^2 - 4ac}}{2a} \\ &= \frac{-2(\alpha+\beta+\gamma) \pm \sqrt{4(\alpha+\beta+\gamma)^2 - 12\left(\alpha^2+\beta^2+\gamma^2 - \frac{1}{V^2(\bar{x})}\right)}}{6} \end{aligned}$$

Only the larger positive solution to the equation is taken as the time solution cannot be negative or smaller than points that are already been calculated, for a causal expanding wavefront.

The specific process and computer algorithm implementation of the Fast Marching Method that was followed in order to calculate the travel time evolution of wavefront can be found in Appendix E.

3.3.2 Fast Marching Method Test Cases

A series of test cases were created to compare the relative accuracy of signal travel times calculated using the FMM engine versus analytic calculations and E3D's dynamic wave modeling. To simplify the process of measuring total travel time from E3D seismogram output, a simple Ricker Wavelet source was used (defined by equation 3.13 in Section 3.5.2).

Travel time was measured from E3D synthetic seismograms by locating the point of maximum in the P-wave output and subtracting the time lapse between source time function's starting time and point of maximum. A series of 18 sensors positions were used, 9 of which were regularly spaced along a horizontal line, while the remaining 9 were positioned along an inclined line. For the sake of consistency between the various test cases, the same source and sensor parameters were used for all tests.

The first accuracy test investigated simple spherical wave propagation through a homogeneous velocity medium, with the wave starting from a single point source. For such a simple case simple case, analytic, E3D and FMM travel times were computed and compared.

In the second test, a rectangular velocity void was inserted in between the source and sensors, which prevented a direct path and required the rays to bend. The void stretches from floor to ceiling, meaning that rays were forced to bend around the sides only. To calculate the analytic travel time, a series of geometric straight rays were used to map the shortest path taken to reach the sensors (See Figure 3.4 for details). Straight rays were projected from the source position to a point P1 located on the closest edge of the void. A series of checks then determined whether a sensor could be reached directly from P1 or whether it must first travel to point P2, on the other side of void, before continuing to the sensor. This resulted in a series involving two or three straight ray-paths, which combined to form the total distance used for calculating full travel time. Similar to Test Case 1, analytic, E3D and FMM travel times were computed and compared.

The third test case increased the complexity of Test Case 2 by including a heterogeneous velocity region that surrounds the rectangular void. This region was created using a distance dependent velocity gradient, created in the same manner as seismic fracture zones as discussed in Section *3.5.5.* Unfortunately in this case the medium was too complicated to realistically calculate an analytic travel time without using some numerical scheme and only involved the computation and comparison of travel times calculated by E3D and FMM.

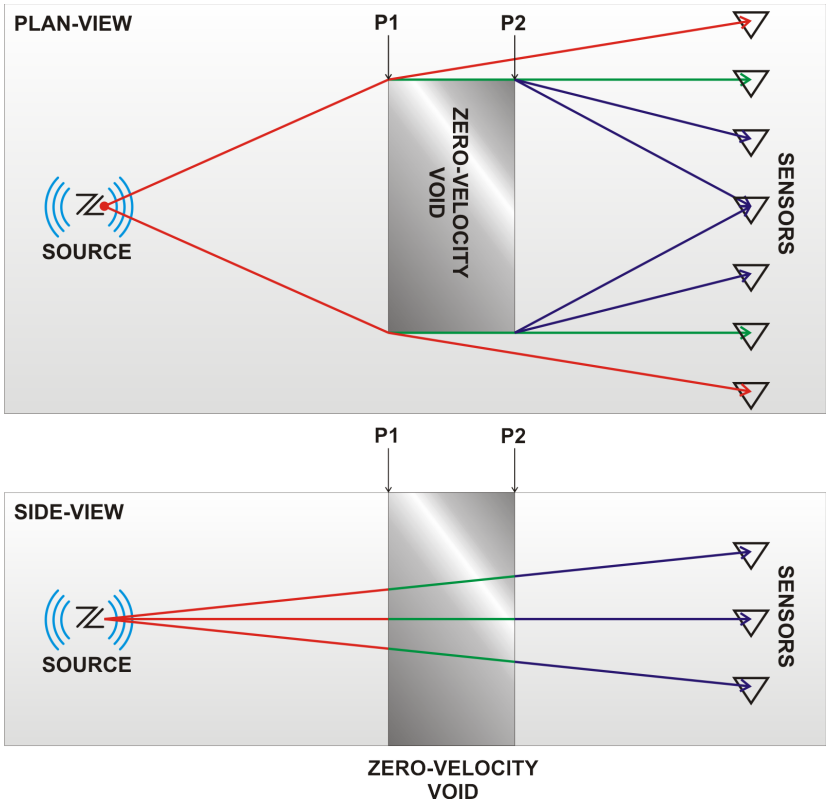

Figure 3.4: A diagram that illustrates the process where by signal travel times were analytically calculated for rays that were forced to bend around a rectangular zero velocity void (Test Case 2). The void extends from floor to ceiling so that rays were forced to bend around the sides. The signal path was calculated as a series of two or three straight rays involving the edges of the void, defined by points P1 and P2.

Synthetic waveforms generated by E3D for the different test cases can be found in Figure 3.5. Results of the three test cases can be found in the Appendix F.

3.4 Mining Front Estimation

The ultimate goal of the project was the evaluation of using low power seismic sources to provide a means of estimating the front advance of the sub-level mining process using source-to-sensor signal delay information. The front estimation process itself was a simple approach that made use of a pre-calculated look-up table of modelled travel times that were calculated for a set of possible mining steps that would result in ray-path bending.

A lookup table of this nature was made practical with the use of the FMM engine which could quickly calculate travel times, coupled with the ability to automatically generate any mining advance configuration. As discussed in Section 3.5.4 the voids created by the mining process was defined by blasting positions or rings which were predetermined by mine planners. Thus different mining stages were created by changing the sequence of ring advances made for each cross-cut.

In order to reduce the total number of model runs and look-up table entries, modelled configurations were limited to those that would cause a detectable phase delay (on the P-wave and S-wave first arrival). The limited coverage of the sensor array (Figure 3.8)

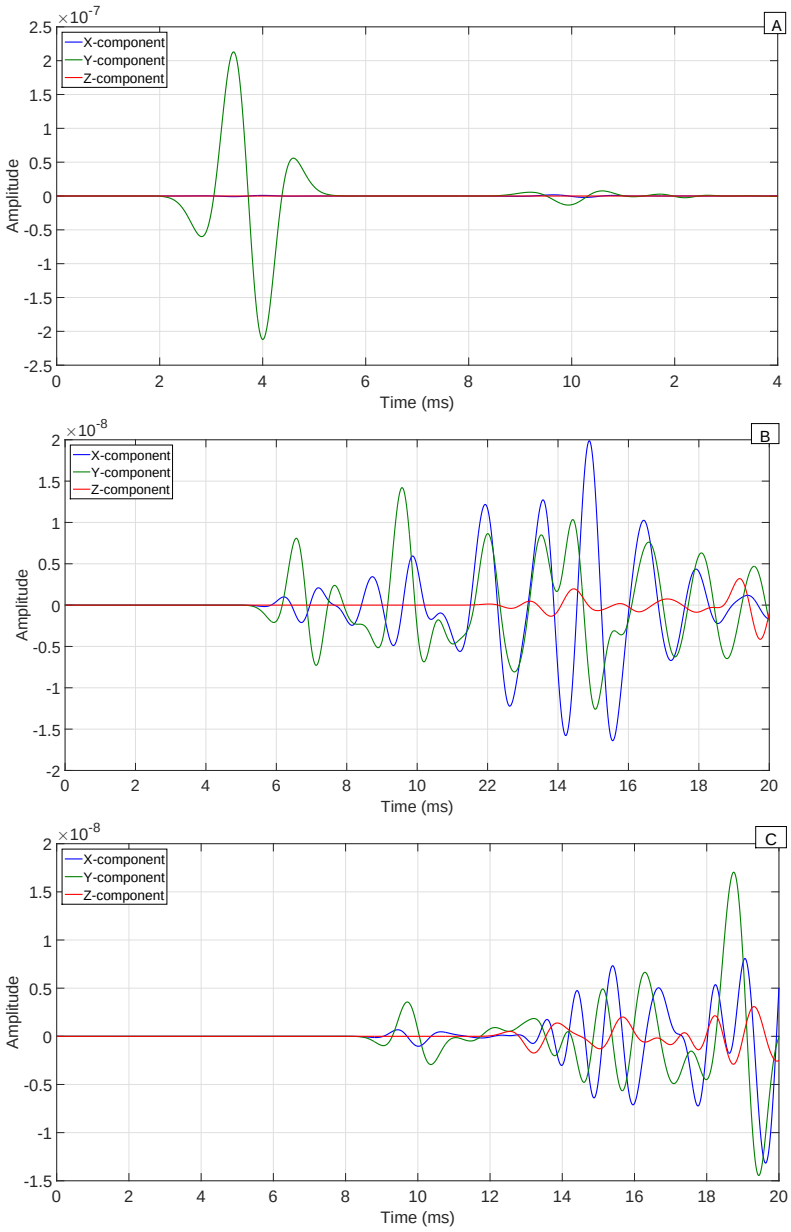

Figure 3.5: A set of E3D waveforms generated for the three FMM test cases performed using a point source with a Richer wavelet input function. A.) is the synthetic seismogram of the homogeneous test case, B.) the tests in the interaction of wave with a seismic void between the source and sensor, while C.) tests the additional of a distance dependent velocity gradient that surrounds the void. Both the source and sensor lie along the Y-axis.

reduces the area of concern to the latter halves of the last three cross-cuts on the level, namely Cross-cuts 6, 7 and 8.

With the full look up table computed, it was a simple matter to compare measured signal travel time changes, calculated using E3D modelling, to values in the FMM look-up table to find which stages were the closest matching. Front estimation was achieved by minimizing the cost function across all stages in the look-up table:

$$H(i) = \sum_{s=1}^{S} \left(\Phi_{s,i}^{FMM} - \Phi_{s}^{E3D}\right)^2 \tag{3.10}$$

Where:

- $\Phi_{s,i}$ is the signal travel time change for sensor s using modelled look-up step i. Model step $i = 1$ refers to the reference stage where no ray bending takes place.
- S the total number of sensors used in the model.

Any mining progression sequence could be modeled and the accuracy of the estimation process determined by comparing the calculated E3D travel time changes to those attained using FMM for the particular mining step.

The total error for each modelled step was calculated using the mean squared error (mse):

$$E_{mse} = \sqrt{\frac{1}{S}\sum_{i=1}^{S} \left(\Phi_{s,i}^{FMM} - \Phi_{s}^{E3D}\right)^2} \tag{3.11}$$

3.5 Model Construction

3.5.1 Model Grid

E3D and FMM made use of a modelling volume defined by a regular finite difference grid with assigned properties that best represent the properties of the physical experiment. The grid spacing size of the finite difference grid played an import role in the modelling process as it affected the model size in memory (which directly affected the computation time) as well as the accuracy of the geometry that could be modelled. More importantly, grid spacing was a parameter of the Courant-Friedrich-Lewy (CFL) condition which must be satisfied in order for the numerical solution of a differential equation (the wave equation in this case) to converge when using the method of finite differences [13, 49, 25]:

$$C = \frac{V\Delta t}{\Delta x} \leq 1 \tag{3.12}$$

Where:

- V is the medium velocity.
- Δt is the time step value.
- Δx is the grid spacing size.

Simply put the condition stipulates the maximum distance that the wave can travel in a single time step may not exceed the smallest point separation distance which is the grid spacing itself. If the grid spacing were to decrease while the wave velocity remains unchanged then the time step value must decrease in order to compensate. Exceeding the CFL condition will result in numerical errors and instability. It should be noted however that satisfying the CFL condition will not guarantee over all numerical stability.

Property	Model Parameters	Physical Experiment
P-wave Velocity (V_p)	5000 m.s^{-1}	5400 m.s^{-1}
S-wave Velocity (V_s)	3300 m.s^{-1}	3430 m.s^{-1}
Rock Density (ρ)	2800 kg.m^{-3}	2800 kg.m^{-3}
Rock Quality Factor (Q)	250	250
Sample Rate ($1/\Delta t$)	50 kHz	48 kHz

Table 3.1: A listing of the various modelling rock properties compared to their physical experiment equivalents

Model velocity was predetermined using the seismic velocities that best characterized the rock medium at Ridgeway Deeps Mine. This meant that only the grid spacing and time step values could be altered in order to satisfy the CFL condition. The total volume of the modelled experiment region was relatively small at $250 \times 250 \times 200$ m, however grid-spacing values smaller than 0.5 m were not practical to implement due to the model sizes exceeding available memory (16 GB). The time step size was made 2.0×10^{-5} s which made it comparable to the sampling rate of the physical experiment which was set at 48 kHz. The with these model parameters the CFL condition was satisfied with $C = 0.2$.

The default bulk medium properties used in the model are listed in Table 3.1 and compared to the values used by the mine.

3.5.2 Input Source

The piezoelectric source was represented in the model using a point based force time function that was created at the known physical position of the piezoelectric transducer. It was originally conceived that an appropriate source time function would be derived from the seismograms recorded by the close proximity reference sensor (RG1) at the Halo experiment site. However this seismogram proved to be significantly more complex than that of the driving signal of the piezoelectric source, but more importantly it was comprised of a predominantly high frequency spectrum.

A compromise was made by changing the source time function or driving wave to a simple Ricker wavelet, characterized by a central frequency of 2050 Hz. The Ricker wavelet was constructed using the equation [42]:

$$F(t) = \left(1 - 2\pi^2 f_0^2 t^2\right) e^{-\pi^2 f_0^2 t^2} \tag{3.13}$$

Where f_0 is the central frequency of the waveform and t, a short time series which was defined using Δt. The total number of time steps used for each model run ranged from 1500 to 2500 steps which was sufficient time to for the direct P- and S-wave fields to reach all sensors in the model.

The point source was located at the corresponding position of the piezoelectric source while output waveforms were attained from positions in the model which mirror the positions of the seismic sensors in the physical experiment (Figure 3.8 and Table 3.2).

3.5.3 Tunnel Voids

Ridgeway Deeps Mine's survey department provided an accurate 3D mesh CAD model of the 5235 and 5205 Levels, attained using laser scanning technology. This mesh model, comprised of irregularly sized triangles, demarcated the surface or skin of the tunnel area and so required a means of translation to the materials grid that was used in the

Sensor	X (m)	Y (m)	Z (m)
1	150.0	194.5	104.5
2	154.0	193.0	101.5
3	171.5	191.5	92.5
4	117.5	131.5	123.5
5	137.5	181.5	112.0
6	138.5	181.5	112.0
7	149.5	181.5	112.0
8	159.5	181.5	112.0
9	163.5	181.5	112.0
Source	**X (m)**	**Y (m)**	**Z (m)**
1	132.5	122.5	104.0

Table 3.2: Listing of source and sensor positions used in the numerical modelling of the Cave Front Tracking Experiment. Coordinates were attained from the locations of the source and sensors (Table 2.1) used in the physical experiment and offset to the local coordinates of the modelling grid.

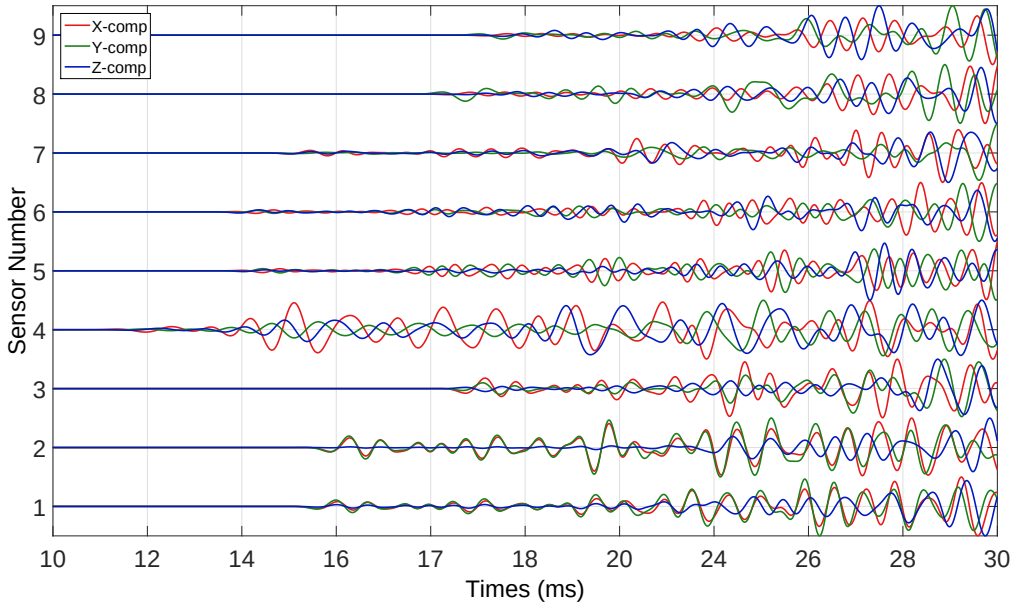

Figure 3.6: Synthetic seismograms created using E3D. Source time function was a Ricker-wavelet with a central frequency of 1000 Hz. The interaction of the wavefield with the tunnel and mined out front geometry results in significantly more complicated waveforms than that of the original source time function.

numerical modelling investigation. This was achieved using a two step process of mesh discretization and volume filling.

The mesh discretization process converted the CAD mesh surface to a surface in grid space. There are a number of methods available to discretize a mesh by interpolating the area of each triangle that makes up the mesh, however a simple approach was chosen which uses triangle geometry to increase the number of points in each triangle.

If the longest side of a mesh triangle was less than the grid spacing size then its three vertices would lie within the half grid spacing region to one or more adjacent grid points with no gaps in between. If the longest edge of the triangle was instead longer than the grid spacing then the triangle was subdivided into smaller triangles to the point where all smaller triangles had longest length sides that were shorter than the grid spacing. This ensured that taking all points on the triangle and transforming their coordinates to the grid space would not result in any gaps in the surface the points represent. The triangles were subdivided by making new vertices at the midpoint of each triangle side, a process which was repeated until the desired triangle size was achieved (Figure 3.7). The grid points closest to the vertices of the all the smaller triangles were then marked as surface points.

The discretization process only created the surface area representation of the tunnel model in the material grid instead of the actual 3D volume of tunnels. A 3D flood fill method was used to determine which of the grid points lay outside the discretized tunnel surface and marking the remaining points as being inside the tunnel. Flood fill is an iterative search method that determines the connectivity of points of the same property with respect to a given starting point in an ordered multidimensional array. Using the starting point, the algorithm checks if each neighboring point has the same assigned property as the starting point. If so, it is marked and the search moves to that point and begins searching its neighbors for property sameness. The process up until the point where no more neighboring points can be found that have the desired property. A well know two-dimensional implementation of this the Bucket Fill method in common paint programs. This method is typically implemented as a recursive algorithm which can be memory intensive, however non-recursive forms do exist. The program code for this mesh discretization process was coded by Jacques Gerber of the Institute of Mine Seismology.

Grid points marked as a part of the tunnel were assigned the properties of a seismic void (air) while points outside were assigned the properties of the host rock or bulk medium.

A true seismic void or volume filled with air cannot be correctly represented by a finite difference elastic modeling program which uses a regular grid without treating such points like the edges or boundaries of the grid. Finite element method is generally better suited to modeling transmission voids that are characterized by complex geometry such as mine tunnels but usually require a complex model setup process. These seismic voids in the both the E3D and FMM models were assigned elastic model properties that best represent a seismic volume that has little to no transmitted seismic energy while avoiding stark differences at void-to-rock interfaces that could result in numerical instability (Table 3.3). This meant that void grid points would technically still transmit seismic energy, however the large seismic impedance and extremely slow velocity ensured that transmitted energy was extremely low and almost all energy was instead reflected at the void and host rock interface.

3.5.4 Mined Out Front Advance

Sub-level mining uses an extraction or blasting design referred to as a drew-bell. A single draw-bell is created from a set of boreholes, drilled into the crosscut ceiling, forming a fan shape pattern which is referred to as a ring. The boreholes are charged with conventional

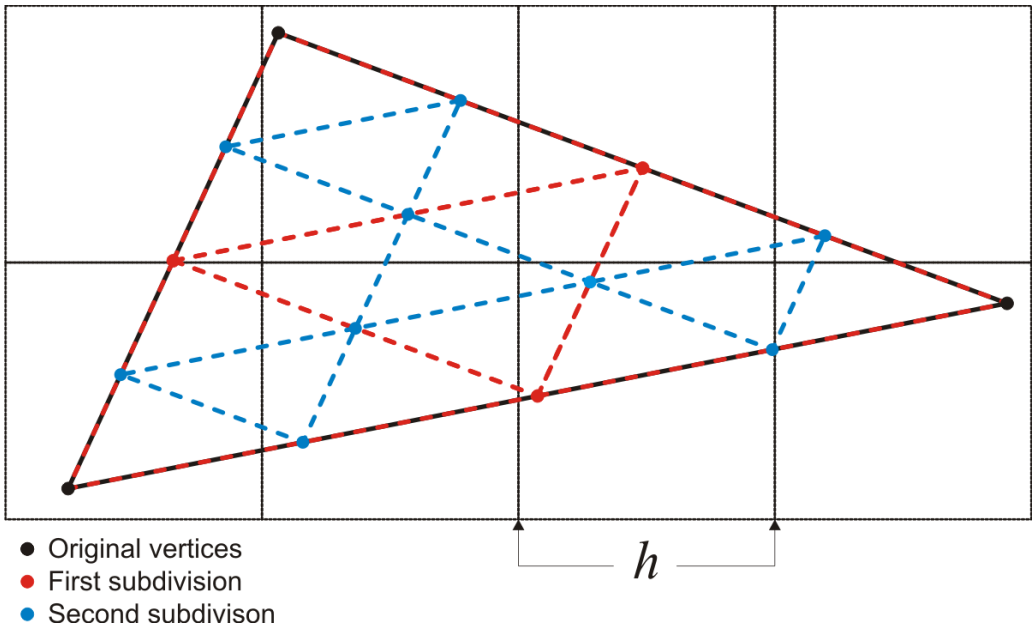

Figure 3.7: An illustration that describes the basic triangle interpolation method. If the longest edge of the triangle (black) is longer than the grid spacing h then the triangle is subdivided into smaller triangles (red) by creating new points at the midpoint of each triangle edge. The process is repeated until the longest edge of the subdivision triangles (blue) are smaller than h.

Property	Model Parameters
P-wave Velocity (V_p)	0.01 m.s^{-1}
S-wave Velocity (V_s)	0.0 m.s^{-1}
Rock Density (ρ)	1.0 kg.m^{-3}
Rock Quality Factor (Q)	0.01

Table 3.3: A listing of the medium properties used to model seismic voids.

explosives and denoted, creating a funnel shaped void of air and broken rock, effectively breaking up a slice of the crosscut ceiling. Sub-level mining progresses by sequentially drilling and detonating the uniformly spaced rings along the length of the mining crosscut.

Simulating the mining progression on the 5205 Level was achieved using information supplied by the mine concerning the shape and position of cross-cut rings. The approximate shape of the void generated by denoting a ring and resulting draw-bell was done using drilling pattern design information which was same pattern used for all rings drilled in the level. Void properties, based on a template drawbell, were then assigned to respective grid points at the position of a ring that was considered denoted. The full extend of the voids created by the mining advance was thus created by repeating the void assignment process for all rings considered denoted in the entire level for that particular mining step. Following the information of the historical ring blasting sequence conducted by the mine allowed the simulation of the actual sub-level mining process that occurred on the 5205 Level (Figure 3.11).

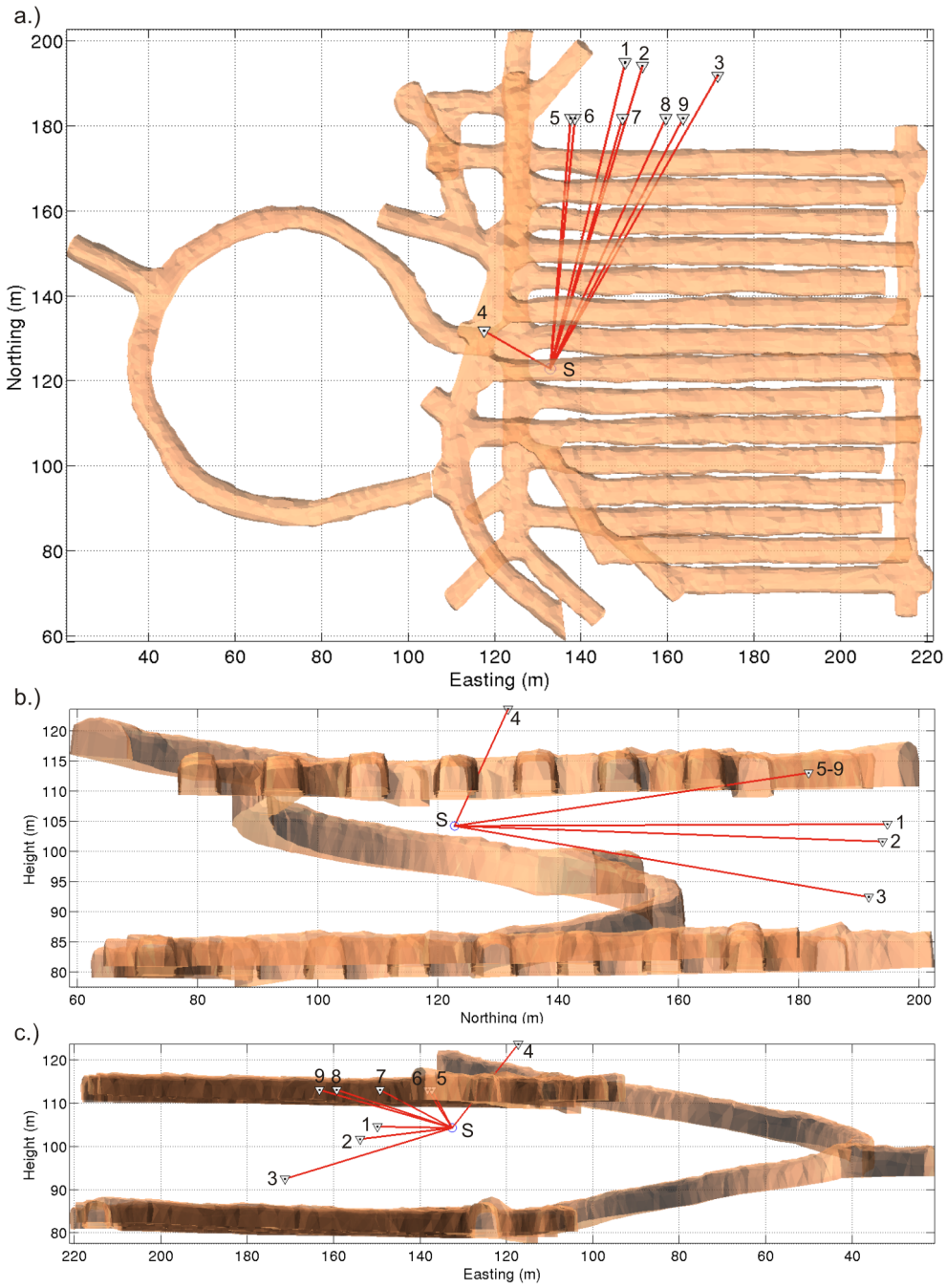

Figure 3.8: Top (a), East (b) and North (c) looking viewpoint plots of the 3D mesh model of tunnels that make up the Halo Cave Front Tracking Experiment Site. The 5205 level (lower level) was the level where the mining was performed, while the 5235 level (upper level) was already been mined out (not reflected in plot). Sensor positions 1-9, are represented by white triangles. Direct straight ray-paths from source position S, are demarcated by red lines. The 3D model data was supplied by the Geo-technical department of the Cadia Valley Operation, New Crest Mining Ltd.

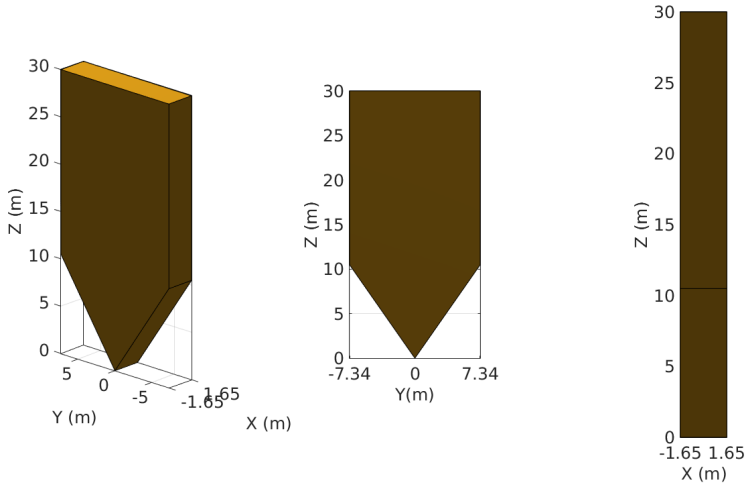

Figure 3.9: A 3D plot of the template shape used to generate the void region created by mining out a draw bell or a detonated ring. The shape and dimensions of the template were attained from drilling design information and ring spacing information acquired from the mine.

3.5.5 Fracture Zones

The process of mining (through the use of explosives) creates a fracture zone in the rock surrounding the excavated medium which impedes the seismic transmission [10]. These fracture zones were represented in the model by implementing a distance dependent velocity (both P- and S-wave) for all grid points that lay within a certain distance of a void grid point. A linear distance dependence was used, starting at a minimum of 10 % of the bulk medium velocity at the void interface and increasing linearly up to the original bulk velocity over a radial distance of 10 m [33].

This fracture zone was implemented in the model by searching for all grid points that lay on the surface of a void volume, which was achieved by checking whether each void point in the full model had a neighboring grid point which was not a void point. For every point found to lie on the surface of the void volumes, all non-void grid points that lay within the fracture zone radius were found and their seismic velocities were reduced based on their distance from the considered surface point. When considering points which already had their velocities altered due to a neighboring void point, the lowest of the possible assigned values was chosen as the new velocity value.

The fracture zone was calculated using the complex geometry of both the mine tunnels and the sub-level mining of blasted rings which meant all void geometry was fully surrounded by a fracture zone represented by a velocity gradient.

3.5.6 Absorbing Boundary Layers

Finite difference models that only represent a small section of a much larger medium are subject to the problem of reflections that are generated once a wave field reaches the boundaries of the grid. The boundary was a free surface which caused perfect reflections that radiated back towards the interior and cause significant interference with the original wave field. This problem could be handled by extending the limits of the grid and reducing the number of time steps such that the boundary reflections were not given enough time

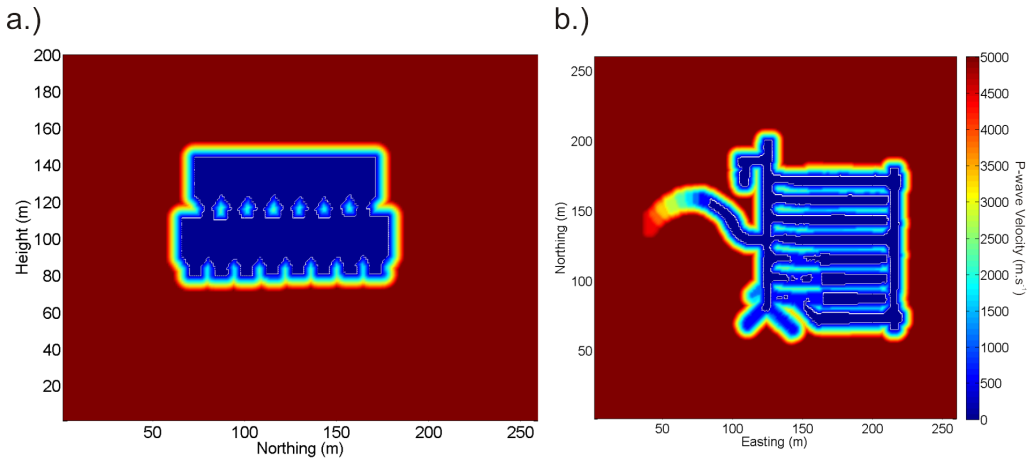

Figure 3.10: A heat-map plot of a 2D section of the input velocity model showing tunnels as zero-velocity seismic voids (blue), surrounded by a fracture zone (light blue to orange) which was approximated by a distance dependent velocity gradient from the void surface. This provided a linear transition between the void geometry and the bulk medium. Plot a.) is an East looking cross-section through the mining region, showing the draw bell shape for each cross-cut. Plot b.) shows a plan view cross-section of the 5205 level.

to reach a particular point of interest.

When such an approach was not possible then a series of absorbing boundary layers must be included in the input model to attenuate and absorb the waves that reach the boundary and greatly reduce the amount of energy reflected back. This was achieved by generating a set number of concentric layers that lined up against the grid boundaries and who's seismic velocity and Q values gradually decreased the closer the layer was to the actual boundary. This resulted in a zone which attenuated and retarded the wave approaching the boundary resulting in significantly reduced and delayed reflections.

Such absorbing boundary layers were not entirely perfect as E3D unfortunately does not include a means of directly attenuating a wave. Instead a balance was struck between including absorbing boundary layers and reducing the number of time steps to the point that prevented the small reflections from reaching the sensors.

3.5.7 Noise

SNR was an important consideration for this experiment owing to the use of a weak seismic source and the necessity to stack large volumes of data to recover its signal as well as the role SNR plays in the minimum temporal resolution that could be achieved. The SNR attained by the physical experiment was largely controlled by changing the amount of data stacking used to create each stack. However the synthetic waveforms calculated using E3D are noiseless and lack the random influences inherent in all physical recordings. From the Cramér–Rao lower bound (Equation 2.2), it was determined that an SNR of less than 1 was required in order to measure a travel time change of 1 %. However a signal with an SNR of less than 1 is not useful in a time domain based cross-correlation and instead an empirical minimum threshold should be established.

In order to investigate the experimental sensitivity to noise in relation to its ability to estimate mining advance, artificial noise was added to E3D synthetic seismograms. To simulate the effect of signal noise, white Gaussian noise (WGN) was first generated and then added to the E3D waveforms. A vector of white Gaussian noise was generated using

a normalized random number generator. Different SNR values were attained by simpling scaling the amplitude of the noise added to the seismograms.

3.5.8 Modeling Procedure

Tunnel voids, mined out volumes, fracture zones and absorbing boundary layers were all part of the geometry construction for each modelling run.

The layout of the source and sensor positions relative to the mining region meant that the mined out front would only intersect with ray-paths between source and sensors at a late stage of the mining process. In order to study the effect of ray bending the mined out front was advanced to a point just before it intersected with the closest ray-path which was formed by Sensor 3.

A model run was performed for each consecutive ring advancement in Crosscuts 6, 7 and 8 starting from rings 19, 18 and 19 respectively. Each consecutive modelling step therefore differed from the previous step by a single ring advance from one of the three cross-cuts. Synthetic seismograms from all sensors positions, for all modeled mining steps, were fed into phase-lag calculation programs which measured the increase in phase lag between two consecutive steps (due the dynamic reference scheme) caused by increase ray-path length and compared to the travel time change calculated using FMM.

In a similar fashion to the tests cases performed to test the accuracy of the FMM engine, mining front advance was investigated by starting with the simplest case of advancing a single cross-cut. This test was performed individually for Cross-cuts 6, 7 and 8 and the respective changes in phase-lag compared with the FMM travel time changes.

The second investigation was aimed at replicating the expected sub-level mining procedure of Crosscuts 6, 7 and 8 in order to build an understanding of how the process would affect the source signal. The mine did not follow a strict blasting sequence (blasting normal followed the rate at which draw-bells could be effectively excavated) for the different crosscuts. The mining of the 5205 Level had ceased before intersecting with the region by the experiment array which meant that no specific blasting schedule for the final set of rings was received.

Instead a sequential ring advance pattern was used, where by each individual crosscut would advance by one ring, starting with Crosscut 6, then 7 and lastly 8 and repeating until the end of the three crosscuts had been reached. For each ring advance, the model was run in E3D and the FMM engine. The phase-lags for each step were calculated and compared to FMM travel time changes and front advance estimated. Full travel time delay increase with respect to the first modelled step was calculated by summing the delays of all previous modelled steps.

In order to study the effect of noise and the required SNR values for correct front estimation, fixed level WGN was added to all synthetic seismograms and the process of phase-lag calculation and front estimation repeated until a minimum SNR value was established.

3.6 Modelling Results

3.6.1 Known Advance Look-up front estimation

The first modelling case was designed to test the signal delay measurement and void estimation accuracy of an advancing crosscut using an travel time change look-up table for an expected known front advance. Crosscuts 8 was modelled individually using a single ring advance per modelling step. The second modelled mining investigated the sequential advance of Crosscuts 6, 7 and 8, which bore a closer resemblance to how the sub-level mining would typically progress and referred to as the normal mining sequence.

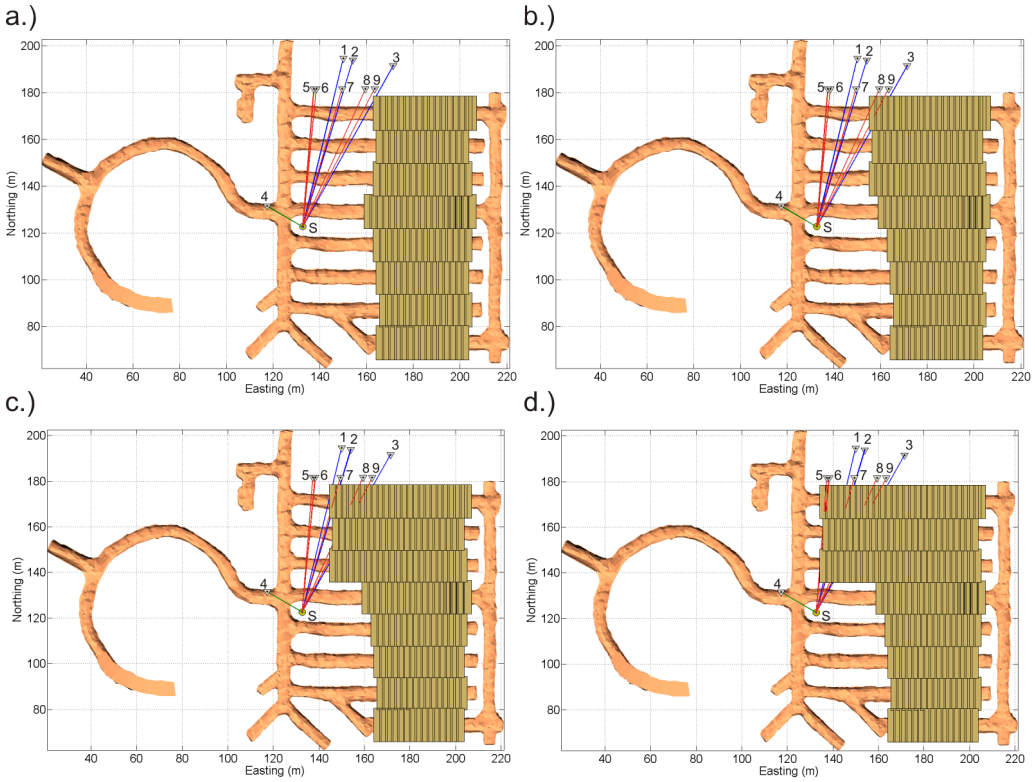

Figure 3.11: A series of 3D model plots of the simulated mining of Halo 5205 Level that intersected with sensor ray-paths. The denoted rings are represented by gold rectangles and collectively they make up the mined out region. Plot a.) shows the modelling step 6 and the final state of the cave once mining in the region had ceased. Plots b.), and c.) show intermediate modelling steps 18 and 30 respectively while d.) plots the final step 40. Direct straight ray-paths from source to sensors are plotted to show points of ray-path intersection with the mining front, for the various modelling steps.

Travel time delays were measured from E3D synthetic seismograms using cross-correlation of the initial portion of the P-wave, while P-wave travel time changes were also calculated using FMM for all modelling steps and travel delay look-up tables created. The cave front advance was then inverted for using the minimization method discussed in Section 3.4. A plotted comparison of signal delay increase calculated using FMM and E3D methods for both modelling cases can be found in Figures 3.15 and 3.16 respectively. An example of the cost function behavior for the single cross-cut modelling case can be found in Figure (3.14).

The front estimation for both modelling investigations, using a known look-up table detected the correct extent of the voids once they had advanced to the point of interaction with signal ray-paths. The results of the front estimation are listed in Tables 3.4 and 3.5.

Phase delay results from both modelling cases show a measured response from the first draw bell advance of Crosscut 8 (draw bell 18 to 19) which reveals the ray-path sensitivity to the fracture zone which was generated ahead of the void. Path interaction from Crosscuts 7, and 6 advance only happened later in the modelled mining sequence owing to the ray-path configuration with respect to those crosscuts.

In the second modelling case, a comparison of the phase-lags measured using E3D

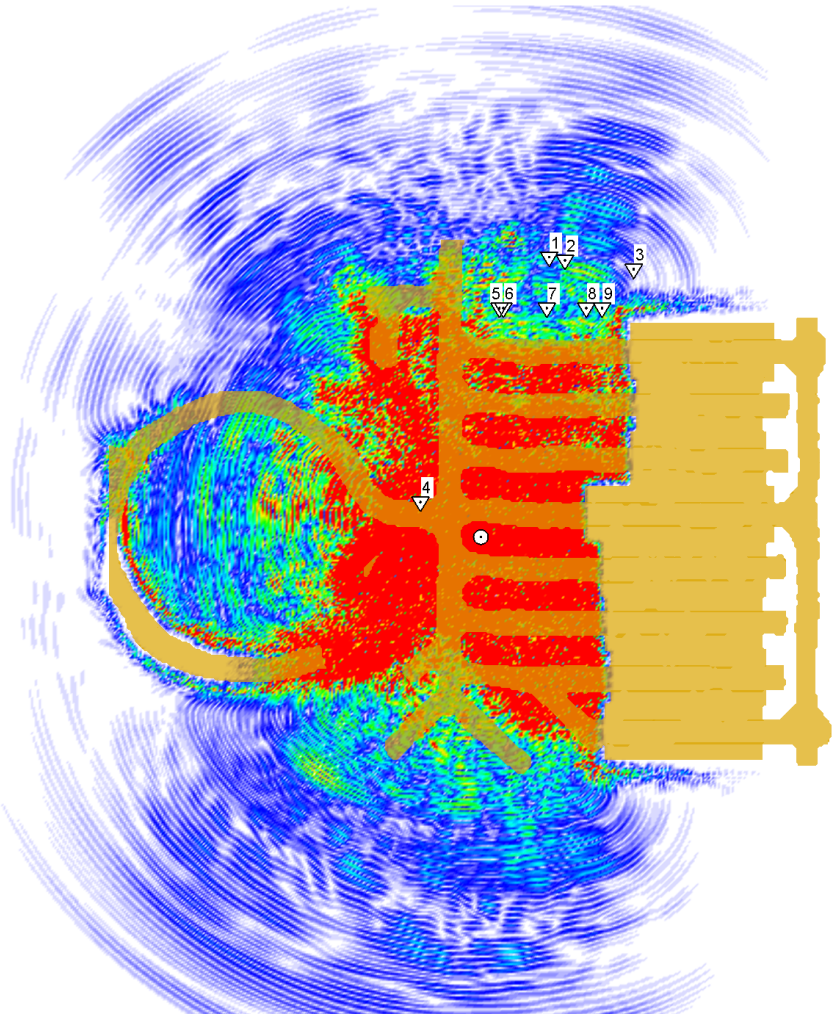

Figure 3.12: A plot of the modeled wavefield generated by E3D along the XY plane, passing through the position of the source. Source time function was a Ricker wavelet with a central frequency of 1000 Hz. Wave bending can be seen along the fracture zone regions which surround the seismic voids that define the mined out front and tunnels. An iso-surface of the discretized tunnel and mined out region is represented by light yellow regions.

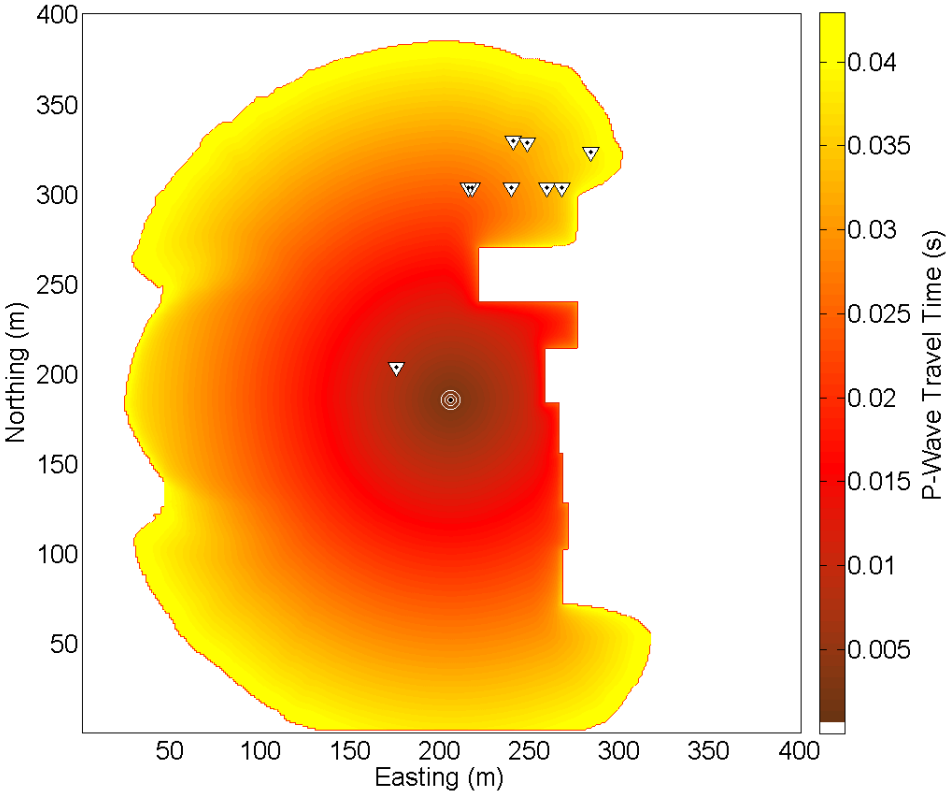

Figure 3.13: A heat map plot of the travel time calculated using the FMM engine taken in the XY plane passing through the position of the source. The source position is denoted by concentric white rings, while sensor positions are represented by white triangles. This FMM solution was attained after 6×10^6 evaluation steps with a model grid spacing of 0.5 m. The presence of the fracture zone caused bending and retardation near all void volumes.

synthetic seismograms to the respective values in the FMM lookup-table (Figure 3.15) revealed noticeable offsets, in particular for sensors 7, 8 and 9. The low correlation values attained for these sensors were attributed to the weak P-wave signal which was a result of the sensors positioning within the seismic shadow cast by the long wall of crosscut 8 on the 5235 level. Whilst not below the cross-correlation value disregard threshold, the phase delay measurement errors accumulated, which resulted in slight deviations from the expected phase as attained from FMM calculations. The total phase-lag curve was subsequently offset for following measurements with respect to the FMM values. However these differences, while larger than the expected errors, were sufficiently small enough as not to derail the front estimation process.

Sensor 4, which was located far from the mining volume showed no phase delay increase as expected.

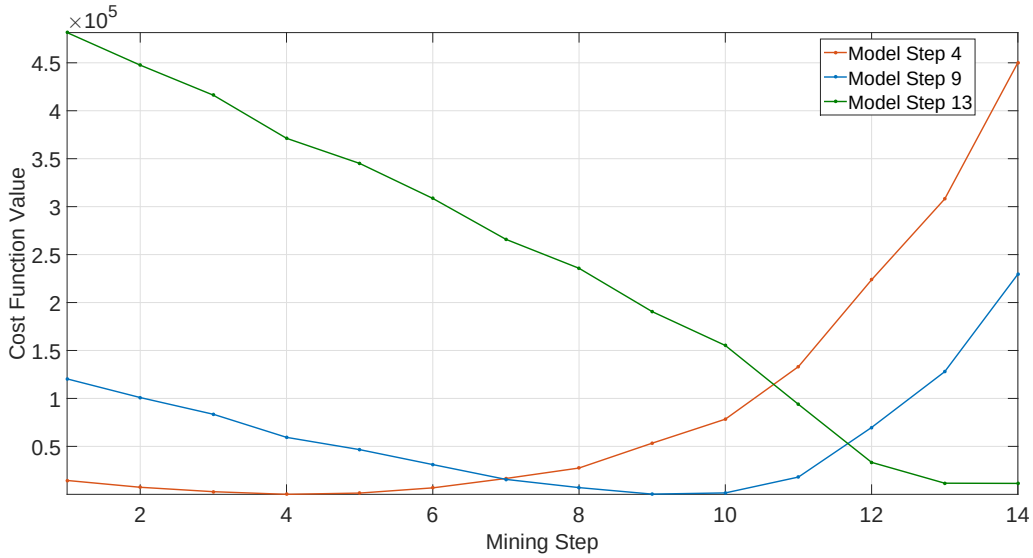

Figure 3.14: The mining step estimation cost functions for the modelling investigation of Cross-cut 8. Only model runs 4, 9 and 13 are shown for viewing purposes.

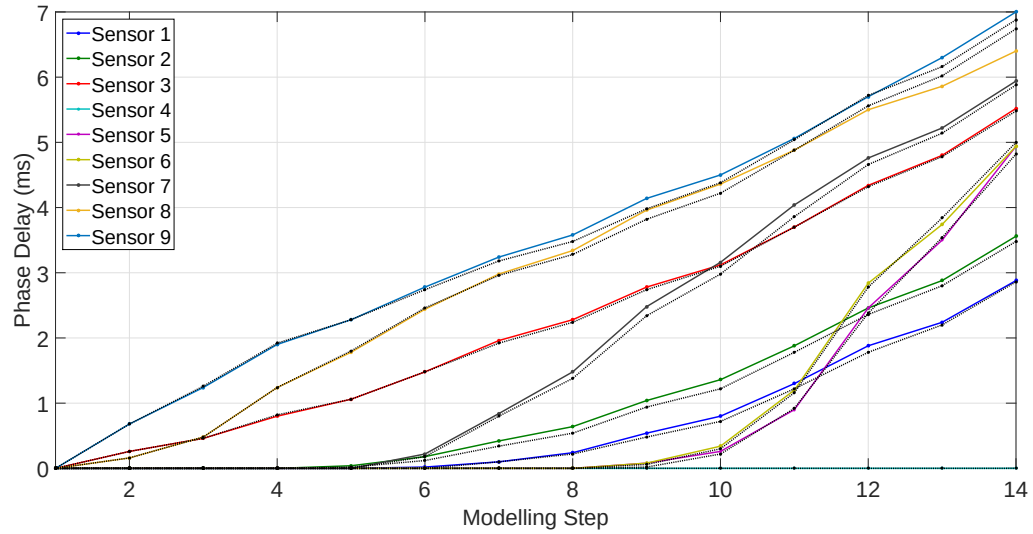

Figure 3.15: The phase-delay measured using E3D (coloured plot) compared to time differences calculated using FMM (black dotted lines) for the first modelling investigation of the mining advance of Cross-cut 8. Sensors 2, 7 and 8 exhibited the largest differences in phase lag despite high cross-correlation values (> 0.9). Measured phase lag error for all sensors was much smaller than the phase-lag change between modelled steps.

	Mined out Front Advance		
Model Run	Actual	Calculated	Mean Error (ms)
Crosscut	8	8	-
1	18	18	0.0
2	19	19	0.0
3	20	20	0.0
4	21	21	0.0
5	22	22	0.0
6	23	23	-0.02
7	24	24	-0.03
8	25	25	-0.05
9	26	26	-0.08
10	27	27	-0.08
11	28	28	-0.04
12	29	29	-0.04
13	30	30	-0.01
14	31	31	0.00

Table 3.4: Estimation results calculated for the modelled front advance of the single crosscut 8. The mined out front was correctly estimated for the whole sequence in this test case .

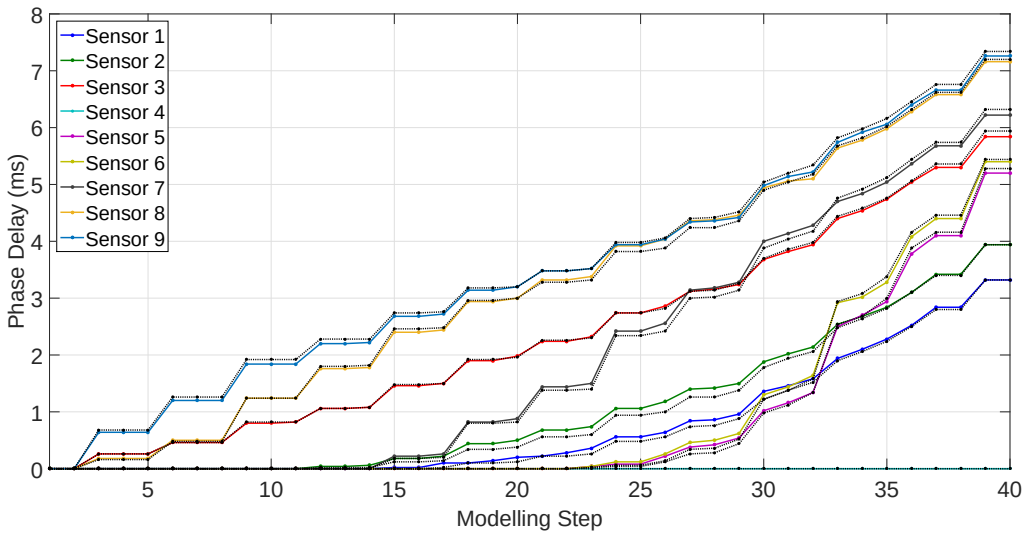

Figure 3.16: The phase-delay measured using E3D (coloured plot) compared to time differences calculated using FMM (black dotted lines) for the second modelling investigation of the sequential mining advance of Crosscuts 6, 7 and 8. Sensors 1, 2, and 7 exhibited the largest differences in phase lag despite high cross-correlation values (> 0.9). Early ring advances in Crosscuts 6 and 7 could not be resolved by the source and sensor array configuration due to the geometry of the array and so yielded little to no signal delay change for both E3D and FMM solutions.

	Mined out Front Advance						
Model Run	Actual			Calculated			E_{mse} (ms)
Crosscut	6	7	8	6	7	8	-
1	19	18	19	19	18	19	0.00
2	19	19	19	19	18	19	0.00
3	19	19	20	19	19	20	0.01
4	20	19	20	19	19	20	0.01
5	20	20	20	19	19	20	0.01
6	20	20	21	20	21	21	0.01
7	21	20	21	20	21	21	0.01
8	21	21	21	20	21	21	0.01
9	21	21	22	21	21	22	0.03
10	22	21	22	21	21	22	0.03
11	22	22	22	21	21	22	0.03
12	22	22	23	22	22	23	0.03
13	23	22	23	22	22	23	0.03
14	23	23	23	22	22	23	0.01
15	23	23	24	23	23	24	0.01
16	24	23	24	23	23	24	0.01
17	24	24	24	24	24	24	0.05
18	24	24	25	24	24	25	0.01
19	25	24	25	24	24	25	0.03
20	25	25	25	25	25	25	0.09
21	25	25	26	26	26	26	0.02
22	26	25	26	26	26	26	0.00
23	26	26	26	26	26	26	0.15
24	26	26	27	27	27	27	0.05
25	27	26	27	27	27	27	0.05
26	27	27	27	27	27	27	0.27
27	27	27	28	27	27	28	0.15
28	28	27	28	28	27	28	0.07
29	28	28	28	28	28	28	0.17
30	28	28	29	28	28	29	0.15
31	29	28	29	29	28	29	0.09
32	29	29	29	29	29	29	0.02
33	29	29	30	29	29	30	0.06
34	30	29	30	30	29	30	0.06
35	30	30	30	30	30	30	0.11
36	30	30	31	30	30	31	0.12
37	31	30	31	31	30	31	0.11
38	31	31	31	31	31	31	0.11
39	31	31	32	31	31	32	0.15
40	32	31	32	32	31	32	0.15

Table 3.5: A comparison of mining advance estimation results calculated for the sequential mining front advance of Crosscuts 6, 7 and 8. Phase-lags calculated using E3D waveforms compared well with FMM times (Figure 3.16) however the advance of Crosscuts 6 and 7 could only be distinguished after model step 27 when both Crosscuts intercepted with all sensor ray-paths.

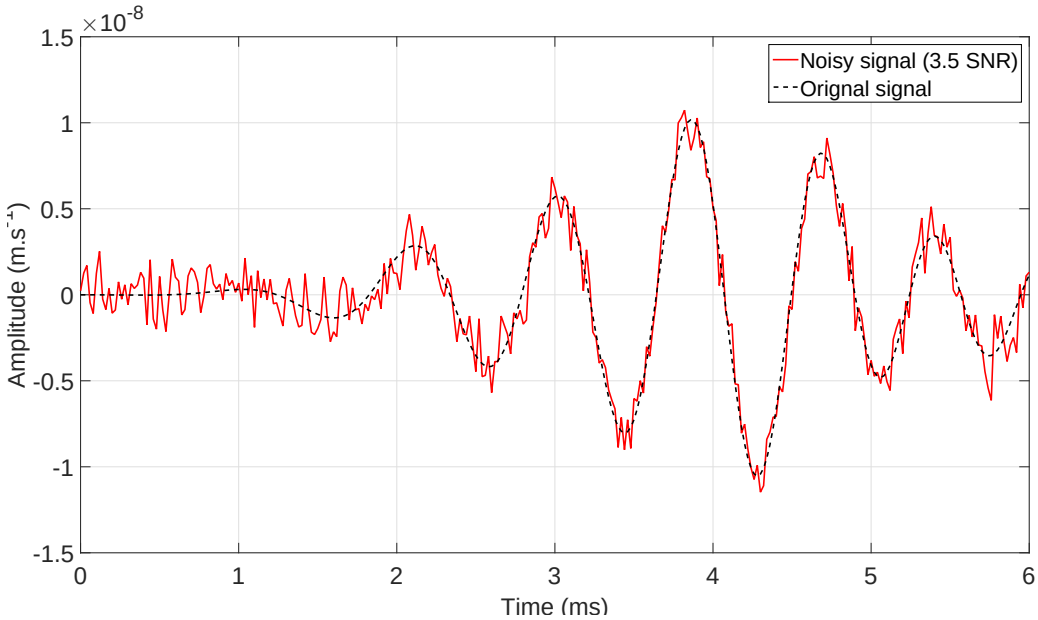

Figure 3.17: An example of a waveform with a signal-to-noise ratio of 3.5. This ratio was sufficient for cross-correlation purposes and measuring the phase-lag with sufficient accuracy as to attain a similar front estimation results as attained using noiseless signals.

3.6.2 Noise Investigation

Two different investigations concerning the effect of signal noise were conducted using synthetic seismograms generated using E3D. The first test was performed to establish the what was the minimum SNR required to measure large signal delay changes (1 % or larger) with sufficient accuracy as to attain the same mining advance estimation results as was attained in the investigation were no signal noise was present (Section 3.6.1). White Gaussian noise was added to the synthetic seismograms attained from the normal mining sequence. Signal delay changes and mining front estimation calculations were performed using noise contaminated synthetic seismograms characterized with a starting SNR of 20 and decreasing to a value of 1.5.

From this test it was concluded that a minimum SNR of 3.5 (Figure 3.17) was tenable for mining advance estimation. Signal delays could be measured using SNR values as low as 2 but the associated errors hampered the accuracy of the mining front estimation.

The second noise test investigated the simulated change in SNR as the modelled mining progressed. This was done by adding fixed level WGN to synthetic seismograms which was scaled to ensure all sensors start off at the same SNR. This test replicates the behavior expected in the physical experiment where recorded noise levels are approximately constant (in the long term) and recorded signal amplitude would decrease as the mining progressed due to increased path length and ray-path bending.

Results from this investigation show a over all decrease in modelled signal amplitude which was much larger than expected considering the total path length increase (Figure 3.18). These results are discussed further in Chapter 5.

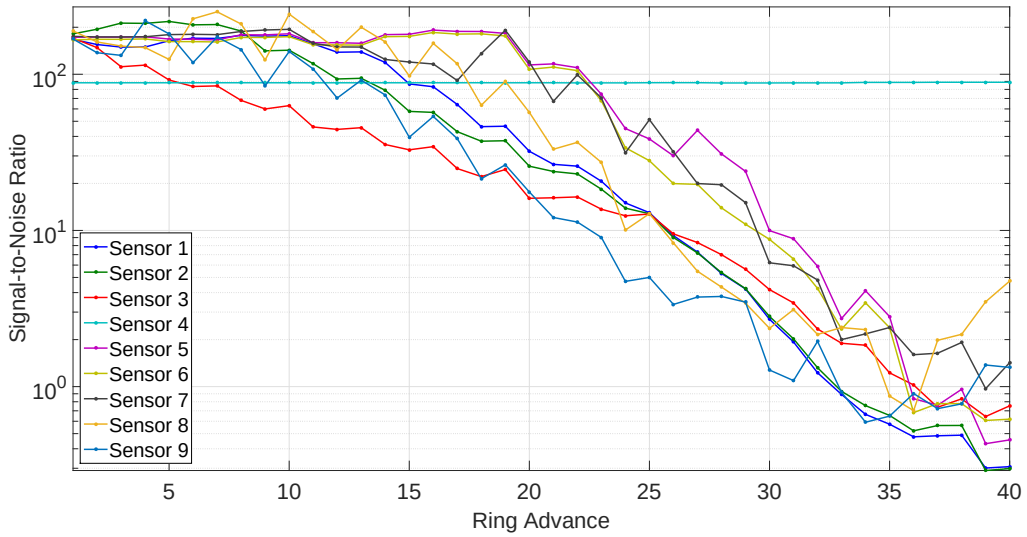

Figure 3.18: Signal-to-noise ratios measured from seismograms generated using E3D with fixed level white Gaussian noise added. SNR decreases rapidly for all sensors over the modelled mining sequence due to the effect of increased travel distance, decreasing medium transmission quality and low diffracted wave energy.

Chapter 4

Physical Data

4.1 Data Recording

The first seismic data recordings taken from the reference sensor verified the signal output generated by the piezoelectric source however the direct signal recorded by the array sensors was particularly weak and could not be distinguished from the ambient noise. Signal recovery from all recording channels was only possible after significant data stacking which was achieved using the stacking methods discussed in Section 2.5.2.

The signal recorded from the reference sensor was used to create the reference waveform for both the signal identification (Section 2.5.4) and pre-stack phase alignment processes (Section 2.5.2). Recording data spanned a period of a year and a half, with the first seismic data recorded on the 20$^{\text{th}}$ of November 2012 and finally halted on the 30$^{\text{th}}$ of June 2014. Significant alterations in the experimental recording hardware required that the data be divided into four separate sets which were then treated independently. The parameters of the pre-stacking were also altered slightly between sets.

The first pre-stack data recordings of Set 1 began on the 28$^{\text{th}}$ November 2012 and proceeded up to the 4$^{\text{th}}$ April 2013 (Figure 4.1). Data recording was terminated when damage was sustained to the fibre optic cable responsible for carrying timing communications to the piezoelectric source driver. The piezoelectric source driver was originally programmed to only operate the source when it was receiving stable PPS time updates. This was a legacy feature originally included for the purpose of unaided vertical pre-stacking around which Phase One of the experiment was designed.

Recording for Set 2 started on the 6$^{\text{th}}$ June 2013 after repairs to the fibre optic cable were completed, as well as a modification to the data acquisition software which was implemented to help improve data recording consistency (Figure 4.2). Set 2 recording was halted on 4$^{\text{th}}$ October 2013 following a malfunction of the piezoelectric source driver which resulted in significantly reduce power output. The driver was replaced with an upgraded unit and recording for Set 3 began on the 2$^{\text{nd}}$ November 2013 where it continued up until the 11$^{\text{th}}$ of March 2014 (Figure 4.3). It was terminated a month after mining in the area had ceased. Unfortunately the mine had halted extraction on the level due to the falling ore grades which made mining in the 5205 Level uneconomical, sequentially stopping ring blasting just before the first expected point of ray-path intersection.

The pneumatic source was also operated during this period of Data Set 3, with the first routine shot recorded on the 1$^{\text{st}}$ November 2013 and continued to operate until it suffered from mechanical failure on the 23$^{\text{rd}}$ March 2014 (Figure 4.4). Recording of stacked data was once again resumed several weeks later on the 1$^{\text{st}}$ of May for the purpose of monitoring the medium after mining had concluded. No hardware changes were made, however pre-stacking parameters were sufficiently altered to consider the data as part of a new set, namely Set 4.

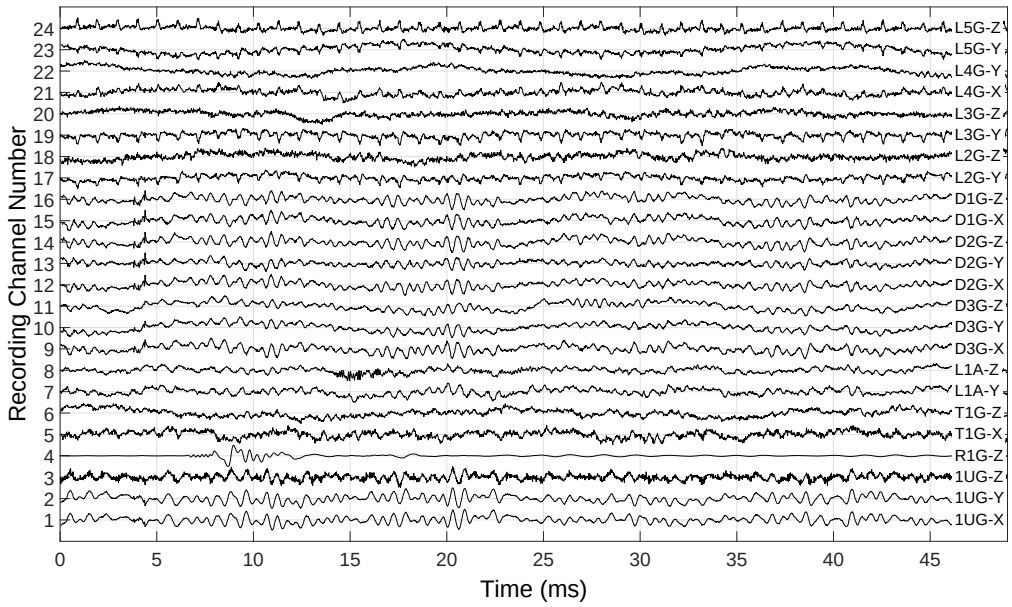

Figure 4.1: A example stacked seismogram from data Set 1, comprising of five minute's worth of pre-stacked seismograms recorded at midnight on the 28th of November 2012. Each trace was labeled by the respective sensor name and axial component on the right edge of figure. All traces were individually normalized for viewing purposes. Coherent waveforms are clearly visible in trace which appeared to be unique to the individual netADC8 digitizers.

Apart from the experiment down times listed above, there were times within each data set when no recording took place, resulting in small gaps within the data. Temporary loss of power or timing communications and hard disks reaching capacity were the main causes for such periods of data loss.

4.2 Reference Sensor Signal

The signal recorded by the reference sensor was particularly important for the success of the experiment as it was required not only for signal identification but also for pre-stacking purposes. The close proximity of the sensor to the piezoelectric source ensured that the recorded signal had a very high SNR, which was necessary for signal identification using the threshold method (Section 2.5.4).

Signal cross-talk (which might occur between adjacent conductor pairs in a cable or between the circuit tracks of the analogue-to-digital converter electronics) is typically a very weak form of noise, however past experiments showed that extensive data stacking could recover the cross-talk generated by strong signals, which becomes a problem when attempting to recover particularly weak seismic signals. The high frequency of the source signal and its coherence with stacking windows, meant that cross-talk could dominate over weaker seismic signals and it is often difficult to distinguish whether a stacked signal is seismic or cross-talk related. In order to reduce the effect of cross-talk from the reference sensor(s), a signal attenuator was included in the form of a resistive divider with a 1:100 attenuation ratio.

The changes made to the seismic source hardware during the course of the experiment resulted in changes to both the power output and waveform pattern generated by the

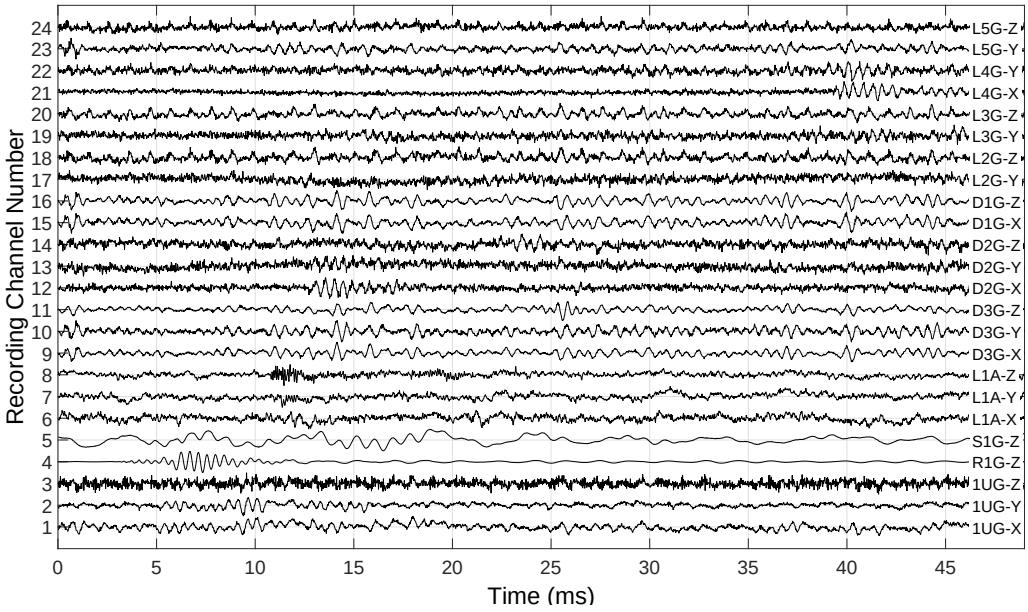

Figure 4.2: An example of a stacked seismogram from data Set 2, comprising of one minute's worth of pre-stacked seismograms recorded at midnight on the 25th of June 2013. Each trace was labeled by the respective sensor name and axial component on the right edge of figure. All traces were individually normalized for viewing purposes. Sensor T1G was replaced with a close proximity surface mount sensor, S1G in the hopes that it could provide short range velocity measurements.

source (Figure 4.5). Despite these changes, two significant problems with the piezoelectric source were identified which were not fully resolved before the experiment had to be terminated.

The first significant problem was a mismatch between the frequency of the signal generated by the source driver and the resonant frequency of the source itself. Analysis of the spectral energy content of the signal recorded by the reference sensor revealed that the signal was dominated by a distribution of frequencies centered at 2350 Hz (Figure 4.6), as opposed to the intended 2050 Hz required to operate the source at its second resonant mode (Section 2.4.1). From the frequency response test data (Figure 2.5) it was estimated that this resulted in a 50 % drop in recorded amplitude. A minor spectral distribution was also observed at the 1560 Hz resonant mode. The cause of the problem was traced back to a programming error of the control electronics responsible for generating the driving waveform which was inherited by all source drivers used during the experiment. Unfortunately this was only discovered after the experiment had concluded, when an investigation was conducted to determine the cause of the problem as well improve the existing signal amplification circuitry ([20]).

The second problem encountered was the gradual and subtle change in the overall signal recorded by the reference sensor. This problem was not fully recognized until well into the recording of data Set 1 and its exact cause was not understood. Tests were performed while the experiment was operational in order to identify the possible cause by a process of elimination. These tests ruled out the data acquisition software, the source driver and reference sensor which left two possible causes; the piezoelectric source itself was changing slowly over time or that the conditions in the source borehole were changing. It was possible that the piezoelectric material in the source deteriorates over time after

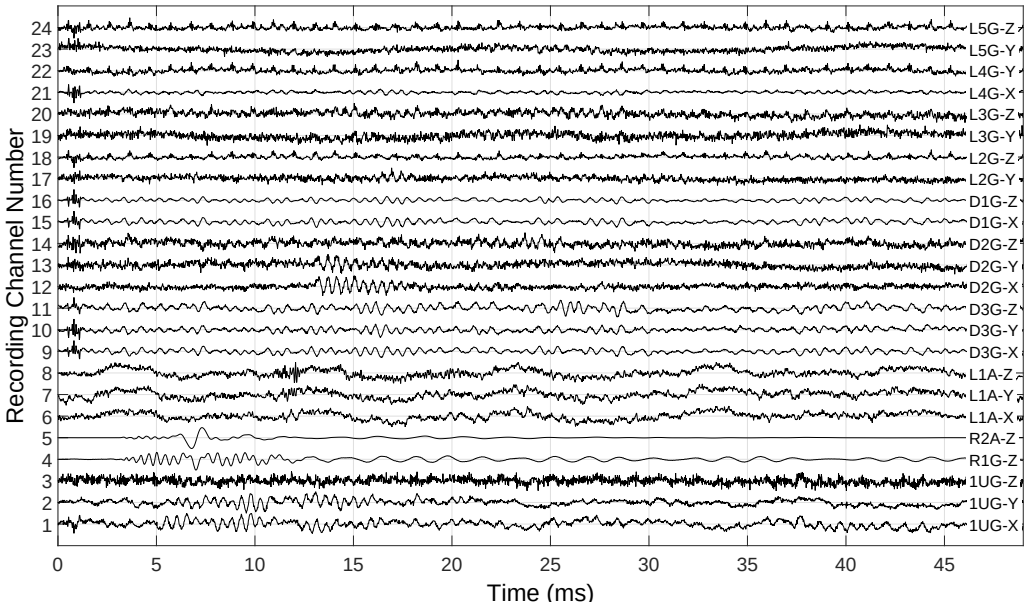

Figure 4.3: An example of a stacked seismogram plot from recording Set 3, comprising of one minute's worth of pre-stacked seismograms recorded at midnight on the 1st of November 2013. Each trace was labeled by the respective sensor name and axial component on the right edge of figure. All traces were individually normalized for viewing purposes. Sensor R2A-Z was installed to replace S1G following observed variations in the reference signal from R1G-Z.

extended use when operated at high power and in a non-resonant mode.

The other possibility was a steady drop of the water level in the source borehole due to evaporation or leakage which may have occurred because of imperfect seals on the borehole cap. Water levels were not strictly monitored, however a basic lab test was conducted which investigated the effect of slowly dropping the water level in a column, while the piezoelectric source was operated. This test showed that the coda portion of the wave does experience a change in phase as the reflection distance between the surface of the water and the sensor slowly decreases.

The effect of this gradual change in the reference waveform manifested as a very large overall drift in signal phase delay measured by all recording sensors (Figure 4.7), as all recording channels were slaved to the phase alignment of the reference signal. This drift in the reference signal timing was not originally anticipated and the full extent of the problem was only revealed after an investigation was conducted to try and correct for this larger than expected deviation that was recorded by all the sensors.

The first step taken was the installation of an water based accelerometer sensor at the start of recording Set 3 which served as the both the replacement reference sensor as well as acting as a comparison to the original reference for measuring long term phase lag drift. This secondary reference sensor confirmed that gradual source signal change was occurring over time, however it did not alleviate the large overall drift observed from all sensors (4.8). What was instead required was a direct measurement of the signal generated by the piezoelectric source driver. No provision had originally been made for such a measurement, however, the electromagnetic radiation generated by the high voltage driving signal caused interference on the cables linking the sensors to the data acquisition units. This interference, like the piezoelectric seismic signal cross-talk, was extremely

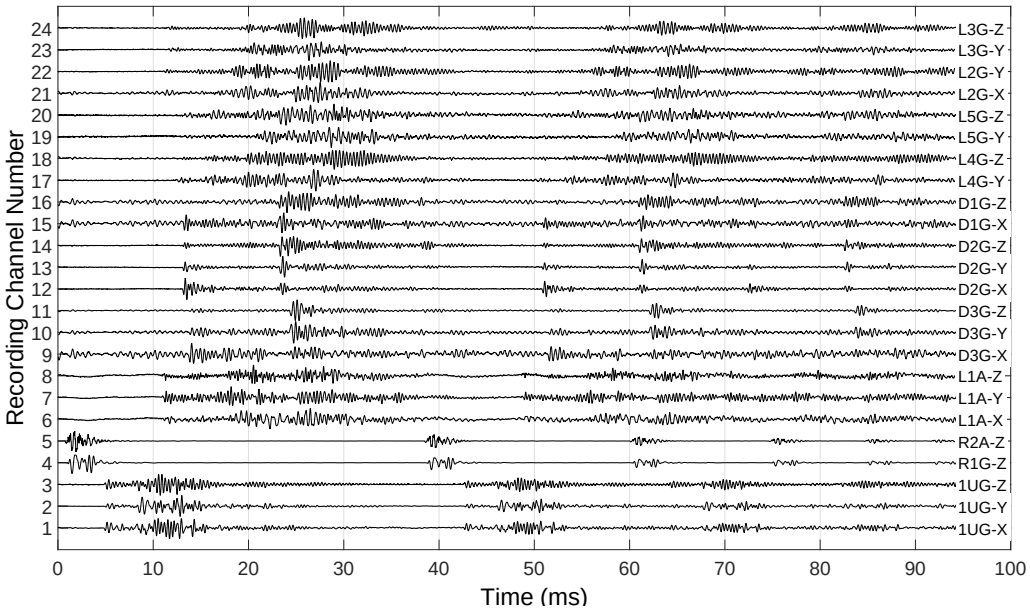

Figure 4.4: An example of a continuous seismogram containing the recorded signal generated by the pneumatic seismic source, taken at midnight on the 1st of November 2013. A distinct signal with good SNR was measured by all sensors without the need for data stacking. Multiple impact signals were observed each time the source was fired, which is a results of the slug rebounding off the stop end while the chamber was still pressurized. Pneumatic source signals were used to accurately measure the P- and S-wave arrivals. Each trace was labeled by the respective sensor name and axial component on the right edge of figure. All traces were individually normalized for viewing purposes.

weak and not discernible in unstacked data. A stack of one minutes worth of data (180 shots) was enough to recover this interference signal which was referred to as the EMI signal. It proved to be particularly useful as a reference signal as it recorded exactly when the piezoelectric source pulse was generated and this provided a more reliable zero-time measurement. This in turn could be used to calculate the timing error introduced by aligning all recorded data to the reference sensor, and correct for it (Figure 4.9).

After characterizing the reference signal drift and further investigating the offsets of different portions of the signal, it was established that the very first P-arrival remained stable in time (Figure 4.9) and that the rest of the signal was slowly changing. The slow change of the latter portion of the signal was the cause of the signal drift and so it was surmised that the likely cause for this was changing conditions in the borehole.

4.2.1 Electronic Clock drift

All electronic digitizing and recording hardware used during the experiment made use of an internal electronic clock to maintain time synchronization with all other recording elements. Ensuring time synchronization between the three netADC8 digitizers was essential for accurate signal time delay measurements of the order of a microsecond. The normal approach to correct relative clock offsets for a standard IMS microseismic monitoring system was to ensure system wide time synchronization using analogue time updates (ATU) that are generated from a reliable time source, such as GPS. The total number of clock counts reached at the end of an ATU period are recorded by the central server and an

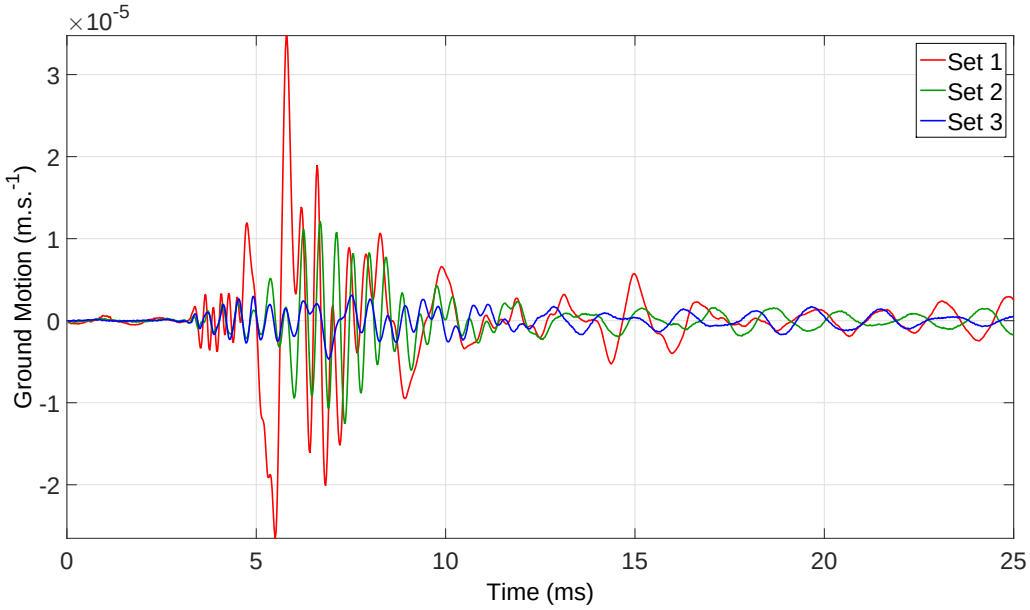

Figure 4.5: A comparison of stacked seismograms that illustrates the change in the reference signal, following alterations to the experiment. The piezoelectric seismic source was replaced following the maintenance work which occurred between Sets 1 and 2. The piezoelectric source driver was replaced with a modified unit between Sets 3 and 2 which resulted in a change to the water transmission pulse. Because of the significant change between signals, data recorded between such changes were treated as separate data sets.

inspection of the historical clock rates provides information on the necessary adjustments required in order to correct any timing offsets.

During the recording of Set 1 data, ATU was supplied to both the data loggers and source driver using pulse-per-second (PPS) analogue time update period, generated from a GPS time source. However, the change to a Synapse data collection server required one minute ATU for the three netADC8 units. The server software did not have the ability to handle seismic loggers which were receiving ATU every second. One second ATU was still required for the source driver to operate and so a compromise was required where the netADC8s received one minute ATU generated by the Central Site Computer, while the source driver continued to receive PPS generated by GPS time (Figure 2.2). This resulted in the problem that the recorded clock counts at the time of ATU were not taken relative to GPS time but instead to that of the clock of the Central Site Computer which itself did not conform to the required degree of accuracy.

All seismogram sections used for pre-stacking were created using the signal occurrence time measured by the reference sensor (excluding Data Set 1 - Section 2.5.5). The signal recorded by the other digitizers at the end of the minute may appear to have shifted when compared to the same signal recorded at the start of the minute. This was due to the disagreement between the clock of the netADC8 recording the reference signal and the clocks of the other two netADC8s which would be counting at slightly different rates.

Unfortunately netADC8s with high accuracy internal clocks were not available at the time of installation and instead the experiment had to make use of units equipped with lower accuracy quartz crystal clocks operating at a frequency of 6.144 MHz and a maximum drift error of 20 parts per million or 20 μs per second. Over the 60 second ATU duration this meant an absolute worse case offset of 2.4 ms was possible which was

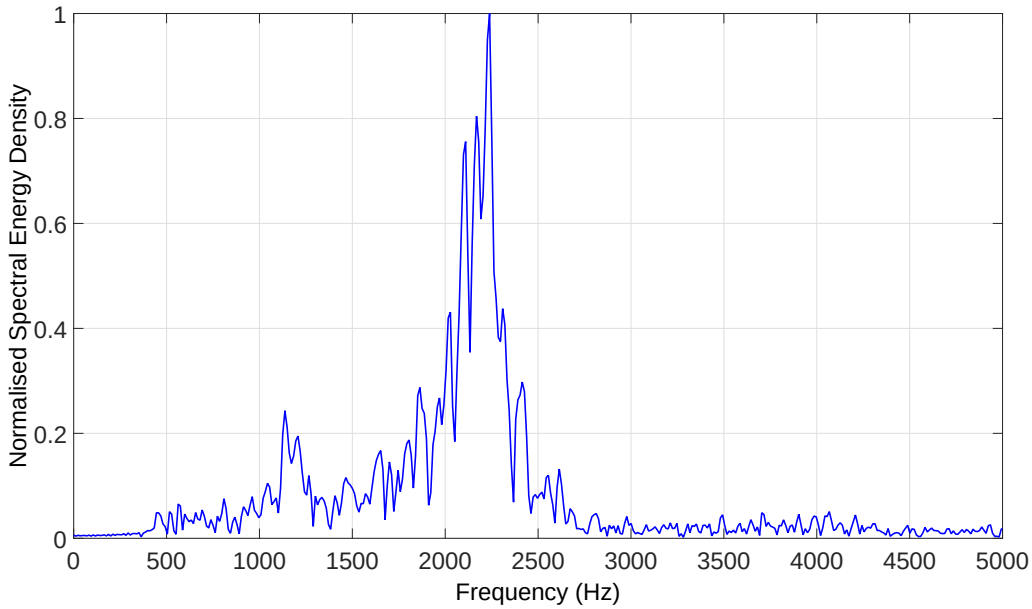

Figure 4.6: A plot of the spectral energy density of the three hour stacked signal attained from the Y-component of Sensor D2G, recorded on the 2ndof November 2013. A distinct peak is evident at 2350 Hz with most of the signal energy distributed between 1.6 kHz and 2500 kHz. This was a surprising observation considering that the piezoelectric source was supposed to be driven using a Ricker-wavelet with central frequency of 2.05 kHz. It was only later discovered that a software error in the control electronics of the source driver resulted in the output of a 2.24 kHz signal.

much larger than the desired minimum resolution.

However, a specific clock's offset over a fixed duration will remain constant provided the clock temperature and supply voltage remains constant. This feature was important as signal phase-lag measurements were made relative to waveforms recorded by the same digitizer and not performed using signals recorded on an absolute time scale. Any clock drift relative to absolute time was a systematic offset that was part of the construction of every pre-stacked seismogram, meaning that any signal aberration caused by stacking clock offset signals was a consistent feature for all pre-stacks as the unit's clock drift was constant.

Due to the mined out state of 5235 Level, there were no human activities in the level that would affect the ambient temperature. It was originally planned that temperature would be monitored using a sensor housed within the piezoelectric source driver. However the recording of this temperature data was prevented by a conflict with the serial ATU generated by the Central Site Computer. Temperature measurements were only possible after seismic data recording had ceased at the end of May 2014. Temperature was found to vary only slightly over a two week monitoring period with a maximum temperature difference of 0.8°C. Given that the clock drift temperature dependence was -0.035 parts per million/° C^2, a temperature difference change of 2.4°C between the different netADC8 units was required before clock offset would have had a measurable affect on signal phase shift. Such a large difference in enclosure temperature was not likely given that all three netADC8 enclosures were positioned side-by-side and housed electronics with steady power consumption rates. Digitizer electronics would undergo a temperature change when powered on after remaining off for an extended period as the device operation itself

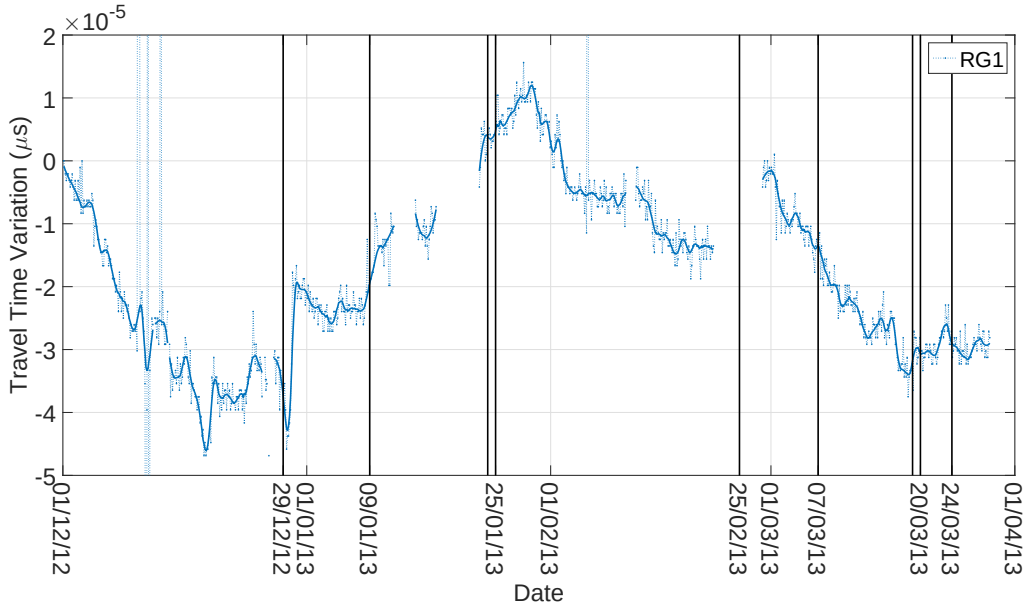

Figure 4.7: The calculated phase lag variation history of the reference signal for Data Set 1, recorded between the 1st of December 2012 and the 1stof April 2013. The maximum drift measured was significantly larger than anticipated which prompted an investigation into the cause. The actual degree of signal drift was only revealed after comparing it to the historical phase-lag of the EMI signal.

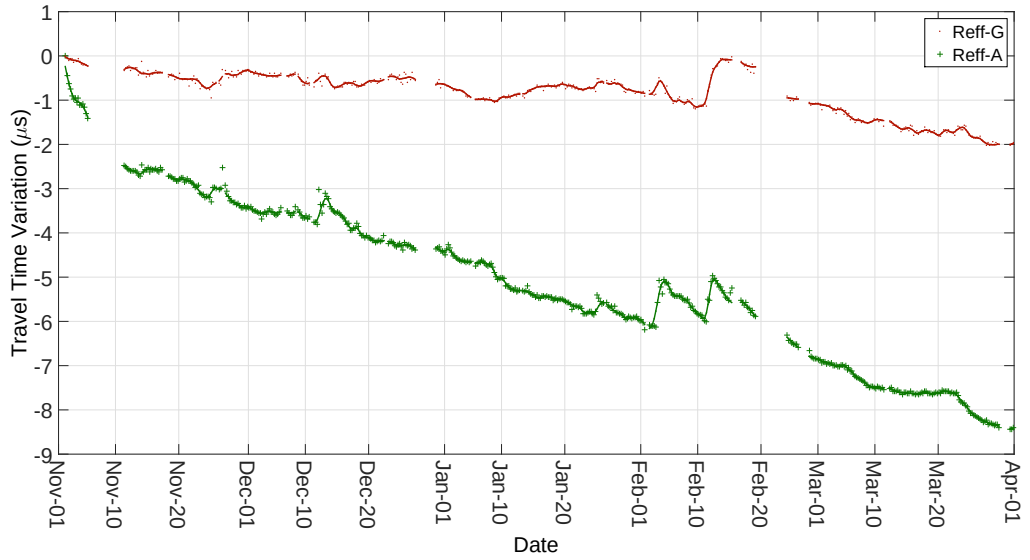

Figure 4.8: A comparison of the relative phase shift change measured by the two reference sensors Reff-G and Reff-A, from data Set 3. The significant overall drift and large difference between shifts provided evidence that the reference sensors were not suitable for stacking alignment and that a means of correction was required.

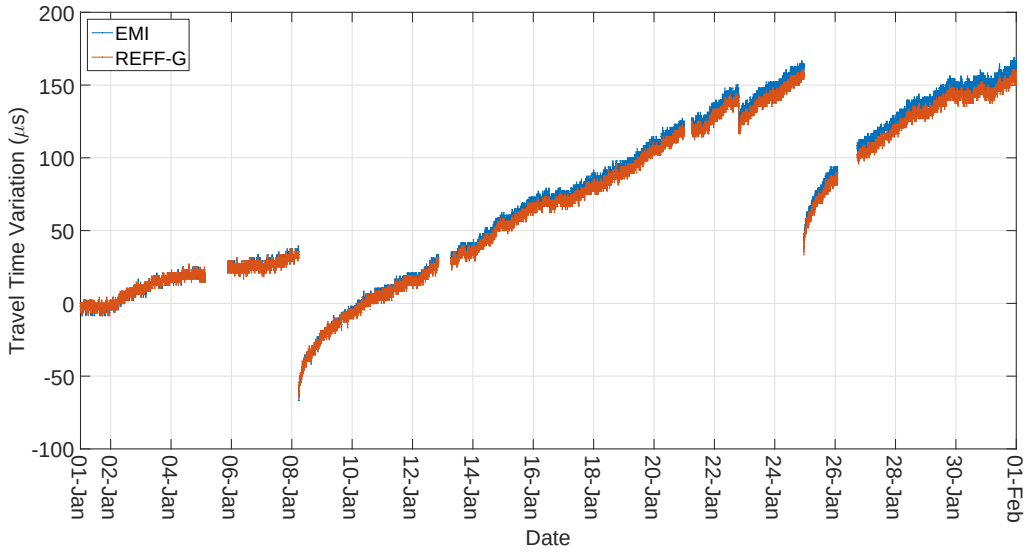

Figure 4.9: A comparison of the phase delay measured by the reference sensor and the EMI signal of netADC8 unit 3, using one minute pre-stacked stacked data recorded for the month of 1st January 2014. Only the initial 2350 Hz segment of the reference waveform (Figure 2.17) was used in the correlation process. The Historical phase-shift compares well with that of the EMI signal, which demonstrated that only this initial segment of the waveform was suitable for use in the pre-stacking process performed by the Central Site Computer.

generates heat which would warm the enclosure until an equilibrium point was reached.

The relative phase shift of the EMI signal between the three netADC8 units was calculated and it was found that despite a mean offset of 2 - 4 μs between the units, the offset remained constant over the recording period (Figure 4.10).

4.3 Travel Variation Data

Post-stacked data was created using the EMI signal as the zero-time reference on which all pre-stacked seismograms were aligned. Post-stacks were comprised of optimal set pre-stacked data recorded within a 4 hour period, separated by 3 hour intervals which meant that each stack shared 1 hours worth of data with neighboring stacks. These stacking periods were chosen in order to attain a reasonable improvement in SNR while also providing a sufficient resolution (number of data points) to observe short term velocity variations.

Unsurprisingly, the overall signal quality recorded after post-stacking varied greatly between the different sensors and different axial components. Cross-correlations performed on signals with a poor SNR produced low correlation co-efficients and the calculated phase-lag history for such signals were characterized by high degrees of scatter.

For this reason a minimum correlation threshold of 0.95 was applied to the pre- and post-stacking alignment of the reference signals, whilst a 0.85 threshold was used for travel time variation calculations on array sensors stacks. All measurements associated with correlation values below the minimum were excluded and this resulted in gaps in the travel time variation histories measured over the recording period of each set.

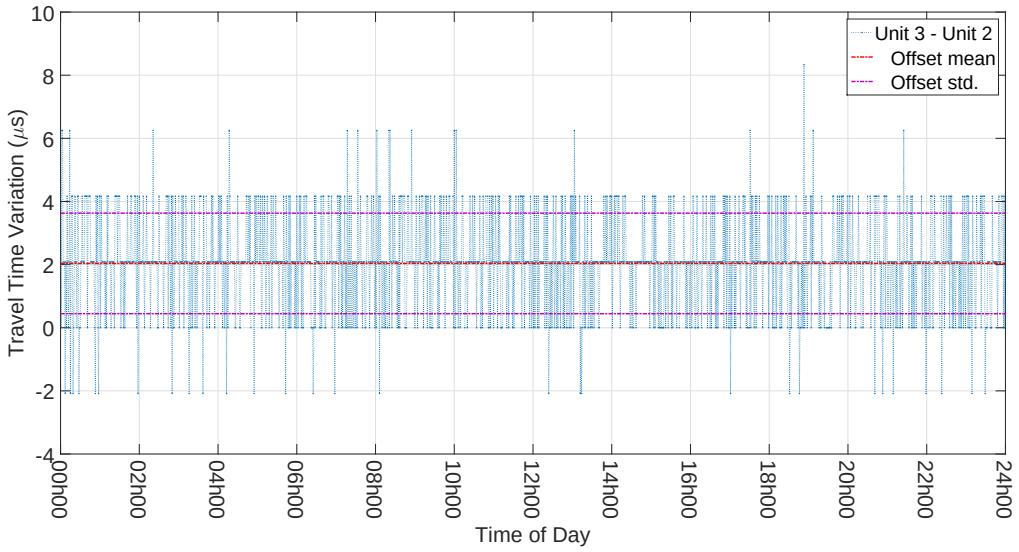

Figure 4.10: The phase shift difference between netADC8 units 2 and 3 of the EMI signal, measured over a period of 24 hours using one minute pre-stacked data recorded on the 1st January 2014.

Signal window boundaries for both the EMI and recorded piezoelectric signals were established for all channels using waveform information from the well defined signals recorded from the pneumatic source. Travel time variation calculations were performed on each individual recording channel using post stacked data. Unlike the noticeable signal pattern changes observed in the synthetic data discussed in Section 3.6.1, signals recorded by the experiment sensors remained largely consistent throughout each recording set as no significant ray bending was induced by the mining. This allowed use of an absolute reference scheme where the signals from the first stack in each data set were used as the master reference from which all subsequent travel time variations were measured. The use of an absolute reference was important as overall calculated trends were not affected by either missing or weakly correlated stacks as would be the case for a dynamic reference scheme (Section 3.2.3).

4.4 Travel Time Variation Results

4.4.1 Piezoelectric Source Data

Travel time variation histories were calculated for all recorded pre-stack data. The mining was still a considerable distance from the monitoring array during the recording of Sets 1 and 2 and so no trends related to mining could be resolved during these recording periods. Travel time histories for Set 1 can be found in Appendix H.

Once the recording for data Set 3 had started, the sub-level caving had drawn to within 10 m of the closest ray-paths which were sensors D3G, L4G and L5G (Figure 4.12).

The effect of first ring blast conducted on the 8^{th} of November was unfortunately missed as communications to the experiment site were down at the time (due to level maintenance), preventing the source driver from operating. Once recording resumed on the 11th of November, travel times for sensors L4G and L5G had decreased by as much as 0.2 %. All successive ring blasts recorded from the 26th onwards showed a distinct

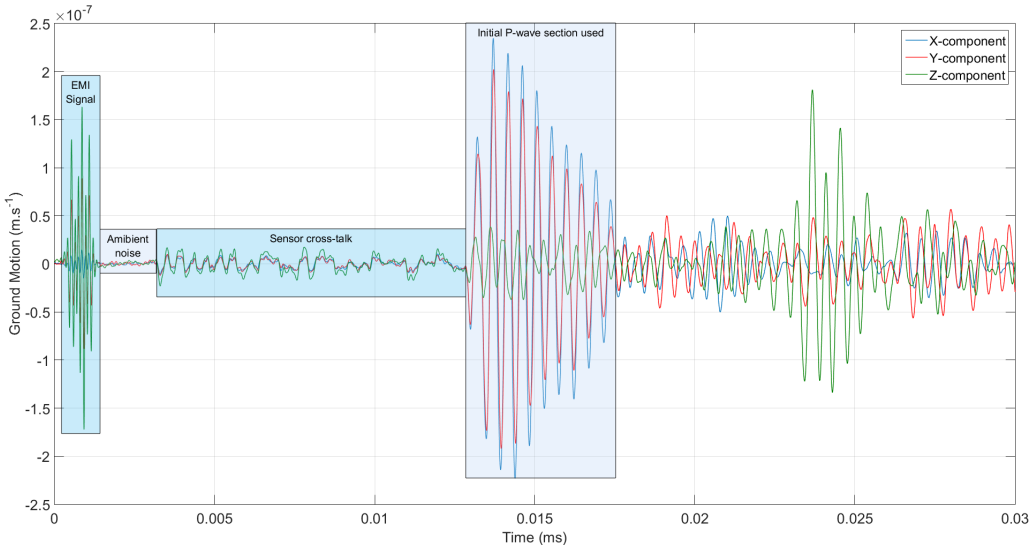

Figure 4.11: A break down of the sections of a 24 hour post-stacked seismogram from Sensor L4G, that were relevant to the travel-time variation calculation process. The EMI signal was used as the zero time reference. Ambient noise, along with the P-wave sections were used to calculate SNR values. Sensor cross talk (from the reference sensor) was a fixed waveform and had to be distinguished from the actual ambient noise. This example of waveform has an SNR of 145 on the X-component.

travel time response, characterized by significant increases in the signal delay for these two sensors. This jump was subsequently followed by a steady decrease in the travel time which was suggestive of a blast induced damage followed by a post-blast relaxation process that was affecting the medium velocity. This behavior was observed for all blasts between the 26$^{\text{th}}$ November to 11$^{\text{th}}$ of February when the final blast was conducted for the Halo 5205 Level. The largest excursions were recorded by Sensor L5G, on the 13$^{\text{th}}$ and of December (65μs or 0.5 %), the 8$^{\text{th}}$ January (60 μs or 0.5 %) and the 5$^{\text{th}}$ of February (70 μs or 0.8 %). These dates correspond with the blasting of Crosscut 7 rings which featured the shortest intercept distance to sensor ray-paths.

Table 4.1 lists the date of blasts conducted during the recording of Data Set 3, and compares the distance between the ring position and the ray-path of sensor L5G to the observed travel time delay.

Despite the slow relaxation process, a permanent offset or increase in travel time was also observed for Sensors L4G and L5G of 70 μs and 25 μs respectively which may have been a result of permanent damage created by the extension of the mining fracture zone.

The travel time history of Sensor D3G on the other hand did not exhibit the same pronounced response to blasting, instead showing only small increases in travel time with the largest excursion of 14 μs.

4.4.2 Pneumatic Source Data

In order to verify whether the distinct jumps in signal travel time were caused by changes in the seismic medium or some other unknown measurement artifact that derives from the referencing scheme or changes in the source signal, travel time variation calculations were performed on seismic signals generated by the pneumatic source. The pneumatic source was operated in parallel with the piezoelectric source from the 1st of November

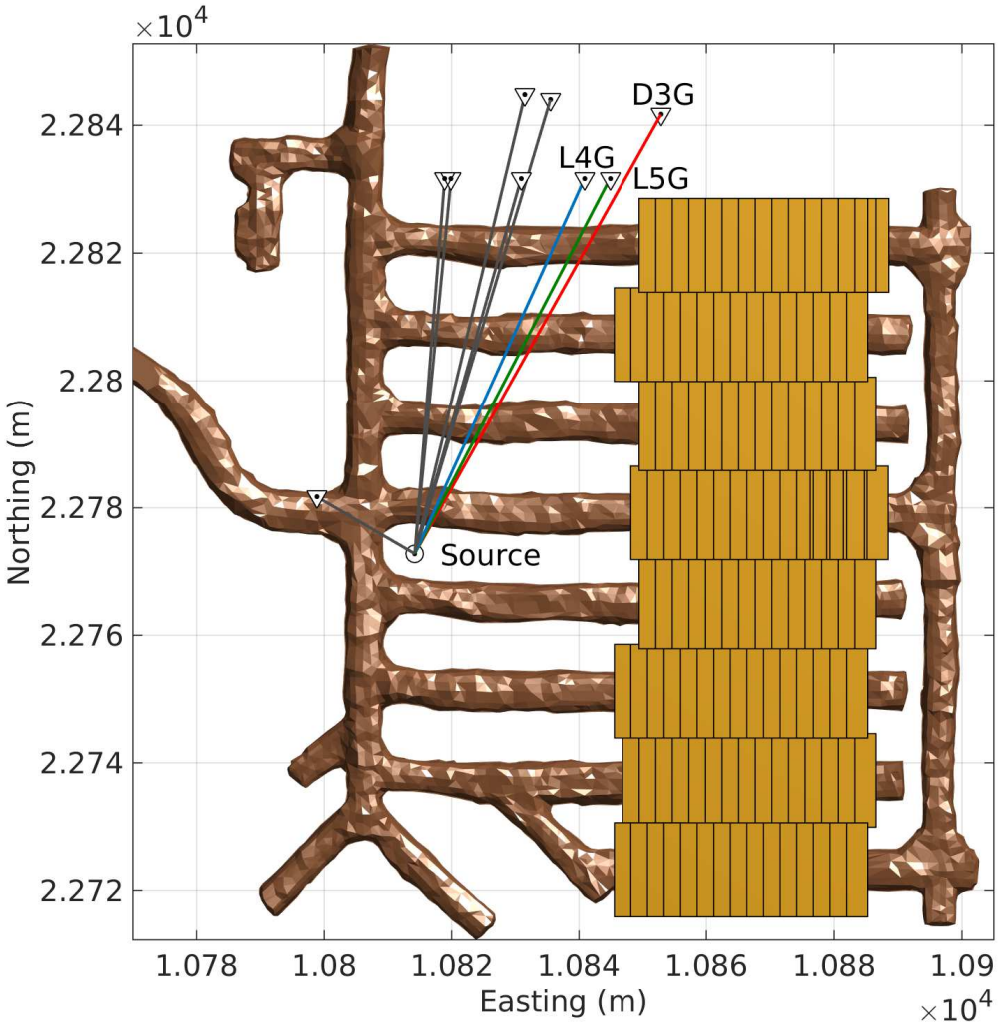

Figure 4.12: The state of the sub-level cave mining on the 5205 level on the 2nd of November 2013, when the recording of Data Set 3 was started. Mining had not yet intercepted with the closest ray-paths of sensors L4G, L5G and D3G.

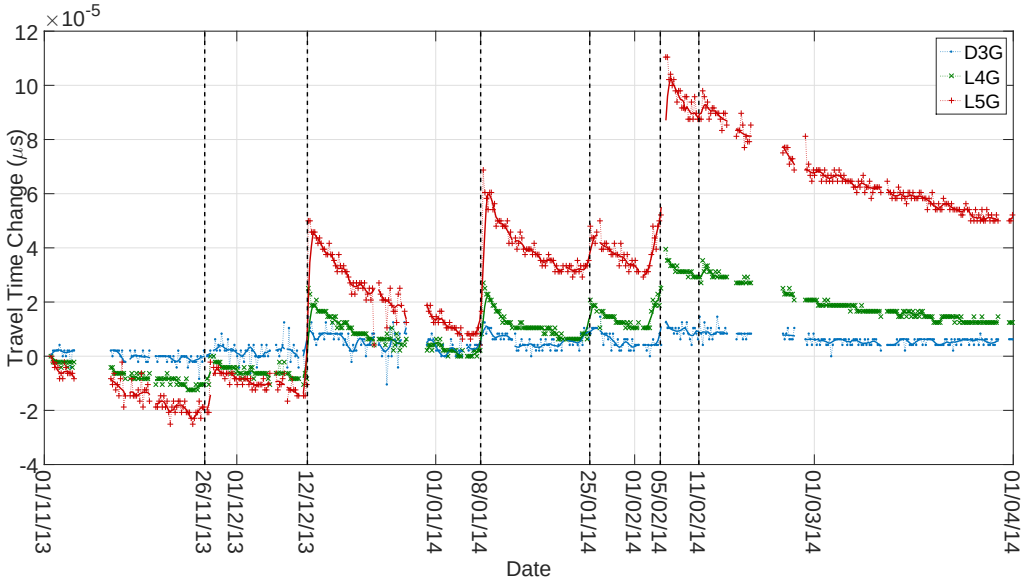

Figure 4.13: Travel time variation measured from the stacked data collected during of the period between the 2nd of November 2013 to the 1st of April 2014 for the three sensors that had the closest ray-paths to the sub-level mining. Days when when rings where blasted in Crosscuts 6, 7 and 8 are marked with vertical dashed lines. Distinct jumps followed by a steady recovery in signal travel time where observed after every blast. A smoothed cubic spline for each data set is utilized for visualization proposes.

Date of Blast	Blast Seq.	X-Cut	Ring	Approx. Dist. (m)	$\Delta\varphi_{L5G}$ (μs)
26/11/2013	1	6	R15	16	18
12/12/2013	2	5	R15	21	65
12/12/2013	3	7	R16	6	65
08/01/2014	4	7	R17	4	60
25/01/2014	5	6	R16	13	17
04/02/2014	6	5	R16	19	19
05/02/2014	7	6	R17	11	70
05/02/2014	8	7	R18	1	70
11/02/2014	9	5	R17	21	10

Table 4.1: A listing of ring blasts and the maximum excursion in signal delay measured during the final mining stage of the 5205 Level. The exact time of day of each blast was not specified by the mine and so may have occurred at any point during the day. The approximate distance was the estimated using the shortest distance between ray-path L5G and the closest edge of the modelled drawbell. $\Delta\varphi$ is the maximum change in signal phase delay measured by L5G following each blast.

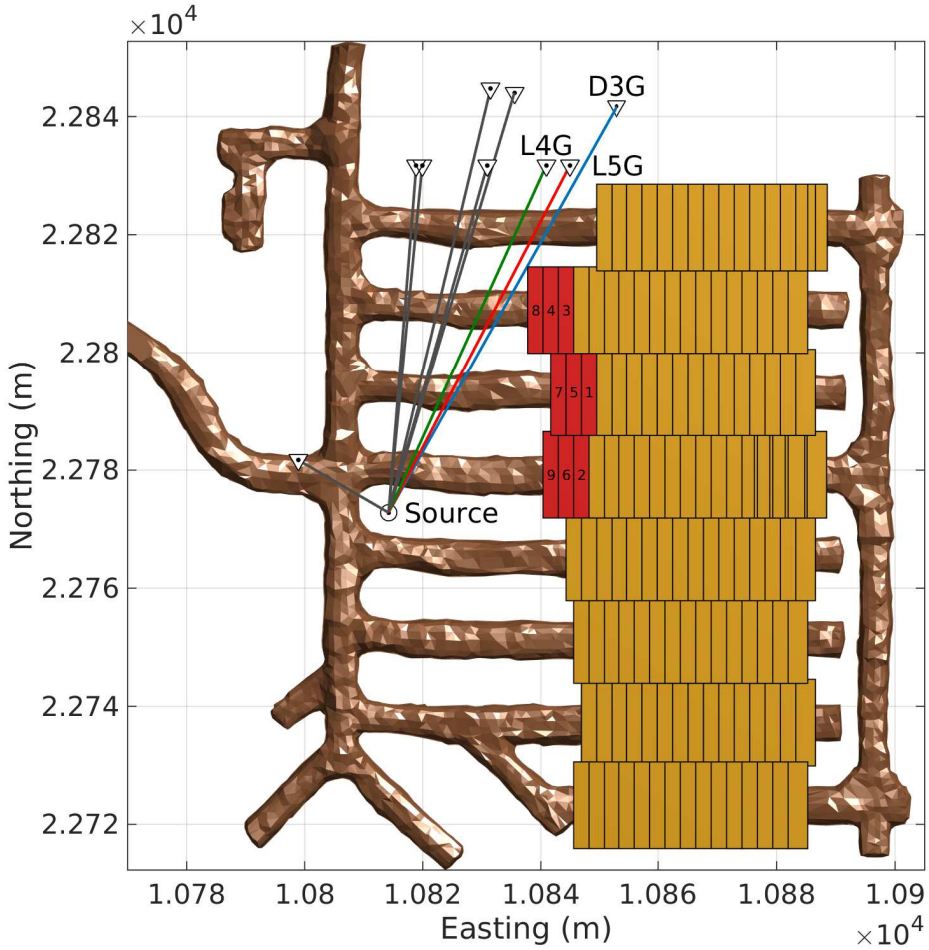

Figure 4.14: A rendered model of the final stages of the sub-level caving progression of the Halo 5205 Level, between the 26^{th} of November 2013 and the 11^{th} of February. The rings blasted during the recording of data Set 3 are shown in red and labeled with the order in which the rings were blasted (Table 4.1). The straight ray-path between the source and the three closest sensors L4G, L5G and D3G are represented by green, red and blue lines respectively. Ring 8 was the closest the mining advance came to these ray-paths.

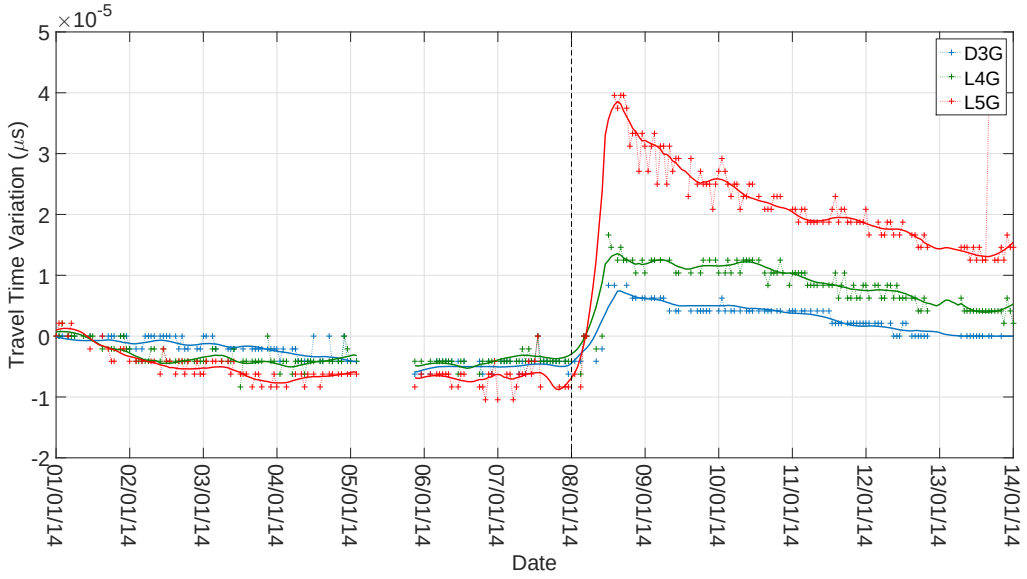

Figure 4.15: Travel time change measured from the pneumatic source data collected between the 1st to the 14th of January 2014 for closest ray-paths sensors. A distinct jump followed by a steady recovery in signal travel time was observed following the blast conducted on the 8th of January, matching the behavior measured using stacked piezoelectric source data. The maximum excursions measured were fairly consistent between the two source types. A smoothed cubic spline for each data set is utilized for visualization proposes.

2013 until the $6^{th}$of March 2014 following a mechanical failure. The source was fired automatically on an hourly basis and its signal was identified using the threshold crossing and cross-correlation method (Section 2.5.4).

Extraction and archiving of the pneumatic shots was not as regular as piezoelectric source stacked data (possibly due to periods when pneumatic pressure supply was reduced significantly), however calculation of short travel time variation histories of before and after blasting was still possible. Signal phase-lag changes calculated for sensors closest to the mining front exhibited the same signal delay behavior following the occurrence of a close proximity blast, as observed in the stacked piezoelectric source data. This was characterized by a sudden yet distinct increase followed by a slow but steady decrease. The extended decay pattern cannot be calculated due to missing pneumatic data so a permanent offset delay cannot be confirmed.

This agreement of travel time variation behavior between the piezoelectric and pneumatic source data confirms the observed seismic response to close proximity ring blasts and that the observed trends are not peculiar artifacts that arise from changes in the reference signal and the corrections applied using the EMI signal.

4.4.3 Distant Sensors

The travel time variation measured using data recorded by sensors further from the mining front, namely L1A, L3G, D2G and U1G exhibited little to no identifiable response to the mining (Figure 4.16). The majority of cross-correlation values obtained using data from sensors L2G and D1G fell below the minimum threshold of 0.85 and were not included in the analysis.

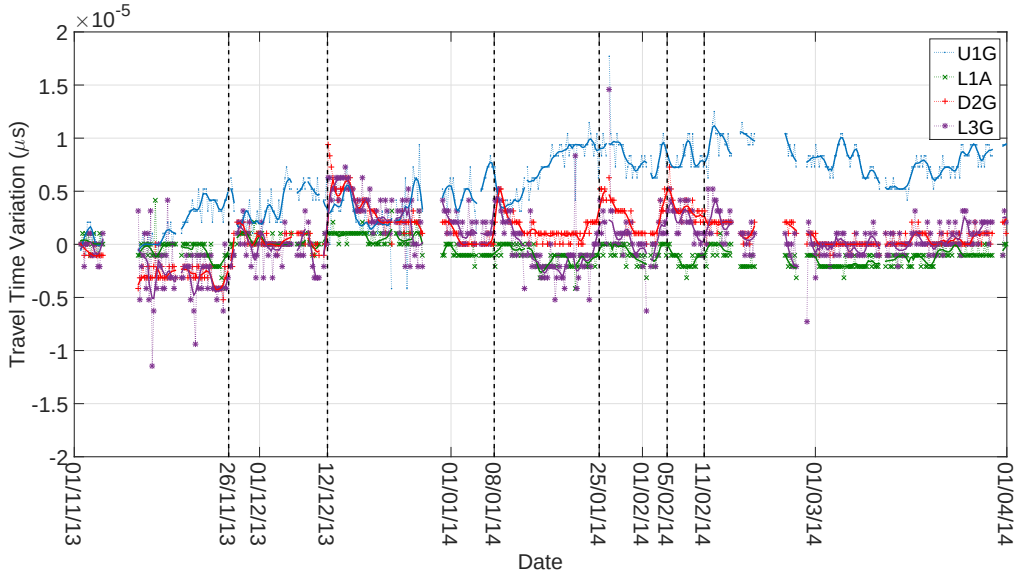

Figure 4.16: Travel time variation measured from the stacked data collected between the 2nd November 2013 and the 1st of April 2014 for sensor ray-paths located further from the sub-level mining. Days when rings were blasted in Crosscuts 6, 7 and 8 are marked with vertical dashed lines. Sensors D2G and L3G exhibit minor blast related responses while remaining sensors exhibit none at all. A smoothed cubic spline for each data set is utilized for visualization proposes.

Sensors D2G and L3G did exhibit small blast related responses similar to those observed from sensors D3G, L4G and L5G. The largest observed change for both was 10 μs after the blast which occurred on the 12^{th} of December. Sensors L1A and U1G, which were located the furthest from the mining, displayed no perceivable response to the blasting.

Chapter 5

Discussion

5.1 Numerical Modelling Results

5.1.1 Waveform Change

Dynamic wave numerical modelling highlighted two important sources of synthetic signal change that arose when the modelling the final stages of the sub-level mining of the Halo 5205 Level. The first problem encountered was a change in the mixing of the orthogonal components of the waveform, caused by the change in incident angle as a result of changing model geometry (Section 3.2.1). The second problem was the significant attenuation of high frequencies which manifested as stretching of synthetic waveforms (Section 3.2.2).

This change in waveform shape, observed between the different modelled mining steps manifested as a problem for the time-domain based phase lag calculation process which is dependent on comparing highly similar waveforms. Seismogram rotation can be used to correct for the incident angle of the wave but requires knowledge of the wave back angle which can be calculated using principle component analysis. Waveform stretching on the other hand was handled through the use of cubic spline interpolation to counter shrink the comparator waveforms to best match the reference, making it a search parameter of the phase lag calculation process.

A dynamic reference scheme was also used to contend with the changing synthetic waveforms by exploiting the fact that each incremental step in the modelled mining process caused only small changes in the synthetic waveform. This was a simple solution employed to overcome waveform evolution, however the method suffered from accumulative error when attempting to calculate total signal delay changes between the first and last modelled mining step.

An alternative to the time-domain based correlation method is a frequency domain based approach to measure phase delay difference, eliminating the need to correct signals to in order to maintain waveform shape [40]. A Discrete Fourier transform carries information of both the amplitude and phase of every frequency with the phase given by the arctangent relation between the real and imaginary parts :

$$\varphi_i = \arctan\left(\frac{\text{imag}\,(y_i)}{\text{real}\,(y_i)}\right) \tag{5.1}$$

Where:

- φ_i is phase of the frequency f_i.
- y_i is the complex value of Discrete Fourier transform for f_i.

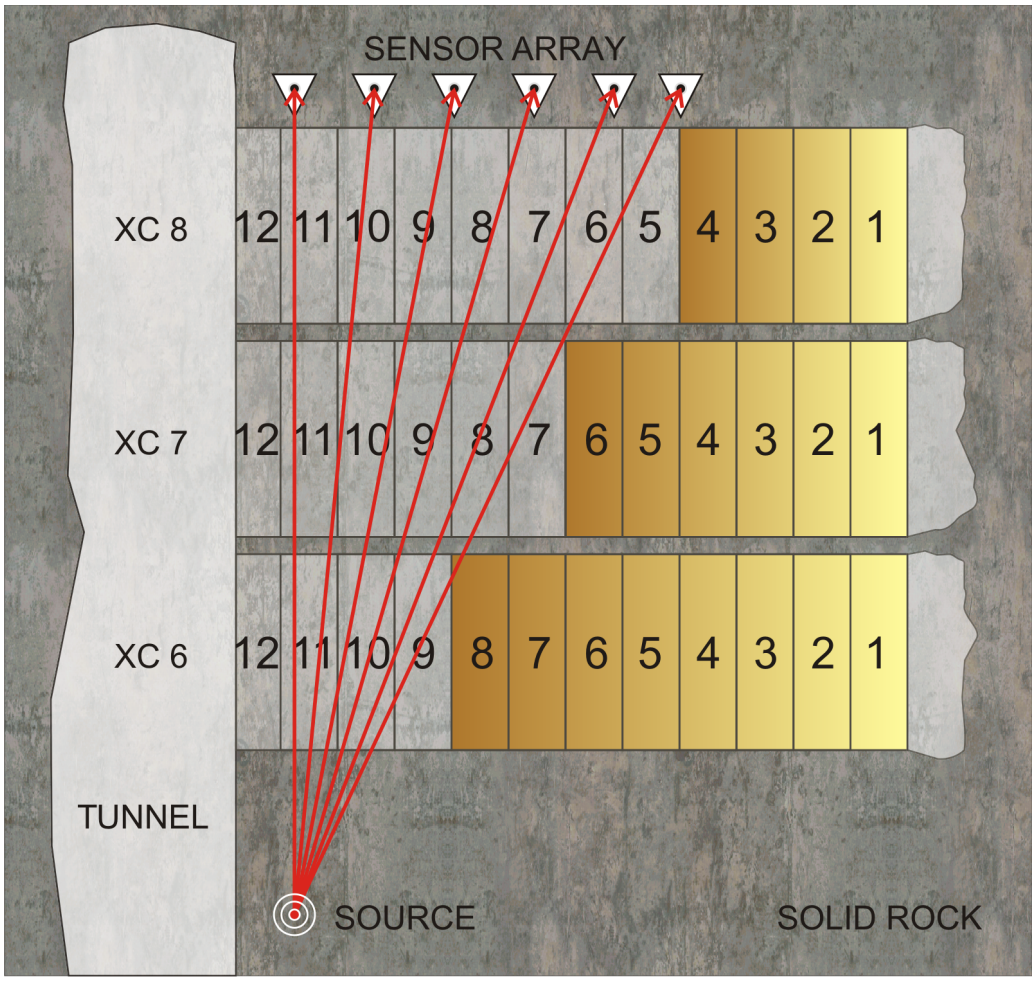

Figure 5.1: An illustration that highlights the short coming of the sensor array for the purpose of mine front advance tracking. The phase delay caused by ray-path bending was more sensitive to the front advance of Crosscut 8 as it intersects with ray-paths after fewer advance steps when compared to Crosscuts 7 and 6. This gives the ray-paths increased exposure to the mining sequence of Crosscut 8 (8 steps as opposed to 6 and 4) providing a larger difference between the phase lag measured by the different sensors. Thus the estimation method was more sensitive to the changes in Crosscut 8 and likely to produce an accurate inversion.

5.1.2 Array Limitations

Two major limitations of the source and sensor array arrangement were also highlighted through the numerical modelling process. Source-to-sensor ray-path coverage of the mining region was revealed by the difference between phase delays calculated for the mining advance of Crosscut 8 when compared to Crosscuts 6 and 7 (Table 3.5 and Figure 3.15). The phase delay increase caused by Crosscut 8 advance was measured after its first modelled advance step while Crosscuts 6 and 7 could only be distinguished after model step 27 of the normal modelled mining sequence, making the experiment more sensitive to Crosscut 8 mining advance.

The second problem identified was the significant signal amplitude decrease in the

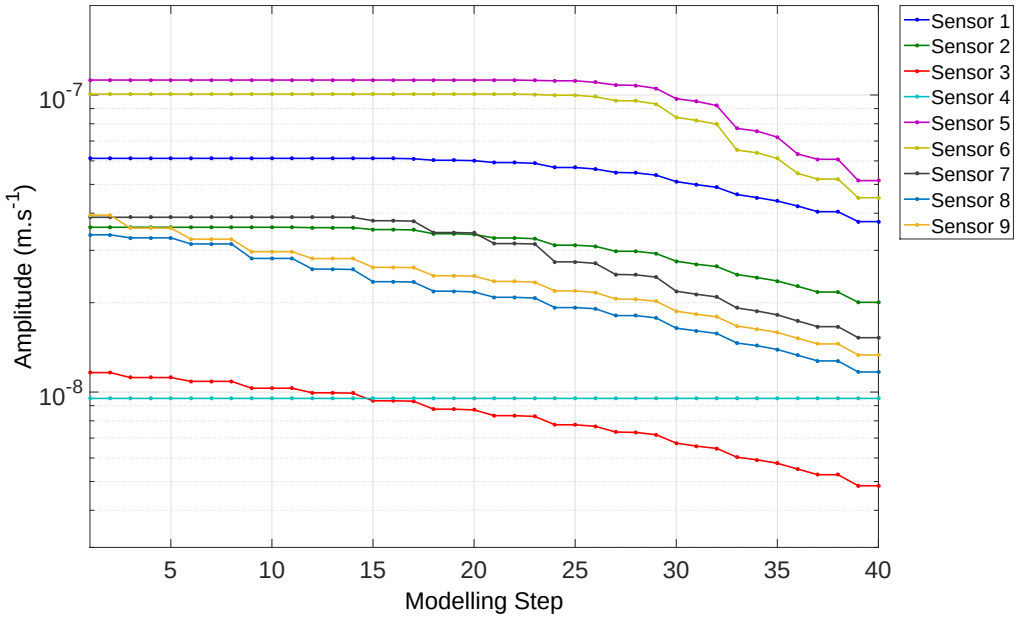

Figure 5.2: The expected amplitude attenuation calculated using basic inelastic scattering and geometric spreading for each modelled mining progression step based on the signal delay increase. Sensor 4 is positioned outside of the mining region and so was not subject to ray-path changes.

latter part of the modelled sequence (Figure 3.18). Three different modelling properties contribute to signal attenuation namely, inelastic scattering, geometric spreading and the interaction of waves with the tunnel and mining geometry.

An inspection of sensor positions in the model shows that Sensors 5 - 9 were positioned in the fracture zone of the mined out regions of the 5235 Level, making inelastic attenuation more pronounced for these sensors. The distance traveled by the signal through these fracture regions also increased as the mining front advanced. However the combination of inelastic scattering and increased path length attenuation through geometric spreading was not enough to explain the two orders of magnitude drop in signal amplitude observed between the first and last model steps. A simple investigation using the attenuation resulting form of geometric spreading, which follows a $\frac{1}{r}$ relation [26, 30], combined with inelastic attenuation (Equation 3.1) and FMM derived travel times showed an amplitude drop of less than one order of magnitude (Figure 5.2) from the first model step amplitudes.

This means the waveform interaction with the changing void geometry was the largest contributor to signal attenuation whereby mining advance was creating a seismic shadow over the sensor region. As mined out geometry progressed to the point of intersection with the source-to-sensor ray-paths, it cut off the direct line-of-sight between the two. The mined out excavation reflects most of the source energy, which only allows the diffracted wave energy to reach the recording positions (Figures 5.4 and 5.3), which results in a significant reduction in signal amplitude.

This highlights the importance of sensor positioning by taking into consideration the signal distribution with respect to the planned mining progress. Such an investigation could be handled using dynamic wave numerical modelling to the aid the planning of future array designs in a specific mining setup. Further considerations would include a sensor distribution that creates sufficient ray-path networking to cover the block-caving region as well as accommodate the possibility of using multiple active seismic sources to

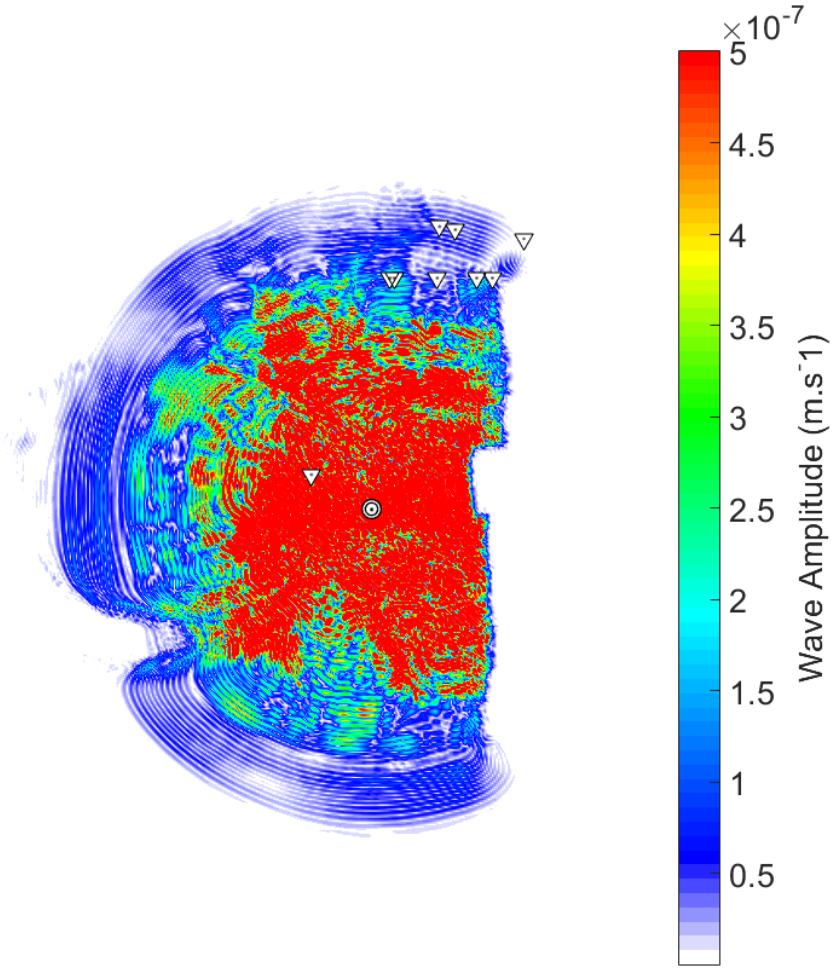

Figure 5.3: The synthetic seismic wave field modelled using E3D for step 1 of the normal mining sequence model. The source has a direct line of sight to all sensors and synthetic seismogram amplitudes are of the order between 10^{-7} and 10^{-8} ms^{-1}. Wave field was taken in the horizontal plane passing through the position of the synthetic source, marked with a white circle while sensors are marked with white triangles.

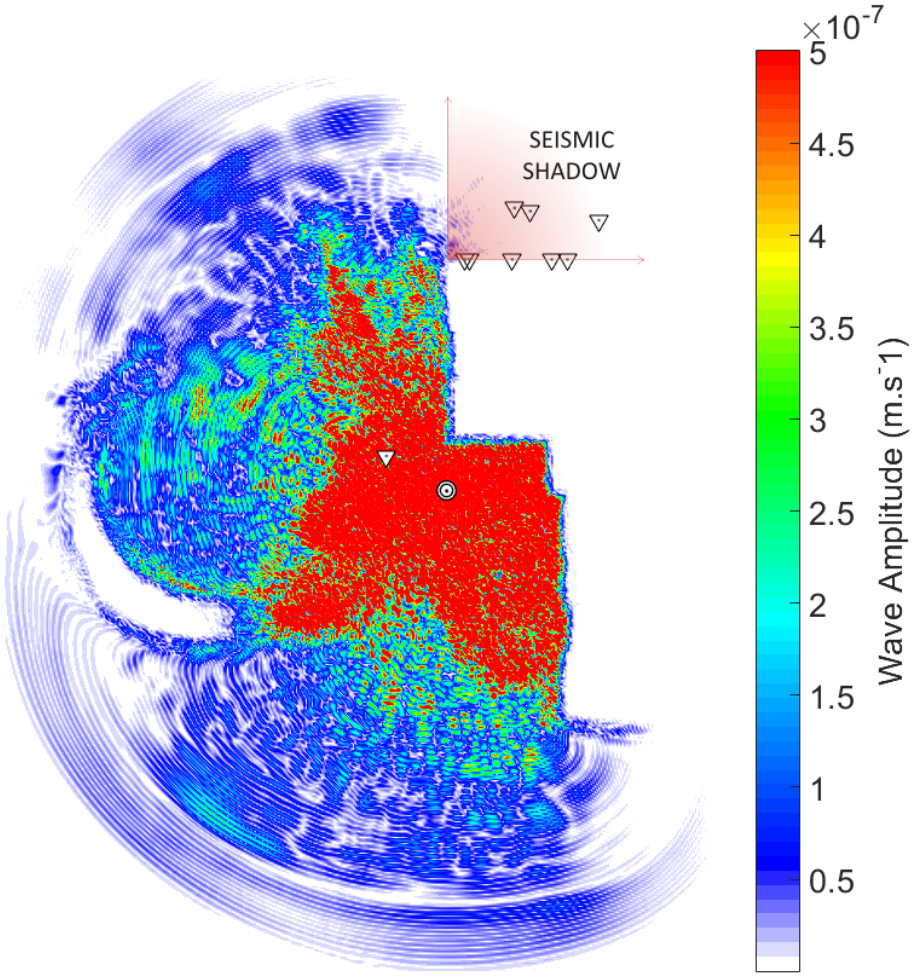

Figure 5.4: The synthetic seismic wave field modelled using E3D for step 40 of the normal mining sequence model. The source no longer has a direct line of sight to all sensors and only a small portion of diffracted wave energy reaches the sensor positions. Seismogram amplitudes are of the order between 10^{-9} and 10^{-10} ms^{-1}. Wave field was taken in the horizontal plane passing through the position of the synthetic source, marked with a white circle while sensors are marked with white triangles.

further enhance the coverage.

Unfortunately, a comprehensive comparison could not be drawn between the modeling and physical experiment results due to the sub-level mining terminating before intercepting with sensor ray-paths. This includes an assessment of the potential problems discussed (seismogram rotation, high frequency attenuation and seismic shadow attenuation) that might have affected the recorded signal given the scenario where the mining of 5205 Level had completed as originally planned.

Despite the less than ideal ray-path coverage, the extend of the modelled mining front advance was successfully attained using the look-up table scheme after the point where crosscut mining had intercepted with sensor ray-paths. It should be noted that the method performed rather poorly when attempting to use a look-up library that contains many different possible mining front advance configurations that share highly similar phase delays values. A look-up table based method might prove unstable for block cave tracking as it would require a good understanding of how the cave will evolve over time. If the expected model was incorrect to begin with, then the measured phase delays would not match values in the look up table. Instead 3D tomographic inversion schemes would be better suited to estimating block cave growth.

5.2 Physical Experiment Results

5.2.1 Time Synchronization

The full signal recorded by the reference sensor proved to be unstable in the long term, despite overall stability of the signal generated by the piezoelectric seismic source. Its long term instability was attributed to the gradual drop of the level of the water contained in the borehole in which the piezoelectric source was installed and caused by slow evaporation. The decrease in water level changed the length of the reflection cavity, resulting in a gradual change in the coda of the recorded reference signal. This precluded the use of the reference sensor(s) full waveform as a zero-time reference for post-stacking and necessitated the use of the stacked electromagnetic interference, created the high voltage driving signal, as the zero-time reference. This EMI reference scheme was also used to compare the relative clock-offset between the different digitizers for the pre-stack data and establish a lower bound error on measurable phase delay.

The EMI signal may have originally been an unintended feature of pre-stack recording but without it, timing correction would not have been possible and the entire pre-stack data set would have been rendered unsuitable for travel time variation studies. This highlights a design flaw in the experiment approach and the need for a stable zero-time reference signal which specifically links all digitizer units together.

An ideal setup for future experiments of a similar nature would employ stable high accuracy internal clocks with temperature compensation and short interval time synchronization updates. In addition to this, a low voltage feed of the output signal generated by the piezoelectric source could be linked to a single data channel on each seismic digitizer so that each unit records specifically when the piezoelectric source was fired. Data pre-stacking would be performed separately for each digitizer, eliminating any uncertainty created by relative clock-offset between the various digitizers. Careful consideration should still be taken with regards to the effect of temperature changes on the individual clocks should digitizers be subject to large temperature variations.

A low sensitivity seismic sensor affixed directly to the source would still be necessary to ascertain the working state of the piezoelectric source as well as study any changes to the output generated over extended periods of operation. Care should be taken to dampen the recorded amplitude from this sensor to a suitable level in order to reduce the effect of signal cross-talk which is enhanced by stacking.

5.2.2 Signal Quality

Stacking proved effective at recovering the weak seismic signal generated by the piezoelectric source however SNR attained from various sensor components ranged between 2.5 to 120 after using 4 hour stacking periods (64800 shots). Signal amplitude recorded at the different sensors was dependent on sensor position with respect to the tunnel geometry and not directly related to the source-to-sensor distance. Sensors in boreholes L and U were positioned in the seismic shadow cast by the adjacent crosscut tunnel on the mined out 5235 Level which resulted in an overall lower SNR attained for these sensors despite some these sensors being among the closest to the source.

As previously mentioned in the discussion concerning modelling results (Section 5.1.2), sensor position with respect to tunnel geometry should be an important consideration in array design with the aim of placing sensors a sufficient distance from existing and future mining while also minimizing source-to-sensor distance.

The highest SNR attained for the furtherest sensor, D3G, was 120 while its average SNR was 46 using the 4 hour stacking period scheme. Using the consideration that signal amplitude is proportional to SNR and the assumption that noise levels are constant throughout the mine (not strictly true) a maximum source range can be extrapolated for. Mine rock properties from Table 3.1 and a SNR of 3.5 (considered the minimum useful threshold - Section 3.6.2) were applied to the amplitude attenuation equation 3.2, which suggests a maximum useful range of 200 m for the piezoelectric source under these recording conditions. It should be noted that due to the source driver programming error the source was only outputting half its intended driving amplitude which in turn suggests a maximum detectable range of up to 250 m for the device. It should be noted that this form of range extrapolation does not take into account the absolute minimum detectable ground motion for the geophone sensors and the digitizer it is connected to.

5.2.3 Phase Delay Measurements

Measurement of travel time changes using data from sensors L5G and L4G showed a distinct pattern following the occurrence of a ring blast in close proximity to the raypath of these sensors (Figure 4.13). A large increase in travel time was observed directly after each blast, which was followed by a gradual decrease or relaxation which indicated that the maximum increase in phase delay was not permanent and instead related to a dynamic healing process of the fractured medium.

This type of seismic velocity relaxation has also been observed in an experiment conducted in a similar mining environment were high sensitivity seismic velocity variations were measured using ambient seismic noise cross-correlation techniques [38]. Similar coseismic velocity drops, followed by gradual relaxation where also reported on a much larger scale following the occurrence of a large earth quakes [6, 22, 35, 11]. This relaxation of seismic velocity is attributed to a healing processes of the rock medium were micro-fractures that were initially opened by the blast shock wave and subsequent stress redistribution, slowly close again and the rock returns to a more competent state. The rate of micro-fracturing is initially at its highest directly following the blast but rapidly slows while the competing rate of micro-fracture closure increases to the point where closure is the dominant process and the rock is undergoing healing. The healing process will continue until a state of equilibrium is reached that is dependent on the local stresses.

It should be noted that an absolute reference was used for the calculation of the travel time variation history for Data Set 3 which started on the 2nd of November 2013, while the mining process was ongoing. A close proximity blast on Crosscut 8 was conducted on the 28th October 2013. It is reasonable to assume that recording started during the

medium healing process following that blast, based on the observed decrease in travel time between the 2nd and 26th of November 2013.

The phase delays measured by the physical experiment were an order of magnitude smaller than those calculated by the modeling for the same mining front advance. Despite this, both sensors L5G and L4G saw a permanent increase in the signal travel time after mining operations were halted, with respect to the signal recorded on the 2nd of November 2013. This implied that the two ray-paths were subject to a small degree of bending, possibly caused by the fracture zone extension created by the final ring blast in Crosscut 7.

Sensor D3G did not produce large changes in both data recorded using the piezoelectric and pneumatic seismic sources. It was surmised that the installation coordinates of sensor D3G were incorrect and that its physical position did not match what was originally planned. Unfortunately the original borehole survey record was lost so this could not be verified and the correct positions of D3G, D2G and D1G could not be confirmed.

The remaining sensors had ray-paths that were located far from the mining front and exhibited weak responses to the blasting while maintaining constant baselines which was expected (Figure 4.16). Sensor UG1, however exhibited an overall increase in phase delay. The cause of this increase was not well understood but given the relatively small degree of change (< 0.1 %), it may be related the redistribution of local stresses that results from the sub-level mining process.

5.3 Block Cave Tracking System

The sub-level mining front tracking experiment verified that a low power piezoelectric seismic source can be used in conjunction with a standard micro-seismic monitoring array to measure very small changes in seismic travel time brought about by mining activities. The numerical modelling explored signal behavior when a scanned medium was subjected to significant change brought about by mining. Both investigations provided valuable insight needed for developing the methods for routine block cave tracking system using active seismic source technologies.

The horizontal cross-section or footprint of a block cave mine is dependent on the dimensions of the mined ore body. From a survey of existing block cave mines including Ridgeway Deeps, Cadia East, Telfar and Argle Mines it was established that cave dimensions vary between 150 m to 500 m across. In Section 5.2.2 it was postulated through range exploration that the piezoelectric source as employed in the experiment, may be sufficient for smaller block cave dimensions but too weak for larger types. From Section 5.1.2 it was found that increased signal travel time, seismic shadow expansion and increased exposure to fractured media lead to significant signal attenuation, requiring that a suitably high enough SNR is achieved before the array is subjected to significant ray-path bending.

There are several different solutions that could be applied in order to increase SNR and ensure useful signal recordings after extensive growth of the cave back.

5.3.1 Seismic Sources

5.3.1.1 Piezoelectric Transducers

The Cave Front Tracking Experiment employed a SRX-1 piezoelectric source, a device which was optimized for underwater acoustic communication. Because it was required to operate in a water filled borehole, the device had the disadvantage of radiated power loss through the seismic transmission coupling between the water filled borehole and the surrounding rock. Larger, more powerful piezoelectric transducers that couple directly to

rock could be designed for the specific purpose of active seismic tomography over block cave mine size distances. Alternatively multiple transducers could be clustered together and operated in parallel to act as a single source, linearly increasing source power output based on the number of sources added.

Should more than one independent active source be operated in the monitoring array, then each source would be require its own operating time window in order to prevent signal recording overlap. For example if three piezoelectric sources are operated simultaneously, each pulsing at a rate of 3 Hz, then each of the sources would fire sequentially with a 1/9 second separation between pulses.

5.3.1.2 Alternate Seismic Sources

Different types of active seismic sources are also available [14, 28, 34], which are capable of higher power output than the piezoelectric source. The field testing both of the pneumatic and eccentric rotating mass source during the experiment yielded encouraging results (Section 4.4.2 and Appendix G) in this regard. The pneumatic seismic source showed potential as a superior substitute for the piezoelectric source, as a result of it generating a significantly more powerful signal with near identical patterns between shots, making it suitable for data stacking techniques. This makes the device well suited for the longer ranges required for block cave tracking, however the mechanical reliability of the device remains unproven. The issue however, can be overcome through improved device design. The eccentric rotating mass source (a type of orbital vibrator) showed potential as a relatively powerful source, however this particular prototype lacked the functional control to needed to produce unique signals that could be used for travel time variation calculations so its comparative potential could not be established.

Other commercially available seismic sources, used in geophysical exploration, might also be considered, namely sparkers, orbital vibrators, vibroseis and airguns. The various source types have different advantages and disadvantages, all which need to be evaluated for the task of routine long term cave front tracking.

5.3.2 Stacking

Data stacking was an integral part of the piezoelectric source deployment for the purpose of mine front tracking. The amount of data stacked contributes to the attainable SNR, albeit with diminishing returns. How much data that can be stacked was determined by the signal generation rate and the total recording time between stacks. Signal generation rate is limited by the optimal duty cycle of the source device. For the SRX-1 source a conservative duty cycle of ~60 % was used, meaning pulse rate could be increased by as much as 50 % (4.5 shots per second). Total recording time between stacks would be limited by the desired regularity required for travel time variation measurements. Should reduced SNR become a concern then stacking periods or source fire rate could be increased to compensate accordingly.

5.3.3 Array Design

The number of seismic sensors required for cave back tracking would be determined by the desired spatial resolution, covering the cave back. A single source and sensor could be used create a rough estimate of the cave back position but would lack the ability to create a profile of the cave shape. To achieve this, multiple overlapping source and sensors ray-paths are required which cover the full extent of the cave foot print in a approximate grid pattern.

Most block cave mines mine relatively deep ore bodies with large vertical distribution (as much as 1 km), meaning that vertical growth of the cave might extend well beyond

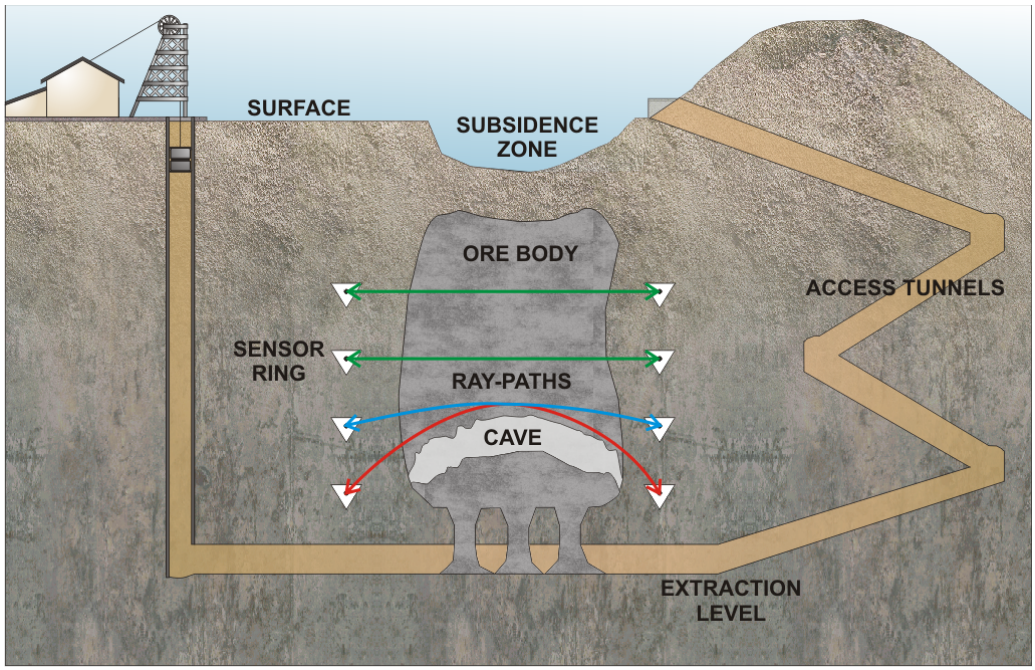

Figure 5.5: A cross-section illustration of an active seismic block cave tracking system. Multiple rings of sensors and active sources are positioned at varying depths in relation to the ore body for the purpose of tracking the cave back as it progresses upwards.

the potential range of the active sources employed in the array. A possible array design that could contend with this problem would use multiple levels or rings of sources and sensors positioned at different depths (Figures 5.5 and 5.6). An added benefit of a vertical distribution of sensors would be the ability to estimate the fracture state of the ore body above the cave back which would potentially aid the mining process by identifying regions that require fracture stimulation.

The type of sensors employed would depend on the type of active source employed in the array as well as the required sensitivity. Both the piezoelectric and pneumatic source generate high frequency signals which are better recorded by accelerometer type sensors due to the greater sensitivity to higher frequencies. Airgun and oscillatory sources operate at lower frequencies which make geophone type sensors the better option.

It should also be noted that an active seismic array would also perform the role of a passive microseismic monitoring array as the use of low power seismic sources relies on stacking for signal recovery. The source signal would not register as a passive seismic event due to the signal being weaker than or comparable to the noise and so makes it invisible to standard triggering algorithms. High power sources that fire relatively infrequently would make the array go deaf when a shot is fired but only for a very brief period ($<$ 1 millisecond), meaning it would be deaf for a very small duration on a daily basis (potentially a few seconds every day). A seismic monitoring system should know when the active source is operated and treat the data recorded during that period as such.

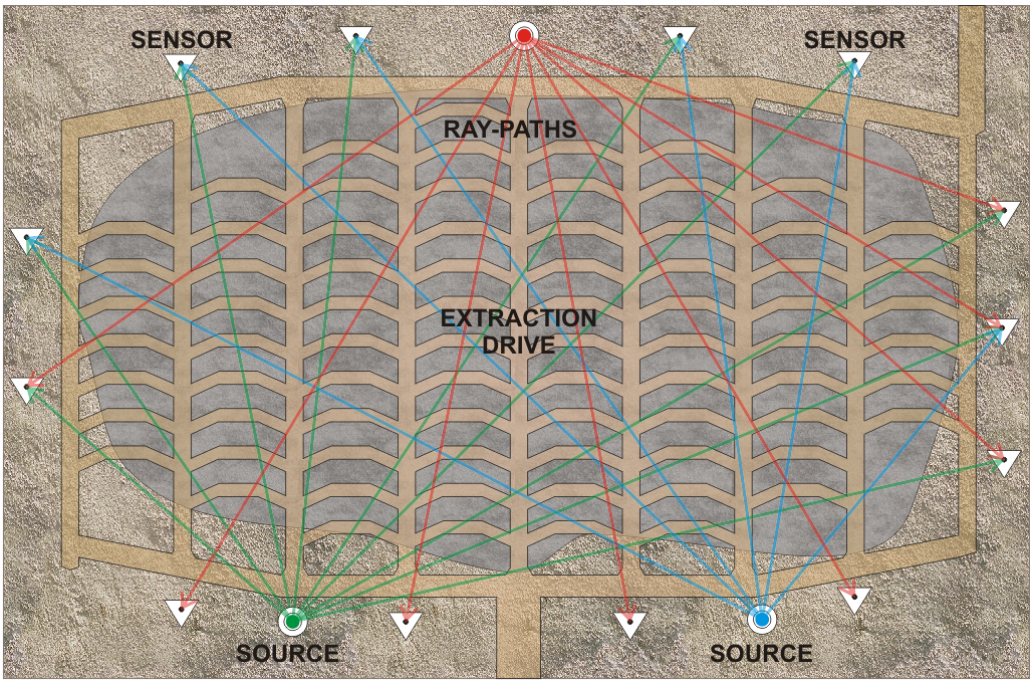

Figure 5.6: A plan view illustration of an active seismic source block cave tracking system. Seismic sensors are positioned around the ore body's anticipated caving region to form a ring. Depending on the requirements of the tracking system, one or more seismic sources are positioned along the ore body perimeter.

Chapter 6

Conclusion

An investigation was conducted to study the feasibility of using a small scale active seismic monitoring array to routinely study the progression of a cave back in a block cave mine. The investigation was carried out using two approaches, namely a small scale physical experiment in an underground mine and a numerical modeling investigation to study the signal behavior and travel time delay caused by mining away the rock mass.

6.1 Modelling

Dynamic wave and Fast Marching Method numerical modelling were employed to investigate the change in signal delay as sub-level mining progressed through the Halo 5205 Level, at Ridgeway Deeps Mine. The investigation aimed determine whether calculated phase delays could be used to invert for mining front progressions. The mining process was modelled using tunnel geometry and blasting information supplied by the mine in conjunction with estimations of the bulk and fractured properties of the region's rock medium. Signal travel times calculated using the Fast Marching Method were used to assess the accuracy of signal delays calculated using synthetic seismograms generated using E3D.

The dynamic wave modelling investigation highlighted several potential difficulties when employing time domain based waveform cross-correlation to measure signal delay changes larger than 1%. Signals interacting with complex and changing high impedance zones resulted in changes in the coda or latter portions of the synthetic waveforms. This limits the analysis to a small portion of the direct P-wave arrival for signal delay measurement using the methods discussed.

Significant ray bending caused by a change in medium geometry resulted in a change of the incident angle of the wave upon arriving at fixed sensor positions. This manifested as a rotation of the orthogonal components of the synthetic seismogram, which necessitates a measurement of the wave polarization angle using principle component analysis in order to rotate the seismograms to face the direction of the wave front.

Significant waveform stretching of synthetic wave waveforms, attributed to frequency dependent attenuation, also caused a detrimental effect on the time-domain based cross-correlation used to calculate signal delay change. This concern could not be avoided using the E3D modelling software and instead was handled using waveform contraction as a search parameter to counter-shrink the synthetic seismograms to better match the original reference waveform.

Small changes in the calculated waveforms occurred after each modelled mining advance step which accumulated into noticeable changes in the synthetic signal when comparing the first and last modelled mining steps. The complicated interactions of the

wave with the changing model geometry could not be fully corrected for and hindered the time-domain based phase-lag calculation process. This made the absolute reference scheme unsuitable for signal delay change measurement over the full progression of modelled mining. Instead a dynamic reference scheme was employed which made use of the previous modelled step set of synthetic seismograms as the reference, reducing the dissimilarity between the reference and the comparator waveforms and ensuring that only well correlated (> 0.85) waveforms were used.

Signal delays changes were calculated for each individual modelled sub-level mining advance step. Calculated delay increases for individual steps ranged between 0.02 ms to 0.136 ms. The overall delay between the first and last modelled steps ranged between to 3.3 ms to 7.5 ms.

A simple mining front estimation scheme was used which compared travel time variations calculated using the dynamic wave modelling to that of travel time differences calculated using Fast Marching Method. Correct mining front estimation was only possible with this method after void advance had reached the source-to-sensor ray-path intersection points. This was a limitation of the array configuration defined by the physical experiment.

Significant signal attenuation was also identified as an experimental concern and was largely attributed to the expansion of the seismic shadow cast by the advancing mining front which blocks the direct line-of-sight between source and sensor. Only the diffracted portion of the wave energy reaches the sensor positions, resulting in a greatly reduced signal amplitude.

6.2 Physical Experiment

A small scale active seismic experiment was conducted at Ridgeway Deeps Gold Mine. Installation and recording was started in October 2012 with the experiment concluding in June 2014. A piezoelectric transducer was employed as the active seismic source and an array of standard micro-seismic monitoring geophones were installed to monitor the controlled sub-level mining of the Halo 5205 Level. Extensive data stacking techniques were successfully employed to recover the weak seismic signal generated by the transducer, which in turn required an accurate zero-time reference measurement.

The signal recorded from a close proximity seismic sensor proved unreliable as a timing reference due to gradual changes in the recorded waveform (over several months) which were attributed to changing conditions in the seismic source's water filled borehole. The non-static reference signal introduced a significant decreasing trend in the signal delay histories measured from stacked seismic data. A correction was introduced using the recorded electromagnetic inference created by the high voltage drive signal for the piezoelectric transducer which served as a more stable zero-time reference. This interference signal was also used to establish a lower bound minimum phase-lag measurement resolution of 2 μs.

High accuracy measurements of signal travel time changes were attained using time domain based cross-correlation on stacked seismograms for all sensors. SNR values achieved after stacking varied significantly for all sensors over the recording period owing to the reliability of the recorded data. Large variations in background noise levels and occasional data loss caused by loss of communications and power to the experiment site reduced the amount of data that was considered suitable for stacking.

Sub-level cave mining ceased before the mining front had extended into the intercept of the source-to-sensor ray-paths. Despite this the experiment was sensitive enough to measure both the instantaneous increase in signal travel time following a ring blast (as much as 70 μs or 0.8 % signal delay change) and the post-relaxation that followed after-

wards. This specific co-seismic damage and medium healing response was also observed in signal delay histories calculated using seismic signals generated from a pneumatically powered seismic source which was operated in parallel with the piezoelectric source.

Similar medium velocity responses to co-seismic damage have been observed in past studies investigating the medium effect of underground blasting and large earthquakes as well as laboratory studies on rock samples. Observation of this medium blast response phenomenon confirms that the active seismic monitoring system was correctly measuring signal delays that resulted from changes in the seismic medium. Given the scenario where mining had advanced through the array's source-to-sensor ray paths then, based on delays calculated using numerical modelling, it would be reasonable to assume that the array was sensitive enough to measure permanent increases in signal delay that could be used to determine face advance.

Modelling results also suggested that significant signal attenuation, attributed to the effect of the growing seismic shadow, might have prevented accurate measurement of the very last mining advances in this scenario.

The blasts were performed at a rate that did not allow the measured post-relaxation process to converge to a steady baseline during the mining process. The largest permanent change in signal-delay was observed after the last blast was conducted, which measured a total delay increase of 70 μs or 0.8 %.

6.3 Application to Block Cave Mining

Information attained from both the numerical modelling and the sub-level cave tracking experiment provided insights into employing active seismic source technology to the problem of routinely tracking the cave back of a block cave mine. Numerical modelling revealed several problems with signal delay processing and signal attenuation following medium extraction. The physical experiment highlighted technical shortcomings and provided insight into the performance of a piezoelectric and pneumatically operated active seismic source in a working mine environment when employing techniques centered on extensive data stacking.

Collectively, the insights gained indicate that routine block cave tracking is certainly possible within the restraints of the typical mining environment, although development is still be required to better hone active sources with regards to the effective range and reliability. Specific dynamic wave modelling that incorporates realistic geometry of block cave mines should be conducted to better understand the evolution of active source signals interaction with different cave back shapes and further investigate the best signal analysis approaches.

The dimensions of block caves vary from mine to mine (150 - 500 m) making the effective range of an active source and the arrangement of the sensor array an important consideration. Many seismic source and receiver types are available that could possibly be employed for the task, however no specific recommendations can be made without a comprehensive analysis of all the different technologies.

As for the technology tested in this experiment, a SRX-1 acoustic projector type piezoelectric transducer, despite being a weak seismic source, proved to be extremely reliable and showed potential to achieve effective ranges required for a block cave tracking system by employing purpose built designs and the use of extensive data stacking. Various means were discussed on ensuring accurate time and further enhancing the range of piezoelectric source types.

The pneumatically operated impact source also showed great potential as an active seismic tool as field testing revealed the device's relatively strong signal power and excellent signal reproducibility. This makes it well suited for data stacking and it has the

potential for a long effective range (500 m), ideal for the purpose of cave back tracking. Mechanical reliability of the device remains unproven and further development and field testing is required before the device could be deployed for any long term routine analysis.

Both source types have the benefit of being relatively inexpensive while also having associated technology specifically developed for use with standard passive micro-seismic monitoring systems in a mine environment, making either a good starting point for block cave tracking systems.

Bibliography

[1] K. Aki and P. G. Richards. *Quantitative Seismology: Theory and Methods*, volume I. W. H. Freeman and Company, 1980.

[2] J. Bailey. Inquest into the deaths of R. Bodkin; M. House; S. Osman and C. Lloyd-Jones; on the 24th November, 1999 at the E26 Lift Mine North Parkes Mines, Parkes, New South Wales. Coroners report, Coroner, 2003.

[3] R. H. Bartels, J. B. C. Beatty, and B. A. Barsky. *An Introduction to Splines for Use in Computer Graphics and Geometric Modeling*. Morgan Kaufmann Publishers, 1987.

[4] Y. Ben-Zion and A. A. Allam. Seasonal Thermoelastic Strain and Postseismic Effects in Parkfield Borehole Dilatometers. *Earth and Planetary Science Letters*, 379:120–126, 2013.

[5] B. Bradie. *A Friendly Introduction to Numerical Analysis*. Pearson Education, 2006.

[6] F. Brenguier, M. Campillo, C. Hadziioannou, N. M. Shapiro, R. M. Nadeau, and E. Larose. Postseismic Relaxation Along the San Andreas Fault at Parkfield from Continuous Seismological Observations. *Science*, 321(5895):1478–1481, 2008.

[7] J. A. Bærentzen. On the implementation of fast marching method for 3D lattices. Technical Report 31-10-2001, Technical University of Denmark, 2001.

[8] W. C. Chew. *Waves and Fields in Inhomeneous Media*. IEEE Press, 2012.

[9] D. Clarke, L. Zaccarelli, N. M. Shapiro, and F. Brenguier. Assessment of resolution and accuracy of the moving window cross spectral technique for monitoring crustal temporal variations using ambient seismic noise. *Geophysical Journal International*, 186(2):867–882, 2011.

[10] Du Pont Company. *Blaster's Handbook*. E. I. du Pont de Nemours & Co. (Inc.), 16th edition, 1980.

[11] R. J. O' Connell and B. Budiansky. Seismic velocities in dry and saturated cracked solids. *Journal of Geophysical Research*, 79:5412–5426, 1974.

[12] J. K. Costain and C. Coruh. *Basic Theory in Reflection Seismology: with MATHEMATICA*. Elsevier, 2004.

[13] R. Courant, K. Friedrichs, and H. Lewy. On the partial difference equations of mathematical physics. *IBM Journal*, 11(2):215–234, 1967.

[14] G. J. Elbring. Comparison of lower-frequency (<1000 Hz) sownhole seismic source for use at environmental sites. Master's thesis, 2008.

[15] A. Fichtner. *Full Seismic Waveform Modelling and Inversion*. Springer, 2011.

[16] M. T. Galdwin. Simultaneous monitoring of stress and strain in massive rock. *Pageoph*, 115:265–274, 1977.

[17] J. D. Gibson. *The Communications Handbook*. CRC Press, 2002.

[18] T. H. W. Goebel, D. Schorlemmer, T. W. Becker, G. Dresen, and C. G. Sammis. Acoustic emissions document stress changes over many seismic cycles in stick-slip experiments. *Geophysical Research Letters*, 40:2049–2054, 2013.

[19] M. T. Green and R. A. Lynch. Self funded research program: Borehole seismic source. Technical report, Integrated Seismic Systems, 2009.

[20] R. W. E. Green. ISSI piezoelectric source driver. Letter, Private, 2013.

[21] C. Hadziioannou, E. Larose, O. Coutant, P. Roux, and M. Campillo. Stability of monitoring weak changes in multiply scattering media with ambient noise correlation: Laboratory experiments. *The Journal of the Acoustical Society of America*, 125:3688, April 2009.

[22] P. A. Johnson, J. Carmeliet, H. Savage, M. Scuderi, B. Carpenter, R. A. Guyer, and C. Marone. Dynamically triggered slip and substained fault gouge metastability under laboratory shear conditions. *Geophyical Research Letters*, 40:1–5, 2013.

[23] S. L. Klemperer. Seismic noise-reduction techniques for use with vertical stacking, an empirical comparison. *Society of Exploration Geophysicists*, 52(3):322–334, 1987.

[24] V. Lakshminarayanan, A. K. Ghatak, and K. Thyagarajan. *Lagrangian Optics*. Kluwer Academic Publishers, 2002. Appendix A: Geometric optics approximation and the eikonal equation.

[25] S. Larsen. *E3D: 2D/3D elastic finite-difference wave propergation code*. Lawrence Livermore National Laboratory, 1992.

[26] T. Lay and T. C. Wallace. *Moden Global Seismology*. Academic Press, 1995.

[27] P. C. Leary, P. E. Malin, R. A. Phinney, T. Borcher, and R. VonColln. Systematic Monitoring of Millisecond Travel Time Variations Near Palmdale, California. *American Geophysical Union*, 84(B2):659–665, Febuary 1979.

[28] P. C. Leary and L. A. Walter. Physical model for the downhole orbital vibrator (DOV) - I. Acoustic and borehole seismic radiation. *Geophysics Journal International*, 163(2):647–662, 2005.

[29] A. R. Levander. Fourth-order finite-difference P-SV seismograms. *Geophysics*, 53(11):1425–1436, November 1988.

[30] W. Lowrie. *Fundamentals of Geophysics*. Cambridge University Press, 2nd edition, 2007.

[31] R. A. Lynch. Passive and active seismic monitoring in mines. In *5th Deep And High Stress Mining Seminar, Chile, 6 - 8 Oct 2010*, Keynote Address, October 2010. ISS International.

[32] R. A. Lynch. Active seismic monitoring, 2012.

[33] R. A. Lynch and E. C. Lötter. Estimation of cave geometry using a constrained velocity model inversion with passive seismic data. *The Journal of The Southern African Institute of Mining and Metallurgy*, 107(12):791–796, December 2007.

[34] R. A. Lynch, G. Olivier, and M. T. Green. High accuracy measurements of seismic velocity variation in mines. *RaSim*, 8:157–164, 2013.

[35] R. Madariaga, K. Olsen, , and R. Archuleta. Modeling dynamic rupture in a 3D earthquake fault model. *Bulletin of the Seismological Society of America*, 88(5):1182–1197, October 1998.

[36] A. J. Mendecki. *Seismic Monitoring in Mines*. Chapman and Hill, 1997.

[37] F. Niu, P. G. Silver, T. M. Daley, X. Cheng, and E. L. Majer. Preseismic velocity changes observed from active source monitoring at the Parkfields SAFOD drill site. *Nature*, 454:204–208, July 2008.

[38] G. Olivier. *Seismic imaging and monitoring in mines with ambient seismic noise correlations*. PhD thesis, 2015.

[39] G. L. Pollack and D. R. Stump. *Electromagnetism*. Addison Wesley, 2002.

[40] J.G. Proakis and D. G. Manolakis. *Digital Signal Processing. Principles, Algorithms, and Applications*. Prentice Hall, 1996.

[41] P. Reasenberg and K. Aki. A precise, continuous measurement of seismic velocity for monitoring in situ stress. *American Geophysical Union*, 79:399–405, 1974.

[42] H. Ryan. Ricker, Ormsby, Klauder, Butterworth - A choice of wavelets. Technical report, Hi-Res Geoconsulting, 1994.

[43] R. L. Sengbush. *Seismic Exploration Methods*. Springer Science & Business Media, 2012.

[44] J. A. Sethian and A. M. Popovici. 3-D traveltime computation using the fast marching method. *Geophysics*, 64(2):516–523, March 1999.

[45] P. G. Silver, T. M. Daley, F. Niu, and E. L. Majer. Active source monitoring of cross-well seismic travel time for stress-induced changes. *Bulletin of the Seismological Society of America*, 97(1B):281–293, February 2007.

[46] R. Snieder. The theory of coda wave interferometry. Technical report, Center for Wave Phenomena, 2005.

[47] J. Virieux. P-SV wave propagation in heterogeneous media: Velocity-stress finite-difference method. *Geophysics*, 51(4):889–901, April 1986.

[48] J. Virieux, V. Etienne, and V. Cruz-Atienza. Modelling seismic wave propagation for geophysical imaging. Technical report, Intechopen, 2008.

[49] Z. Yao and G. F. Margrave. Fourth-order finite-difference scheme for P and SV waves propagating in 2D transversely isotropic media. Research Report 11, Consortium for Research in Elastic Wave Exploration Seismology, 1999.

Appendix A

IMS Hardware

IMS seismic hardware specifications documentation for equipment used in the experiment.

1. 10 kHz accelerometer sensor.
2. 2.3 kHz accelerometer sensor.
3. 14 Hz geophone sensor.
4. 28 Hz geophone sensor.
5. netADC8 networked seismic digitizer.
6. Piezoelectric source driver.
7. 1-Port DSL modem.
8. GPS timing unit.
9. Time distributor unit.

Sensor 10 kHz Accelerometer

Borehole Sonde

institute of mine seismology

Characteristics of IMS 10 kHz Accelerometers

Sensor

Frequency range	1.0 - 10000 Hz
Dynamic range	114 dB [1]
Linear output range	± 15 g
Noise	30 μg_{rms}
Sensitivity	0.500 V/g
Input voltage	18 - 30 VDC [2]
Input current	2 - 10 mA [2]
Shock limit	2500 g

Physical (for sonde)[3]

Diameter	34 mm
Length	185 mm
Mass	0.5 kg

Installation

Working position	omni-directional
Diameter	76 mm
Pressure tested water depth	600 m

1 Measured using a 2.5 - 25 000 Hz bandwidth

2 Powered with IMS IEPE accelerometer line driver

3 Physical dimensions are given for the most commonly used borehole sonde. Different sonde sizes may be available. Refer to IMS document entitled “Seismic sensor products” for details of common sensor sizes.

IMS-SPEC-ACC10kBOREHOLE-20130524-MGv0

Sensor 14 Hz Geophones

Borehole Sensor

institute of mine seismology

Characteristics of IMS 14 Hz geophones

Sensor

Frequency range (±3dB)	6 Hz - 2000 Hz
Natural frequency	14 Hz ± 0.5 Hz
Distortion with 18 mm/s p.p coil to case velocity	< 0.3 %
Distortion measurement frequency	14 Hz
Open circuit damping	0.185 ± 5 %
Standard coil resistance	3500 Ω ± 5 %
Open circuit sensitivity	80.0 V/m/s ± 5 %
Damped (0.7) sensitivity	56.1 V/m/s ± 5 %
Moving mass	10.2 g
Maximum coil excursion	0.5 mm

Physical (for sonde)[1]

Diameter	51 mm
Length	300 mm
Mass	1.3 kg

Installation

Working position	omi-directional
Minimum hole diameter	76 mm
Pressure tested water depth[2]	400 m

1 Physical dimensions are given for the most commonly used borehole sonde. Different sonde sizes may be available. Refer to IMS document entitled “Seismic sensor products” for details of common sensor sizes.

2 High pressure rated sensors (up to 2000 m depth) available on request.

IMS-SPEC-GEO14BOREHOLE-20130430-MGv0

netADC

Seismological Digitizer

institute of mine seismology

Key Features

- Small, lightweight, 35 mm DIN rail mountable enclosure with UL94 V0 flame retardant rating
- Low power: 0.38 Watt per channel [1]
- Power over Ethernet capable [2]
- 4 or 8 seismic sensor channels
- Geophone, Broadband, Force Balance or Piezoelectric digitizer
- Timing, power and data over single CAT5 cable (if using IMS WoE switch)
- Multi-station Networked, or Standalone operating modes
- Compatible with Smart Seismic Sensors (self-configuring)
- Wide dynamic range (24-bit oversample data)
- Software selectable sampling rates
- Continuous streaming of data (triggered recording with netSP)
- Communications (Waveforms over Ethernet) via 10/100Base-Tx Ethernet or fibre (using external media converter)
- Geophone state-of-health coil measurements
- Remotely upgradable firmware via netSP and/or Synapse
- On-board temperature measurement and readout

Specifications

ADC CHARACTERISTICS
- Seismic Channels .....4 or 8
- Sampling Rates [3].....1 to 192000 Hz

Bandwidth
- 0 - 48000 Hz.....0.47 fs
- 48000 - 92000.....0.45 fs
- 92000 - 192000.....0.24 fs

Dynamic Range [4]
- @ 48000 .....118 dB
- @ 50 .....147 dB

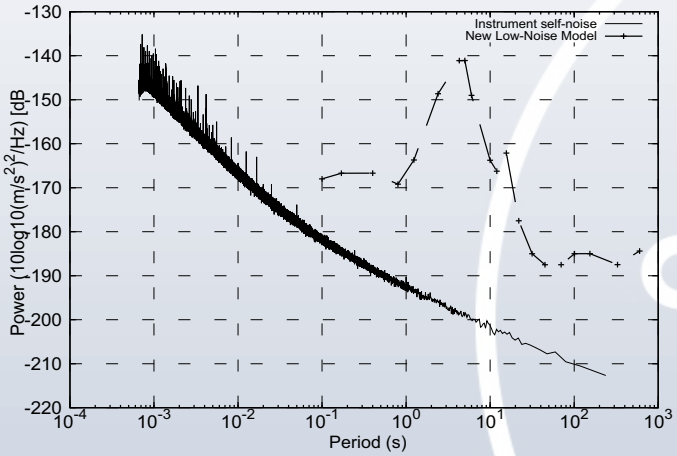

ELECTRICAL
- Supply Voltage ..... 9 - 18 Vdc
- Power Consumption [1].....3 W

PHYSICAL
- Mass ..... 420 g
- Dimensions:
  - Height.....180 mm
  - Width.....52 mm
  - Depth.....165 mm

ENVIRONMENT [5]
- Operating Temperature.....-10 - 70°C
- Humidity..... 20 - 80 % relative humidity, non-condensing

EXTERNAL INTERFACES
- Ethernet (10/100Base-TX) with Auto-MDIX (auto-crossover) and 802.3af PD functionality for power, setup and telemetry
- RS-232 (3-wire) port for time synchronization
- DC power and feed-through
- 4 or 8 seismic sensor channels (geophone, broadband, piezoelectric & FBA)
- 6 user LEDs
- 2 User push buttons

NOTES:

[1] Average power consumption measured on 8 channel version, at 48 kHz sample rate, continuously streaming data over 100Base-TX interface.

[2] Power over Ethernet (PoE) functionality must be specifically requested at order time. Delivery time for PoE capable devices is subject to availability and manufacturing leadtimes.

[3] Software selectable: 1, 3, 5, 10, 15, 20, 50, 75, 100, 125, 150, 200, 250, 300, 500, 750, 1000, 1500, 3000, 6000, 12000, 24000, 48000, 96000, 192000 Hz.

[4] Dynamic range dependent on sampling rate due to oversampling

[5] This device is not designed to be operated in an un-enclosed environment. To avoid voiding of equipment warranty, the equipment must be housed in an external enclosure. The external enclosure should have an Ingress Protection Rating of at least IP65. Suitable, customised, pre-wired enclosures are available from IMS upon request.

IMS-SPEC-NETADC-20140919-MGv3

Piezoelectric Source Driver

Signal Generator for Piezoelectric Seismic Sources

institute of mine seismology

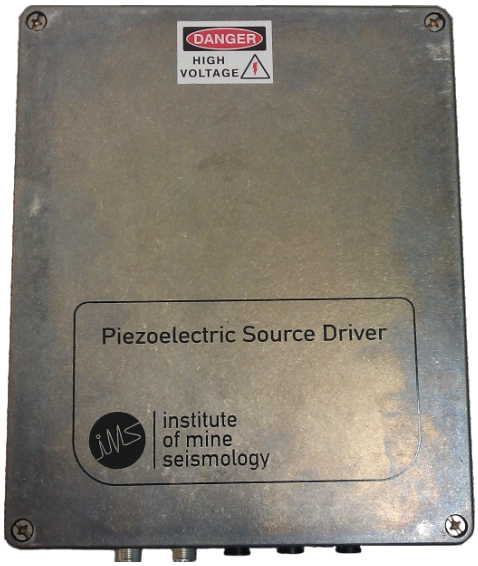

Key Features

- Robust aluminium enclosure with IP66 ingress rating
- 1.4 kV_{p-p} driving signal output
- Ricker Wavelet pulse generation with programmable frequency
- Programmable pulse generation rate
- Pulse-Per-Second time synchronization
- RS232 communications for status monitoring and remote programming
- Internal temperature and pressure sensor
- 2 status LEDs

Specifications

ELECTRICAL

Voltage requirement .....12 V DC

Average power consumption .....6 W

Output voltage .....1.4 kV_{p-p}

EXTERNAL INTERFACES

2 UHF connectors for output signal

12 V DC 5 pin connector

1 RS232 serial communications port for status monitoring and remote programming

1 ATU port for time synchronization

PHYSICAL:

Mass.....4.3 kg

Dimensions:

Length .....230 mm

Width .....230 mm

Depth .....110 mm

ENVIRONMENT:[1]

Operating Temperature..... 0 - 50°C

1 To avoid voiding of equipment warranty, the external enclosure should have an Ingress Protection Rating of at least IP65. Suitable, customised, pre-wired enclosures are available from IMS upon request.

DSL-1Port

Single Port DSL Modem

institute of mine seismology

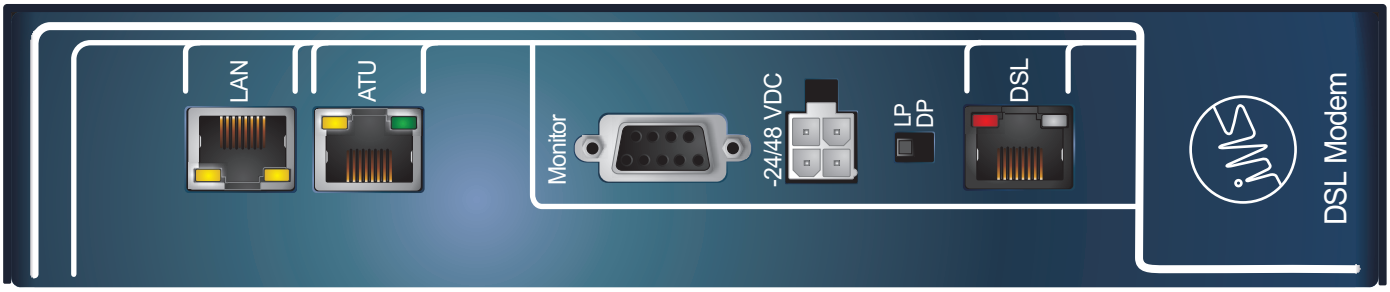

Key Features

- Timing over DSL link (no additional lines required)
- SHDSL and SHDSL.bis (TC-PAM16/32)
- Up to 5.7Mbps over single pair copper
- Ethernet Bridge (10/100BaseT)
- Repeater/Regenerator Support
- Console Port, Telnet, Web, SNMP Management
- 35 mm din rail mounting
- Point-to-Point

Interfaces

xDSL LINE INTERFACE

- Specification ITU-T G.991.2-G.shdsl, ITU-T G.991.2-G.shdsl.bis
- Modulation TC-PAM16/TC-PAM32
- Impedance 135 Ω
- Transmit Power 13.5 (Annex A) or 14.5 (Annex B) dBm @ 135 Ω
- Number of Pairs 1
- Bit Rate 192 to 5704 kbps
- Connector Type RJ-45, 8 pin
- Overvoltage Protection ITU-T Rec. K.20/K.21
- Wetting Current 2-4 mA @ 60 V

MONITOR INTERFACE

- Specification EIA-232 / V.28
- Data Rate 9600 baud, asynchronous
- Protocol 8 bit, no parity, 1 stop bit, no linefeed with carriage return, XON/XOFF enabled
- Signal Level V.28 on DB9 female connector
- Connector Type DB9 female connector

ETHERNET INTERFACE

- Standard: IEEE-802.3, IEE-802.1Q
- Data Rate 10/100BaseT, Full/Half Duplex
- Protocol Telnet, SNMP
- Signal Level Ethernet
- MDI / MDI-X auto crossover supported
- Auto Negotiation supported
- Connector Type RJ45 (1x)

Specificatons

ELECTRICAL

Specification ETSI ETS 300 132-2
Supply voltage.....24/48 V DC
Power consumption.....4.0 W

SAFETY / EMC

IEC 60950-1:2005
EN 60950-1:2006
EN 55022, Class B
EN 300386
EN 50121-4

PHYSICAL

Weight.....0.96 kg
Dimensions
Height.....217 mm
Width.....43 mm
Depth.....162 mm

Specification subject to change without prior notice. Refer to http://www.imsesimology.org/notices for important information about equipment installation and warranty conditions, as well as the most recent product specifications.

NOTES

To avoid void of equipment warranty, the external enclosure should have an Ingress Protection Rating of at least Ip65. Suitable, customised, pre-wired enclosures are available from IMS upon request

Time Distributor

For Time Synchronisation of IMS Stations over Ethernet

institute of mine seismology

Key Features

- Small, lightweight metal enclosure
- Multi-purpose, 19-inch rack (1U) or desk mounting brackets supplied
- Universal AC input
- 4-way Analogue Time Update (ATU) signal fanout
- Cascadable ATU inputs and outputs for large systems
- Optional GPS module for timing signal generation [1]
- On-board RTC can be used as time source for underground applications
- All connections on front panel for easy rack mount access
- DIP switch adjustable ATU signal generation period: 1 second, 1, 2 or 5 minutes
- Separated port for NMEA messages and GPS pulse per second (PPS)

Specifications

ELECTRICAL

INPUT (AC):
- Phase .....single phase and PE
- Line voltage .....100 - 260 V AC[2]
- Line frequency .....50 - 60 Hz

PHYSICAL

- Mass[3].....350 g
- Dimensions:
  - Height .....144 mm
  - Width .....245 mm
  - Depth .....82 mm

ENVIRONMENT[4]

- Operating Temperature .....-15 - 80 °C
- Humidity .....20 - 80 % relative humidity, non-condensing

EXTERNAL INTERFACES

Mains line power inlet: universal IEC EN60320 C14 connector with removable fuse

ATU input port: RJ45 jack

4 ATU output ports: RJ45 jacks

DIP switches for ATU generation settings

4 user LEDS: Power, GPS, GPS fix status and ATU generation

Female SMA connector for GPS antenna[1]

NMEA output port for GPS NMEA messages and PPS or RTC time messages

NOTES

1 Internal GPS module must be specified at time of order. With no internal GPS module, SMA connector is not fitted.

2 12 V DC version available by special order.

3 Weight without mounting brackets or accessories.

4 If the unit is to be installed in an underground or other harsh environment, then to avoid voiding of equipment warranty, an external enclosure with an Ingress Protection Rating of at least IP65 should be provided. Suitable, customised, pre-wired enclosures are available from IMS upon request.

IMS-SPEC-TDU-20111215-MGv1

Appendix B

Monitoring Channel Map

Seismic monitoring details from the physical experiment that link recording channels with the various sensors and their axial components.

No.	netADC No.	Channel No.	Sensor	Axial Component
1	1	1	1UG	X
2	1	2	1UG	Y
3	1	3	1UG	Z
4	1	4	R1G	Z
5	1	5	R2A	Z
6	1	6	L1A	X
7	1	7	L1A	Y
8	1	8	L1A	Z
9	2	1	D3G	X
10	2	2	D3G	Y
11	2	3	D3G	Z
12	2	4	D2G	X
13	2	5	D2G	Y
14	2	6	D2G	Z
15	2	7	D1G	X
16	2	8	D1G	Z
17	3	1	L4G	Y
18	3	2	L4G	Z
19	3	3	L5G	Y
20	3	4	L5G	Z
21	3	5	L2G	X
22	3	6	L2G	Y
23	3	7	L3G	Y
24	3	8	L3G	Z

Table B.1: A table listing the seismic recording channels and the sensors used in the physical experiment. There were more sensors components than there were recording channels available. Sensors components which recorded poor signal-to-noise ratios were dropped in favor of sensors components that performed better.

Appendix C

Cubic Spline Interpolation

The purpose of an interpolation function is the inter sample approximation of a discretized function such as a recorded seismogram. Cubic spline interpolation is such a method which is continuous in both the first and second derivatives [3], making it suitable for interpolating waveforms which can be described by the wave equation. Consider a given set of $N+1$ number of ordered pair points $[x_i, y_i]$ with $i = 0, 1, 2, ..., N$ and therefore N number of intervals. The i^{th} cubic spline segment that interpolates between the two consecutive points at x_i and x_{i+1} can defined by the cubic function:

$$F_i(t) = a_i t^3 + b_i t^2 + c_i t + d_i \tag{C.1}$$

with the parameter t is defined as

$$t = \frac{x - x_i}{x_{i+1} - x_i} \quad t \in [0, 1] \tag{C.2}$$

Equation C.1 presents 4 unknowns, namely the coefficients of the four terms in the polynomial a_i, b_i, c_i and d_i. As there is a cubic spline segment for each of the N number of intervals, it means there are $4N$ number of unknowns, requiring $4N$ knowns or conditions in order for solve for all unknowns.

The first requirement of the interpolating function is that it passes through all the given tabulated points, so segment $F_i(t)$ is constrained by it's two bounding points $[x_i, y_i]$ and $[x_{i+1}, y_{i+1}]$, namely:

$$F(t(x_i)) = F_i(0) = y_i \tag{C.3}$$
$$F(t(x_{i+1})) = F_i(1) = y_{i+1} \tag{C.4}$$

Equations C.3 and C.4 provide two knows per spline segment or two $2N$ conditions, meaning an additional $2N$ are still required.

The second defining constraint is the requirement that the first and second derivatives of the segments, passing through interior points, are smooth and continuous at each bounding point. The condition is expressed by the following:

$$F'_{i-1}(1) = F'_i(0) \tag{C.5}$$
$$F''_{i-1}(1) = F''_i(0) \tag{C.6}$$

The first and second derivative of each spline segment is:

$$F'_i(t) = 3a_i t^2 + 2b_i t + c_i \tag{C.7}$$
$$F''_i(t) = 6a_i t + 2b_i \tag{C.8}$$

Substituting the segment boundary values into first derivative and introducing k_i, where k_i is the first derivate or gradient at the given tabulated points:

$$F_i^{'}(0) = \quad k_i \quad = c_i \tag{C.9}$$
$$F_i^{'}(1) = \quad k_{i+1} \quad = 3a_i + 2b_i + c_i \tag{C.10}$$

For the second derivative, relation C.8 into C.6 gives:

$$6a_{i-1} + 2b_{i-1} = 2b_i \tag{C.11}$$

Using equations C.3 through to C.10 and solving for the cubic segment's coefficients, gives the following set of partial solutions with respect to k_i:

$$\begin{aligned} a_i &= k_i + k_{i+1} + 2(y_i - y_{i+1}) \\ b_i &= 3(y_{i+1} - y_i) - 2k_i - k_{i+1} \\ c_i &= k_i \\ d_i &= y_i \end{aligned} \tag{C.12}$$

The continuous requirement only applies to interior segments and so add an extra $2N - 2$ conditions, meaning an additional two conditions are still required in order to solve for the $4N$ unknowns.

The third constraint applied is the requirement that the gradient passing through the end points of the set is constant (known as a natural spline constraint), i.e.:

$$F_0^{''}(x_0) = 0 \tag{C.13}$$
$$F_N^{''}(x_N) = 0 \tag{C.14}$$

This set of solutions in C.12 are given in terms of the derivative k_i which must still be solved for in order to attain the desired cubic spline coefficients a_i, b_i, c_i and d_i. To achieve this, a linear combination of the equations involving all spline segments is required in order to solve for all k_i.

Combining equation C.11 with the partial solution for a_i and b_i from C.12 for internal segments gives:

$$6[k_{i-1} + k_i + 2(y_{i-1} - y_i)] + 2[3(y_i - y_{i-1}) - 2k_{i-1} - k_i] = 2[3(y_{i+1} - y_i) - 2k_i - k_{i+1}]$$

Simplifying and separating the terms leads to:

$$k_{i-1} + 4k_i + k_{i+1} = 3(y_{i+1} - y_{i-1}) \tag{C.15}$$

Similarly for the first and last segments using equations C.13 and C.14:

$$\begin{aligned} 2k_0 + k_1 &= 3(y_1 - y_0) \\ k_{N-1} + 2k_N &= 3(y_N - y_{N-1}) \end{aligned} \tag{C.16}$$

Equations C.15 and C.16 express all unknown k_i in terms of the given knowns y_i, which can be assembled into a tridiagonal matrix.

$$\begin{bmatrix} 2 & 1 & & \cdots & & \\ 1 & 4 & 1 & & & \\ & 1 & 4 & 1 & & \\ \vdots & & \ddots & \ddots & \ddots & \\ & & & 1 & 4 & 1 \\ & & & & 1 & 2 \end{bmatrix} \begin{bmatrix} k_o \\ k_1 \\ k_2 \\ \vdots \\ k_{n-1} \\ k_n \end{bmatrix} = \begin{bmatrix} 3\left(y_1 - y_0\right) \\ 3\left(y_2 - y_0\right) \\ 3\left(y_3 - y_1\right) \\ \vdots \\ 3\left(y_n - y_{n-2}\right) \\ 3\left(y_n - y_{n-1}\right) \end{bmatrix}$$

Solving for all k_i and substituting back into the partial solutions C.12 will provide the value of the coefficients of all the cubic spline segments that interpolate between the $N+1$ given data points $[x_i, y_i]$. Interpolate values along the respective segments are calculated using equations C.1 and C.2.

Appendix D

The Eikonal Approximation

The wave equation is a second order partial differential equation which describes the behavior of waves [26, 8]. The wave equation in three-dimensional space and time is expressed in terms of the displacement u:

$$\frac{\partial^2 u}{\partial t^2} = \bar{c}^2 \nabla^2 u \tag{D.1}$$

where:

- Displacement u is a function of spacial coordinates $\bar{x}$ and time t, $u = u(x, y, z, t)$.
- c is the velocity of the wave. In a non-isotropic heterogeneous medium the velocity is spatially dependent so $\bar{c} = (c_x, c_y, c_z)$.
- ∇^2 is the spatial Laplacian in Cartesian coordinates, $\left(\frac{\partial^2}{\partial x^2}, \frac{\partial^2}{\partial y^2}, \frac{\partial^2}{\partial z^2}\right)$.

The Eikonal approximation of the wave reduces the complexity of this second order differential by using an optical ray approach to determine wave propagation. In this form the wave is treated as an advancing front or plane wave. The motion of the wave is perpendicular to the plane of the wave at all points along the wave front and the wave length is much smaller than other length considerations.

To reach the Eikonal Equation, consider the d'Alembert's solution to the spatial wave equation [39, 24]:

$$u(\bar{x}, t) = A_0(\bar{x}) e^{-i(\bar{k}\bar{x} - \omega t)}$$

where:

- $A_0(\bar{x})$ is the initial displacement.
- ω is the angular frequency of the wave, $\omega = 2\pi f$.
- Wave number $\bar{k}$ is related to the slowness of the wave medium, $\bar{k} = (\frac{\omega}{c_x}, \frac{\omega}{c_y}, \frac{\omega}{c_z})$.

This solution can be restated in terms of wave front travel time $T(\bar{x}) = (\bar{k}\bar{x} - t)$, which links all points of equal travel time, in a similar fashion to contouring :

$$u(\bar{x}, t) = A(\bar{x}) e^{-i\omega T(\bar{x})} \tag{D.2}$$

Inserting this solution back into the wave equation D.1:

$$\begin{aligned}
\frac{\partial^2}{\partial t^2}\left(Ae^{-i\omega T(\bar{x})}\right) &= c^2\nabla\left(\nabla Ae^{-i\omega T} - i\omega A\nabla Te^{-i\omega T}\right) \\
\left(-\omega^2 A\right)e^{-i\omega T(\bar{x})} &= c^2\left(\nabla^2 A - \omega^2 A|\nabla T|^2 - i(2\omega\nabla A\cdot\nabla T + \omega A\nabla^2 T)\right)e^{-i\omega T} \\
-A\frac{\omega^2}{c^2} &= \nabla^2 A - \omega^2 A|\nabla T|^2 - i\omega(2\nabla A\cdot\nabla T + A\nabla^2 T) \qquad \text{(D.3)}
\end{aligned}$$

For information on the wave propagation consider only the real part of the right-hand side of equation D.3, $\nabla^2 A - \omega^2 A|\nabla T|^2$:

$$\begin{aligned}
-A\frac{\omega^2}{c^2} &= \nabla^2 A - \omega^2 A|\nabla T|^2 \\
|\nabla T|^2 - \frac{1}{c^2} &= -\frac{\nabla^2 A}{A\omega^2}
\end{aligned}$$

Apply a high frequency condition for the wave where sufficiently high ω causes the right-hand side of the equation to go to zero, which results in the Eikonal approximation:

$$\begin{aligned}
|\nabla T|^2 &= \frac{1}{\bar{c}^2} \\
|\nabla T| &= \frac{1}{\bar{c}}
\end{aligned}$$

It should be noted that no fixed rules exist to qualify the requirement for what makes ω sufficiently large enough to ensure the Eikonal equation remains a valid approximation of the wave equation. There are however general conditions which applies to optical rays in general which should be taken into consideration :

- The distance over which the medium wave speed changes, along any given ray path, must be much larger than the wavelength of the wave.
- The curvature of any given ray ($|\nabla T|$) should be relatively small compared to the wavelength of the wave.

Appendix E

Fast Marching Method

E.1 Computation Algorithm

A common analogy used to describe the process of FMM is that of a ring of fire that is burning through a medium. As the fire expands, it leaves behind burnt or spent medium that cannot be revisited (as there is nothing left to burn), meaning the fire can only spread into unburnt parts of the medium. Translating this to the Fast Marching Method, the fire is the wavefront which only spreads outwards, the burnt areas are grid points for which the travel time is calculated while the unburnt points have yet to be reached (Figure E.1).

Through this analogy, three states can be defined for the points:

- Burnt: Points with travel times that are known or already calculated and cannot be revisited. Burnt points that neighbor on active points are be used to evaluate active points.
- Unburnt: Points have no travel time information and have yet to visited for evaluation. Unburnt points cannot be used in a travel time calculation.
- Active: Points that comprise the wave front and are currently subject to evaluation. These points may possess a partial calculation of travel time and may be revisited until considered burnt. An active point is considered burnt when it is removed from the process queue.

Before any wavefront expansion can be calculated an initial condition of burnt points is required that defines the starting shape of the wavefront. This can be a single burnt point with a starting time $T = 0$ (spherical wave propagation in homogeneous medium) or any number of points that define an arbitrary shape. The initial condition points are considered burnt as only burnt points can be used to evaluate any active points.

The active points are identified by simply checking whether every starting burnt point has a neighbor in the x, y and z directions which is unburnt. These unburnt points are then marked as active, evaluated using the starting burnt points by following the calculation method defined in 3.3 and placed into a first-in-first-out queue.

The queue is sorted in ascending order of travel time values, every time an active point has been evaluated. The first active point in the queue (point with the smallest travel value) is taken out and marked as burnt. After burning the point, its position is now used to identify whether it has any unburnt neighbors (including active points) which are then evaluated for travel time and added to the queue which is again sorted.

Once the neighboring points have been added to the active point queue, the fist point in the queue is removed and marked as burnt and so the process continues until the active queue is emptied or a special stop condition is reached.

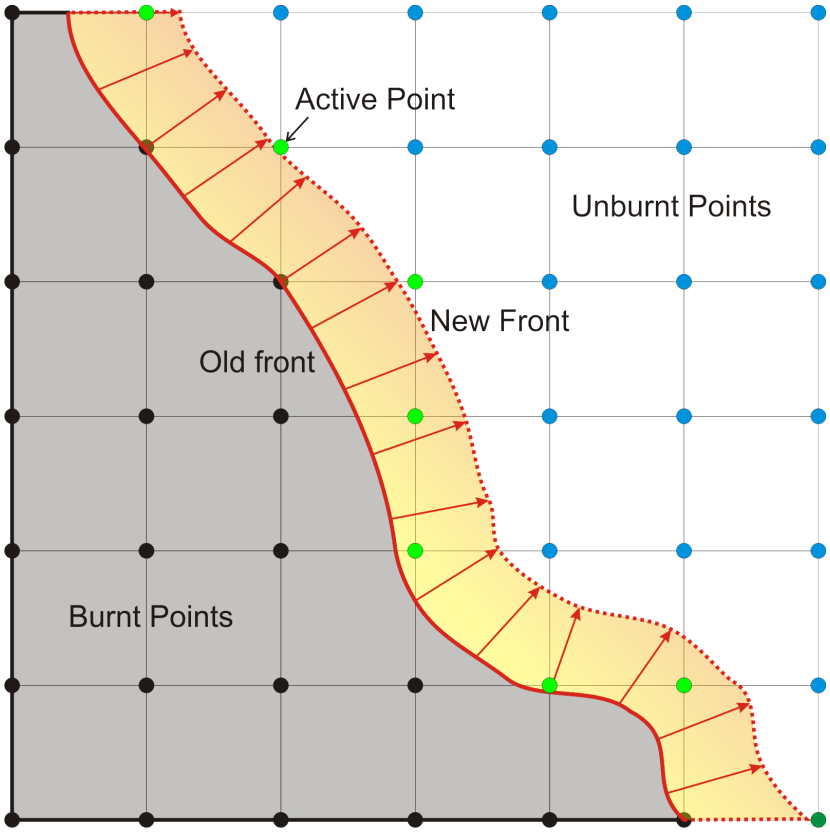

Figure E.1: A depiction of a 2-D Fast Marching Method grid, illustrating the different regions of the process. The wave front projects outward from the burnt region, represented by a contour of active points that outline the burnt region. Active points are added by determining whether the most recently burnt point has neighbors that are unburnt.

Because the neighbors of the most recently burnt points are considered for evaluation, it is possible that an active point already in the queue, can be evaluated again. The newly burnt point provides additional information for the evaluation of that active point, improving its the evaluated travel time.

The number of calculations on grid points is kept to a minimum in FMM however a great deal of computation goes into ensuring that the active points queue is sorted - a problem which grows as the size of the active queue grows. There are a number of computational methods which can efficiently sort queues of this nature.

Alternatively it could more efficient to insert the new point to its correct ascending position in the queue using a binary search algorithm or efficient indexing method instead of sorting the queue after each new member is added. An efficient search algorithm is also required in order to determine whether a currently evaluated neighbor point is an active point already present in the queue. If it is, it must be removed from the queue and inserted at its updated position in the queue.

Appendix F

Numerical Modelling Tests

F.1 Sensor Positions

Sensor	X	Y	Z
1	20.0	80.0	40.0
2	30.0	80.0	45.0
3	40.0	80.0	50.0
4	50.0	80.0	55.0
5	60.0	80.0	60.0
6	70.0	80.0	65.0
7	80.0	80.0	70.0
8	90.0	80.0	75.0
9	100.0	80.0	80.0
10	20.0	80.0	60.0
11	30.0	82.5	60.0
12	40.0	85.0	60.0
13	50.0	87.5	60.0
14	60.0	90.0	60.0
15	70.0	92.5	60.0
16	80.0	95.0	60.0
17	90.0	97.5	60.0
18	100.0	100.0	60.0

Source	X	Y	Z
1	60.0	20.0	60.0

Table F.1: The sensor and source positions used in the numerical modelling test cases which compares signal travel times calculated by E3D and the Fast March Method.

F.2 Test Case 1 Results

Sensor	Analytic	E3D	E3D Error		FMM	FMM Error	
No.	(ms)	(ms)	(ms)	(%)	(ms)	(ms)	(%)
1	14.96	15.64	0.67	4.5	15.01	0.04	0.3
2	13.75	14.42	0.67	4.9	13.79	0.04	0.3
3	12.81	13.48	0.67	5.3	12.84	0.03	0.3
4	12.20	12.88	0.67	5.5	12.23	0.02	0.2
5	12.00	12.68	0.68	5.7	12.00	0.00	0.0
6	12.20	12.88	0.67	5.5	12.23	0.02	0.2
7	12.80	13.48	0.67	5.3	12.84	0.03	0.3
8	13.74	14.42	0.67	4.9	13.79	0.04	0.3
9	14.96	15.64	0.67	4.5	15.01	0.04	0.3
10	14.42	15.08	0.66	4.6	14.44	0.02	0.2
11	13.86	14.54	0.67	4.9	13.89	0.02	0.2
12	13.60	14.28	0.68	5.0	13.62	0.02	0.1
13	13.65	14.32	0.67	4.9	13.66	0.01	0.1
14	14.00	14.68	0.68	4.9	14.00	0.00	0.0
15	14.64	15.32	0.68	4.7	14.65	0.01	0.1
16	15.52	16.20	0.68	4.4	15.54	0.02	0.1
17	16.62	17.30	0.68	4.1	16.64	0.02	0.1
18	17.88	18.56	0.67	3.8	17.91	0.02	0.1

Table F.2: Comparison of the results for the first signal propagation timing test case. This simple case uses a simple homogeneous medium, allowing a straight line analytic solution for travel time.

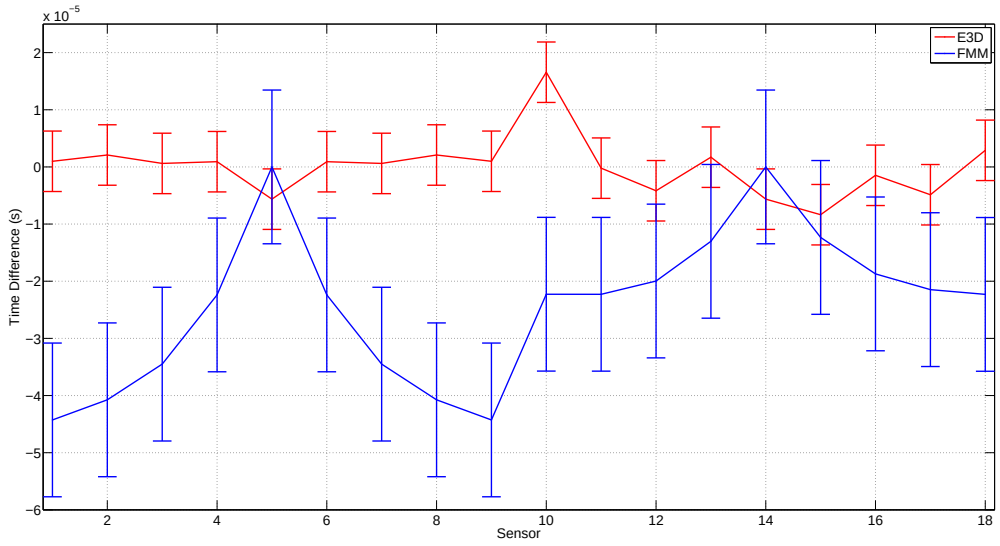

Figure F.1: Relative error plot of the two numerical methods for test case 1. The systematic offset in measured E3D times is subtracted and error bars were attained by calculating the standard deviation for each numerical method against the analytic solution.

F.3 Test Case 2 Results

Sensor	Analytic	E3D	E3D Error		FMM	FMM Error	
No.	(ms)	(ms)	(ms)	(%)	(ms)	(ms)	(%)
1	14.97	15.64	0.67	4.4	15.01	0.05	0.3
2	13.86	14.60	0.73	5.2	13.95	0.09	0.6
3	13.36	14.18	0.82	6.1	13.47	0.10	0.8
4	13.71	14.62	0.90	6.5	13.89	0.17	1.3
5	14.86	15.82	0.95	6.4	15.08	0.21	1.4
6	13.71	14.66	0.94	6.8	13.89	0.17	1.3
7	13.36	14.24	0.88	6.5	13.47	0.10	0.8
8	13.86	14.66	0.79	5.7	13.95	0.09	0.6
9	14.97	15.66	0.69	4.6	15.01	0.05	0.3
10	14.42	15.10	0.68	4.7	14.45	0.03	0.2
11	14.01	14.76	0.75	5.3	14.08	0.07	0.5
12	14.21	15.02	0.81	5.6	14.30	0.09	0.6
13	15.06	15.96	0.90	5.9	15.21	0.15	1.0
14	16.42	17.36	0.94	5.7	16.61	0.18	1.1
15	16.01	16.94	0.93	5.7	16.15	0.14	0.9
16	16.21	17.08	0.87	5.3	16.30	0.09	0.6
17	16.91	17.74	0.82	4.8	17.00	0.08	0.5
18	17.98	18.76	0.78	4.3	18.04	0.06	0.3

Table F.3: Comparison of the results for the second signal propagation timing test case. This simple case uses a homogeneous medium, allowing a straight line analytic solution for travel time.

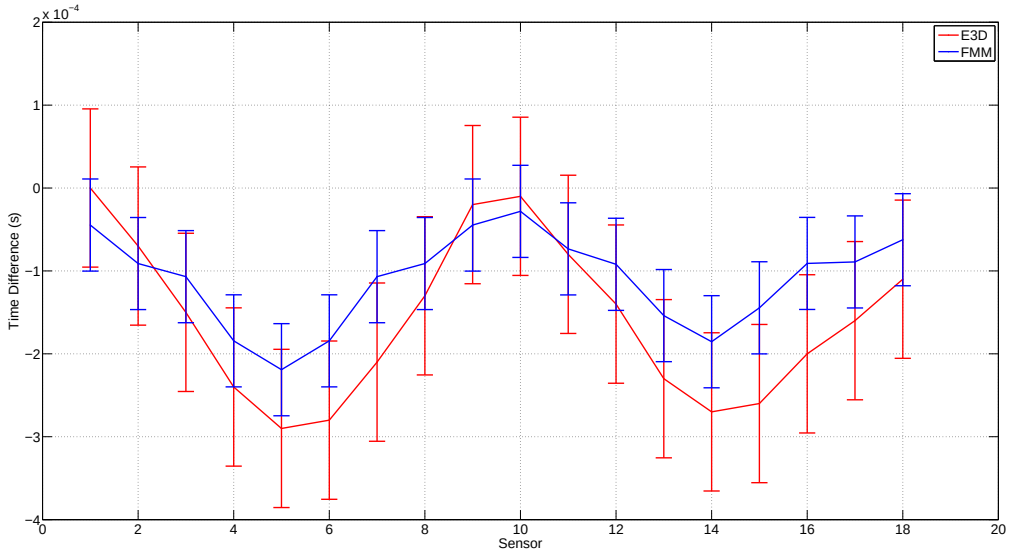

Figure F.2: Relative error plot of the numerical methods for Test case 2. The systematic offset in measured E3D times is subtracted and error bars were attained by calculating the standard deviation for each numerical method against the analytic solution.

F.4 Test Case 3

Sensor No.	E3D (ms)	FMM (ms)	Error (ms)	Error (%)
1	16.22	15.51	0.71	4.4
2	15.72	14.95	0.77	4.9
3	16.08	15.25	0.83	5.2
4	17.32	16.44	0.88	5.1
5	18.98	18.11	0.87	4.6
6	17.28	16.44	0.84	4.9
7	16.08	15.25	0.83	5.2
8	15.70	14.95	0.75	4.8
9	16.20	15.51	0.69	4.2
10	15.70	14.97	0.73	4.7
11	15.90	15.12	0.78	4.9
12	16.84	16.01	0.83	4.9
13	18.34	17.47	0.87	4.8
14	19.96	19.22	0.74	3.7
15	19.12	18.28	0.84	4.4
16	18.72	17.90	0.82	4.4
17	18.90	18.12	0.78	4.1
18	19.56	18.84	0.72	3.7

Table F.4: Comparison of the results for the third signal propagation timing test case. A more complicated test case that uses a velocity void, as well a fracture zone represented by a varying velocity zone that surrounds the void.

Appendix G

ERM Source Data

This appendix details the results attained from the field tests of the pneumatic and eccentric rotating mass seismic sources.

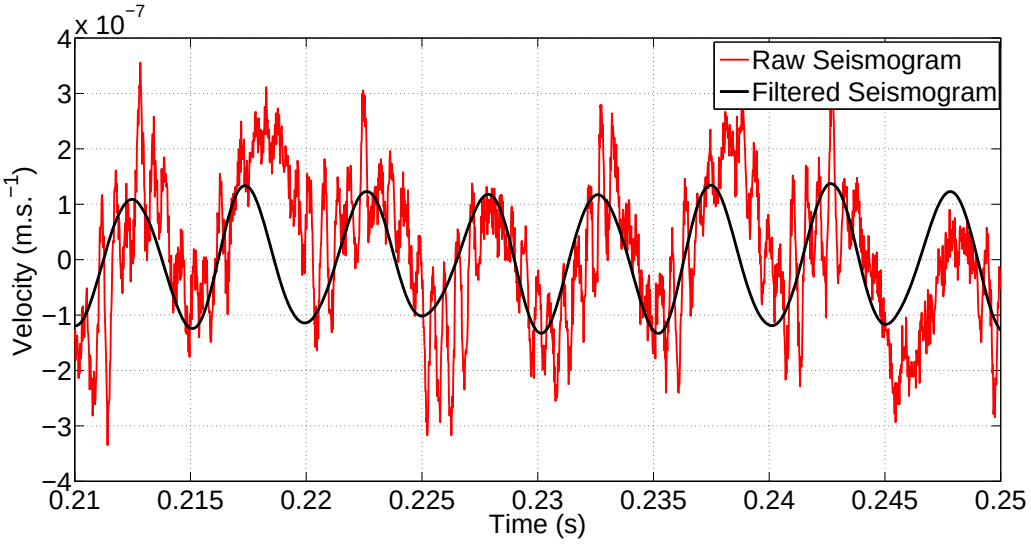

Figure G.1: A example of the sinusoidal signal recorded by sensor D3, positioned 79.8 m away from the eccentric rotating mass source. The red curve denotes the raw unprocessed signal while the black curve denotes the same signal, bandpass filtered between 150 and 300 Hz. The seismic source had an operating frequency of 200 Hz which was evident as a monotonic sine wave in the filtered seismogram.

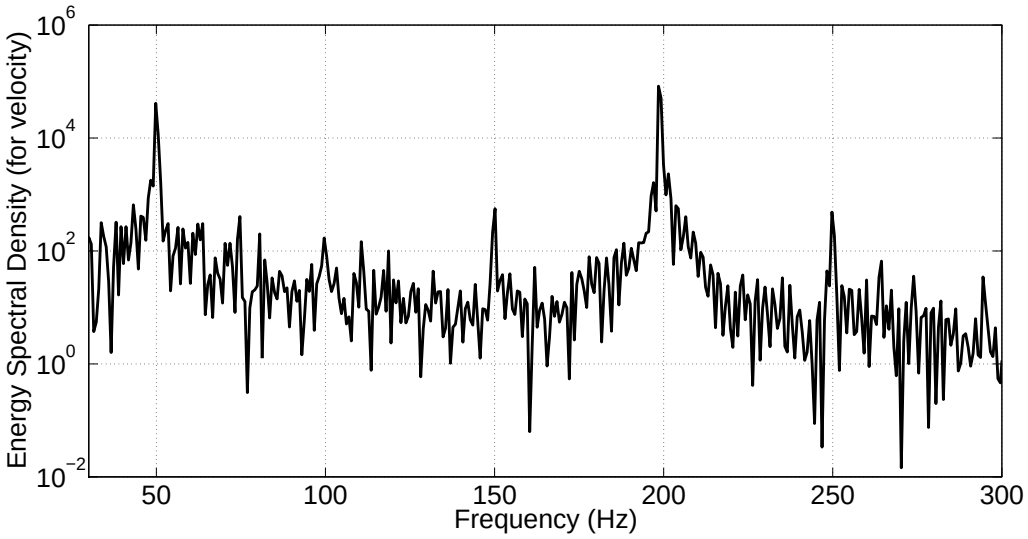

Figure G.2: A spectral energy density plot of unfiltered seismic signal generated by the eccentric rotating mass source. A dominant frequency of 200 Hz is evident which is the operating frequency of the ERM source. Typical mains power interference at 50 Hz is also present on the raw signal.

Appendix H

Physical Experiment Data

H.1 Data Set 1 Travel Time Variation Results

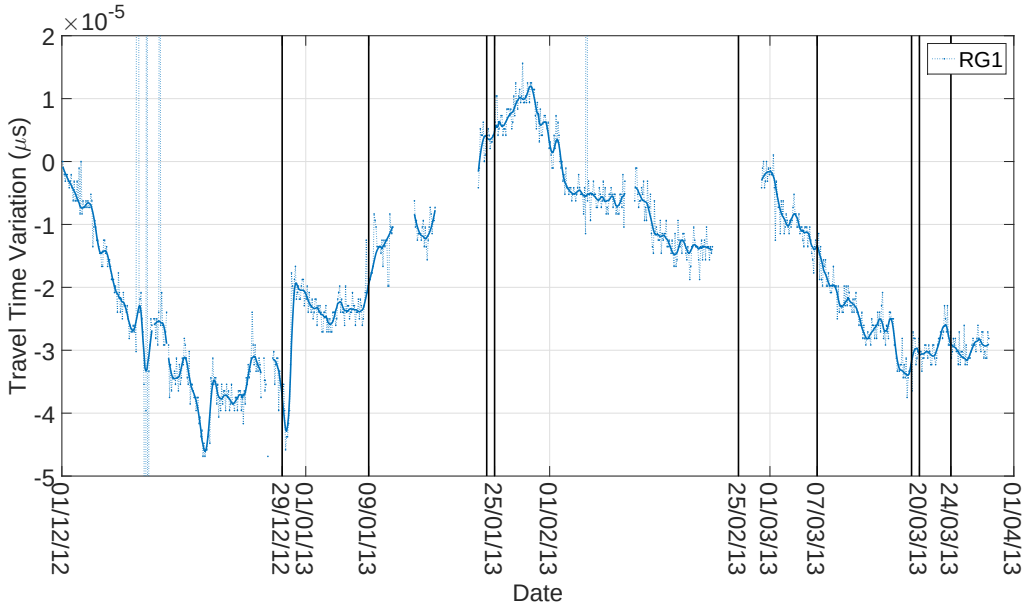

Figure H.1: The travel time variation history calculated for the reference sensors RG1. The unusually large variations suggested that the reference signal may be unsuitable as a zero-time reference.

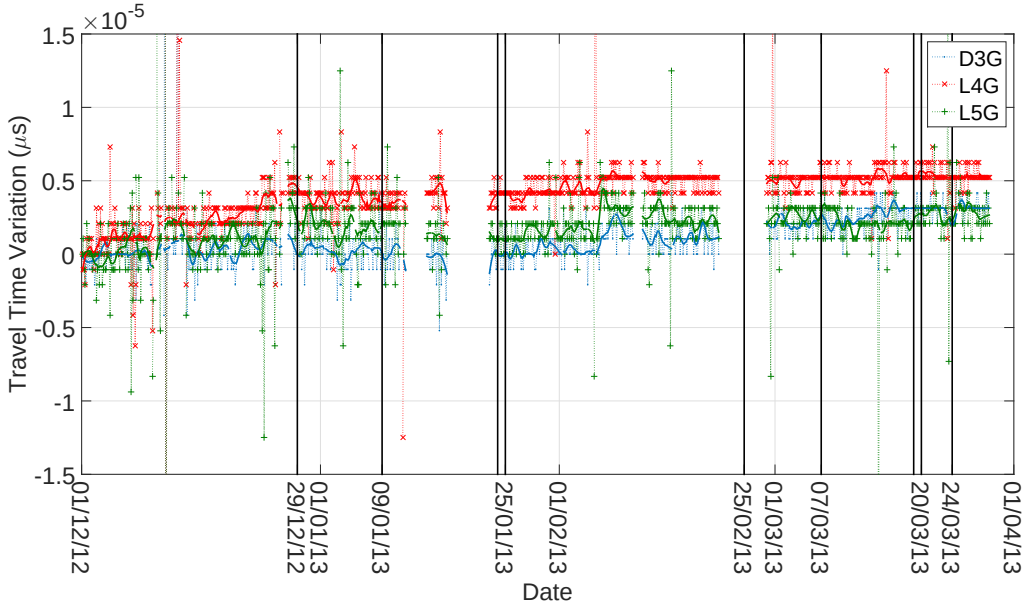

Figure H.2: Travel time variations calculated for the sensors closest to the mining front. Only a small overall increase was observed over the four month recorded period for all three sensors.

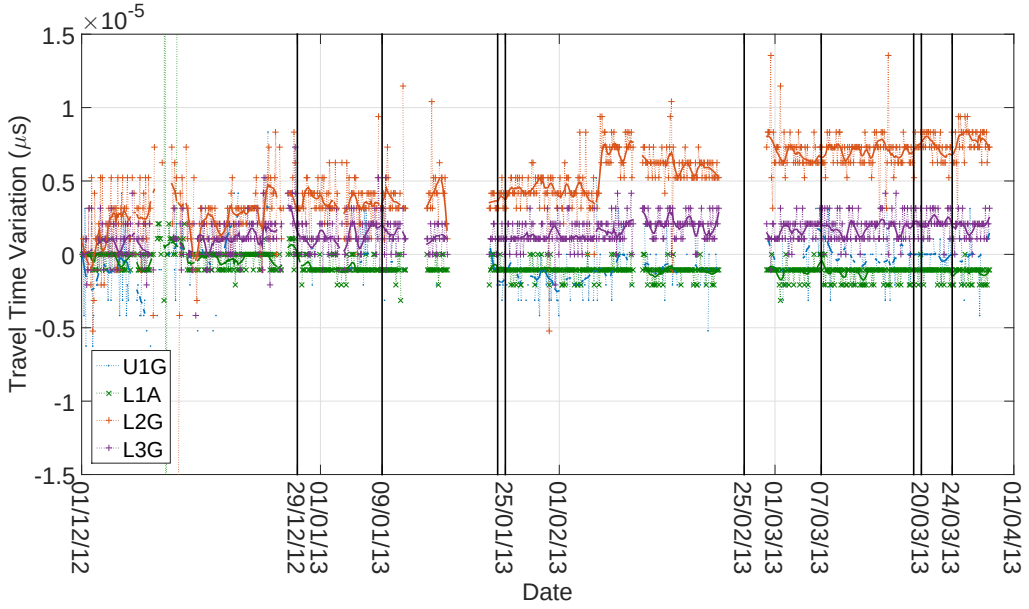

Figure H.3: Travel time variations calculated for the sensors further from the mining front. Little to no change was observed for Sensors L1A and U1G.